CHANDRA STUDIES OF THE X-RAY GAS PROPERTIES OF GALAXY GROUPS

M. SUN[1], G. M. VOIT[1], M. DONAHUE[1], C. JONES[2], W. FORMAN[2], AND A. VIKHLININ[2]

[1] Department of Physics and Astronomy, MSU, East Lansing, MI 48824, USA; msun@virginia.edu

[2] Harvard-Smithsonian Center for Astrophysics, 60 Garden St., Cambridge, MA 02138, USA

ABSTRACT

We present a systematic analysis of 43 nearby galaxy groups ($kT_{500} = 0.7$–2.7 keV or $M_{500} = 10^{13}$–10^{14} h^{-1} $M_\odot$, $0.012 < z < 0.12$), based on *Chandra* archival data. With robust background subtraction and modeling, we trace gas properties to at least r_{2500} for all 43 groups. For 11 groups, gas properties can be robustly derived to r_{500}. For an additional 12 groups, we derive gas properties to at least r_{1000} and estimate properties at r_{500} from extrapolation. We show that in spite of the large variation in temperature profiles inside $0.15\, r_{500}$, the temperature profiles of these groups are similar at $> 0.15\, r_{500}$ and are consistent with a "universal temperature profile." We present the K–T relations at six characteristic radii (30 kpc, $0.15\, r_{500}$, r_{2500}, r_{1500}, r_{1000}, and r_{500}), for 43 groups from this work and 14 clusters from the Vikhlinin et al. (2008) sample. Despite large scatter in the entropy values at 30 kpc and $0.15\, r_{500}$, the intrinsic scatter at r_{2500} is much smaller and remains the same ($\sim 10\%$) to r_{500}. The entropy excess at r_{500} is confirmed, in both groups and clusters, but the magnitude is smaller than previous *ROSAT* and *ASCA* results. We also present scaling relations for the gas fraction. It appears that the average gas fraction between r_{2500} and r_{500} has no temperature dependence, ~ 0.12 for 1–10 keV systems. The group gas fractions within r_{2500} are generally low and have large scatter. This work shows that the difference of groups from hotter clusters stems from the difficulty of compressing group gas inside of r_{2500}. The large scatter of the group gas fraction within r_{2500} causes large scatter in the group entropy around the center and may be responsible for the large scatter of the group luminosities. Nevertheless, the groups appear more regular and more like clusters beyond r_{2500} from the results on gas fraction and entropy. Therefore, mass proxies can be extended into low-mass systems. The M_{500}–T_{500} and M_{500}–$Y_{X,500}$ relations derived in this work are indeed well behaved down to at least 2×10^{13} h^{-1} $M_\odot$.

Key words: cosmology: observations – dark matter – galaxies: clusters: general – X-rays: galaxies: clusters

Online-only material: color figures

1. INTRODUCTION

Most baryons in clusters reside in the hot intracluster medium (ICM), and most clusters are low-mass groups and poor clusters, because the mass function of virialized systems is steep. Studies of galaxy groups are thus especially important for understanding the gravitational and thermal evolution of the bulk of matter in the Universe. In contrast to hot clusters, galaxy groups are systems where baryon physics (e.g., cooling, galactic winds, and AGN feedback) begins to dominate over gravity. Groups are not just a scaled-down version of massive clusters. Cluster scaling relations (e.g., *L–T* and entropy-*T*) show deviations from the self-similar relations at the low-mass end (reviewed in Voit 2005), reflecting the importance of baryon physics, which is essential to shape the properties of the cluster galaxies and ICM. Cooling sets a characteristic entropy threshold in the ICM (Voit & Ponman 2003) and is required to understand the cluster scaling relations (Voit 2005). On the other hand, cooling has to be balanced by feedback to preserve the observed cluster stellar fraction and the galaxy luminosity function. The most important feedback may be the AGN outflows driven by the central supermassive black hole (SMBH). AGN outflows can simultaneously explain the antihierarchical quenching of star formation in massive galaxies, the exponential cutoff at the bright end of the galaxy luminosity function, and the quenching of cooling flows in cluster cores (e.g., Scannapieco et al. 2005; Croton et al. 2006). Along with SN winds, they act to suppress cooling and structure formation. They pump thermal energy into the surrounding ICM as the host galaxy and the central SMBH formed and evolve. These imprints are recorded in the ICM and are reflected in the cluster scaling relations.

There are two important ICM properties that directly reflect the role of baryon physics. The first is ICM entropy. With *ROSAT* and *ASCA* data, Ponman et al. (2003) showed that at $0.1\, r_{200}$, the ICM entropy (K) obeys a simple relation with the cluster temperature (T), $K \propto T^{\sim 0.65}$, which is different from the self-similar relation ($K \propto T$). Ponman et al. (2003) and Voit & Ponman (2003) demonstrated that this K–T relation at $0.1\, r_{200}$ can be understood with a simple model, involving a fixed cooling threshold, which may be related to galaxy formation. However, the details of cooling and feedback that determine this threshold and its scatter are still unclear. Finoguenov et al. (2002) and Ponman et al. (2003) showed that groups and clusters have significant excess entropy at r_{500}. Voit & Ponman (2003) suggested that smooth accretion (via e.g., galactic winds in subhalos) can boost entropy higher than lumpy hierarchical accretion to produce the observed excess. However, Borgani et al. (2005) showed that galactic winds alone are not able to boost entropy very much at radii beyond r_{500}. The AGN-like feedback algorithm in Kay (2004) has a more substantial effect on entropy at large radii, which may imply that radio outflows have an important impact on group properties. Thus, it is important to robustly constrain the entropy around r_{500} with observations and to connect the dispersion with other group properties. The Ponman et al. (2003) results rely on extrapolations based on assumed density (β-model) and temperature (polytropic-model) profiles, which may not be adequate and may bias the derived ICM properties (e.g., Borgani et al. 2004; Vikhlinin et al. 2006, V06 hereafter). These early results can be examined with

Chandra and XMM-*Newton*. There has been some work on the ICM entropy of groups with the *Chandra* or XMM-*Newton* data (e.g., Mushotzky et al. 2003; Sun et al. 2003; Pratt & Arnaud 2005; Pratt et al. 2006; Mahdavi et al. 2005; Finoguenov et al. 2007). Our much larger sample allows us to study the scatter in group properties. As the ICM properties are traced to at least r_{2500} for each group, the K–T relation at $\gtrsim r_{2500}$ can be better constrained from our studies.

Another important ICM property is the gas fraction. Groups have low gas fractions within r_{2500} (0.03–0.07, V06; Gastaldello et al. 2007, G07 hereafter). However, few groups have gas fraction measured to r_{500}. V06 and G07 derived gas fraction within r_{500} for four low-temperature systems ($kT < 2.7$ keV). The results, 0.06–0.15, span a large range. Gas fraction in simulated groups and clusters is directly related to the strength of cooling and star formation (e.g., Kravtsov et al. 2005), and a small gas fraction in groups may imply efficient cooling and star formation. The enclosed gas fraction can also be modified by the AGN feedback (e.g., Puchwein et al. 2008), thus bearing the imprint of the feedback history. It is, therefore, of great interest to know how gas fractions and total baryon fractions (gas + stars) of groups at r_{500} compare with those of clusters. The f_{gas}–T relation is also important for cosmology, e.g., determining cosmological parameters, and using the Sunyaev–Zel'dovich flux as a proxy for the cluster mass (e.g., Vikhlinin et al. 2009, V09 hereafter). Besides the science related to entropy and gas fraction, better determination of the group gas properties are also essential to constraining the low-mass ends of other important scaling relations (e.g., M–T, M–Y_X, and c–M). M–T and M–Y_X relations are essential for using clusters to study cosmology (e.g., Kravtsov et al. 2006; V09), while the c–M relation is important for understanding the formation and evolution of the dark matter halos (e.g., Buote et al. 2007).

We started a systematic analysis of galaxy groups in the *Chandra* archive to better constrain the ICM properties in groups and to better understand the difference between groups and clusters. In this paper, we present the results on 43 galaxy groups that appear relaxed beyond the central core. Our sample is larger than in the previous work on 3–16 groups with *Chandra* and XMM-*Newton* data (Mahdavi et al. 2005; Pratt et al. 2005; Finoguenov et al. 2007; G07; Rasmussen & Ponman 2007). The data are homogeneously analyzed with results on temperature, entropy, gas mass and total mass. The sample size also allows us to measure the scatter in various interesting ICM properties. We focus on the data reduction and the derived scaling relations in this paper, while more extensive discussions with modeling and work on an extended sample including irregular groups will be presented in future papers. The group sample is defined in Section 2. The data analysis is presented in Section 3, including spatial and spectral analysis. We especially discuss the *Chandra* background and our method of background subtraction in this section and in the Appendix. In Section 4, we define four tiers of groups with different data coverage. Different characteristic radii ($r_{2500}, r_{1500}, r_{1000}$, and r_{500}) are reached in different tiers. We also define the system temperatures in Section 4 (T_{500} etc.) and derive their empirical relations. The group temperature profiles are discussed in Section 5, while Section 6 is about the ICM entropy. In Section 7, we discuss M–T and M–Y_X relations, gas fraction, concentration parameter, baryon fraction, and fossil groups in this sample. There are groups with signs of AGN heating and groups with strong central radio sources in this sample. We discuss them in Section 8. Systematic errors are discussed in Section 9. Section 10 contains the summary and

conclusions. We assumed $H_0 = 73$ km s^{-1} Mpc^{-1}, $\Omega_M = 0.24$, and $\Omega_\Lambda = 0.76$.

2. THE GROUP SAMPLE

The groups in the sample are mainly selected from the *Chandra* archive as of 2008 September. We also include proprietary data on three groups from the *Chandra* program 09800349 (PI: Vikhlinin). We started to collect groups from several previous group samples constructed from *ROSAT* observations: Mahdavi et al. (2000), Mulchaey et al. (2003) and GEMS (Osmond & Ponman 2004). We have also searched for low-temperature systems ($T < 3$ keV) in the online database BAX.[3] However, most *ROSAT* groups with well-determined temperatures are quite nearby. The most distant group in GEMS is at $z = 0.0282$ (NGC 6338). As we want to constrain gas properties out to at least r_{2500} (ideally r_{500}) for each system, many nearby systems in these *ROSAT* catalogs are excluded. Thus, we have had to extensively examine the data in the *Chandra* archive seeking groups with good observations out to these large radii. Our selection criteria are: (1) full-frame Advanced CCD Imaging Spectrometer (ACIS) data at the focal plane temperature of -120C (after 2000 January 29); (2) $T_{500} \lesssim 2.7$ keV and a global temperature constrained to better than 15%; (3) $0.015 < z < 0.13$ and group emission traced to at least r_{2500} with the *Chandra* data; (4) group emission well centered around the cD and not significantly elongated or disturbed beyond the group core. T_{500} is the temperature measured between 0.15 r_{500} and r_{500} (defined and discussed in Section 4). The upper limit on T_{500} is determined from the M_{500}–T_{500} relation in V06 to make sure that we are studying low-mass systems with M_{500} of $< 10^{14}\ h^{-1}$ $M_\odot$. We understand that there is not a well-defined temperature boundary separating galaxy groups and clusters. Many people may consider groups to be systems with temperatures of < 2 keV. Nevertheless, we refer to all the systems in our sample as groups for convenient comparison with the clusters in V09. The requirement to well constrain T_{500} allows us to derive a temperature profile for each group. The constraint on redshift enables a first cut to make sure r_{2500} can be reached. We used the r–T relation in V06 as the first guess. It turns out that the derived r–T relations from our work are close to V06's. With the r_{2500}–T relation in V06, $r_{2500} = 11.6'$ for a 1 keV group at $z = 0.015$. An ACIS pointing can reach this radius, although the coverage is partial. The only exception to the redshift requirement is NGC 1550 at $z = 0.0124$. There are two offset observations for this luminous group that allow us to reach r_{1000}. Clearly some hotter systems at $z \gtrsim 0.015$ may not meet our criterion to reach r_{2500} and are excluded after their temperatures are constrained. We indeed have examined many more systems than the ones in our final sample. With *Chandra*'s superior angular resolution, almost all groups have substructures around the center, and in some cases these features can be very significant and striking, like the central 60 kpc of IC 1262 ($\sim 0.1 r_{500}$). Nevertheless, they are included as long as the group emission is well centered and regular at $\gtrsim 0.15 r_{500}$, where our main interests are. Our science goals concerning gas entropy are also not affected by the dynamic state of the group. Moreover, at least the Y_X mass proxy is still robust in unrelaxed systems (Kravtsov et al. 2006).

The *Chandra* archival search not only includes targets in the cluster and galaxy categories, but also targets in the AGN category, as many radio galaxies are in group environments. There are also targets selected optically. Many faint systems

---

[3] http://bax.ast.obs-mip.fr/

are included, as shown by the wide range of gas entropy at 30 kpc and 0.15 r_{500} (Section 6). Thus, our final sample is not much biased to the X-ray luminous systems. The final sample includes 43 groups, listed in Table 1. It is hardly a homogeneous or a complete sample. But the wide spread of the gas densities and entropy values at $r < 0.15r_{500}$ indicates a wide luminosity range as cool cores in groups contribute a large portion of their luminosities (See Section 7.2). If there were groups that are much fainter or poorer in gas than the faint systems in this sample, it is difficult to constrain their gas properties with the current X-ray instruments anyway. Because of the layout of ACIS, full coverage at large radii (defined as > 80% coverage for the outermost spectral extraction bin, as there is always area missing from extended and point sources and chip gaps) is only achieved in seven groups (Table 2). However, the coverage at $r \lesssim r_{2500}$ is much better. Previous analysis for nearby clusters or groups with the *Chandra* data all had partial coverage at large radii (e.g., V06; Rasmussen & Ponman 2007; V09), while our sample is about three times bigger than these previous ones.

3. THE DATA ANALYSIS

3.1. Chandra Observations & Calibration Steps

All observations were performed with ACIS. Standard data analysis was performed which includes the corrections for the slow gain change[4] and charge transfer inefficiency (for both the FI and BI chips). We investigated the light curve of source-free regions (or regions with a small fraction of the source emission) to identify and exclude time intervals with particle background flares, including weak flares. The relevant information on the *Chandra* pointings is listed in Table 1. We corrected for the ACIS low-energy quantum efficiency (QE) degradation due to the contamination on ACIS's optical blocking filter,[5] which increases with time and is positionally dependent. The dead area effect on the FI chips, caused by cosmic rays, has also been corrected. As the background subtraction is important for this project, we present it in detail in the following section and in the Appendix. We do not use any data on the S4 chip, because of the residual streaks often seen at low levels (after running the CIAO tool "DESTREAK") and the lack of the stowed background data. The "readout artifact," seen in groups with very bright cores, is also corrected (see e.g., V06). We used CIAO3.4 for the data analysis. The calibration files used correspond to *Chandra* calibration database (CALDB) 3.4.3 from the *Chandra* X-ray Center, released in 2008 March. We are aware of a possible overcorrection of the *Chandra* effective area beyond the Iridium M-edge (∼ 2 keV) in CALDB 3.4.3 and before (see David's presentation in the 2007 *Chandra* Calibration Workshop),[6] which can bias *Chandra* temperatures to higher values, especially for hot clusters ($T > 4$ keV). The difference between *Chandra* and XMM-*Newton* temperatures is also shown in Snowden et al. (2008). The calibration work to incorporate this into the *Chandra* CALDB is ongoing. However, as shown in both David's presentation and Snowden et al. (2008), the agreement between *Chandra* and XMM-*Newton* temperatures for $\lesssim$ 4–5 keV systems is very good. The highest gas temperature at any radii in our sample is ∼ 3.3 keV for several groups at the center, while temperatures at large radii are much lower and mainly determined by the iron L hump

(instead of the continuum slope as for hot clusters). Thus, any changes in our results from this correction should be smaller than the current measurement errors and scatter. In the spectral analysis, a lower energy cut of 0.4 keV (for the BI data) and 0.5 keV (for the FI data) is used to minimize the effects of calibration uncertainties at low energy. The solar photospheric abundance table by Anders & Grevesse (1989) is used in the spectral fits. Uncertainties quoted in this paper are 1σ.

3.2. Determining the Local Background

Proper background subtraction is important for the analysis in the low-surface brightness regions of the groups. A detailed discussion of the *Chandra* background and the relevant data set is presented in the Appendix. We determine the local background based on the stowed background data and modeling. The corresponding stowed background of each observation is scaled according to the flux ratio in the 9.5–12 keV band (e.g., V05). We adopt a 3% uncertainty on the particle background (PB) normalization (5% for BI data in period E, see the Appendix) in the error budgets.

The local cosmic X-ray background (CXB) can be modeled. The best fit of the hard CXB component is determined with an absorbed power law with a photon index of 1.5. The absorption is determined from spectral fits to the group spectra, which involves iterations and is present in Section 3.3. The soft CXB component is adequately described by two thermal components at zero redshift, one unabsorbed component with a fixed temperature of 0.1 keV and another absorbed component with a temperature either derived from spectral fits or fixed at 0.25 keV (see the Appendix). Abundances of both components are fixed at Solar. We can compare our CXB model with other work. V05 used the blank sky background and corrected for differences between a local control field and the blank sky background. As the scaling factors of the PB are close to unity in their sample, V05 ignored the correction for the unresolved hard CXB. However, the correction for hard CXB becomes more important after the middle of 2004 when the PB flux is 30%–50% higher than that in the blank sky background (the Appendix). V05 found that generally a single thermal component with a temperature of ∼ 0.2 keV and solar abundance can fit the soft CXB excess or decrement well. In regions with high RASS R45 values, a second thermal component with a temperature of ∼ 0.4 keV and solar abundance is required. Humphrey et al. (2006) and G07 also used two thermal components with solar abundances to describe the soft CXB. The CXB temperatures are fixed at 0.07 keV and 0.2 keV. As discussed in the Appendix, Snowden et al. (2008) used three thermal components to describe the soft CXB. Thus, our model of the soft CXB only has less freedom than the model by Snowden et al. (2008). However, our model balances the requirement of having enough components to fit the local CXB and avoiding parameter degeneracy in generally low-statistics data. First, the two ∼ 0.1 keV components will naturally be mixed in our energy band when the absorption is low. Second, statistics for most of our groups at large radii are not very good, so uncertainties are mainly statistical errors. As long as the background uncertainties are folded into the final error budgets, very detailed modeling of the soft CXB component is not crucial. Third, we test different models of the soft CXB for groups in our sample for which a large group-emission-free region is available. All spectra can be well fit by our two-component model, while the three-component model by Snowden et al. (2008) makes little or no improvement. In fact, the soft CXB can be well

---

Table 1
The Group Sample and the *Chandra* Observations

Group	z[a]	D[b]	ObsID[c]	Date	Exposure[d]	PSPC[e]	L_{K_s}[f]	$L_{1.4GHz}$[g]
NGC 1550	0.0124	51.4	3186	2002 Jan 8	9.7		11.29	21.72
			3187	2002 Jan 8	9.5			
			5800	2005 Oct 22	43.0 (44.0)			
			5801	2005 Oct 24	44.0 (44.3)			
NGC 3402	0.0153	63.5	3243	2002 Nov 05	22.9 (29.5)		11.40	22.18
A262	0.0163	67.8	2215	2001 Aug 3	28.7 (28.7)	7.6	11.60	22.56
			7921	2006 Nov 20	110.5 (110.5)			
NGC 383 (3C 31)	0.0170	70.8	2147	2000 Nov 6	41.0 (44.3)	24.0	11.67	24.46
3C 449	0.0171	71.2	4057	2003 Sep 18	14.3 (26.4)	8.9	11.13	24.36
NGC 533	0.0185	77.1	2880	2002 July 28	29.7 (37.1)	11.5	11.76	22.31
NGC 741	0.0185	77.3	2223	2001 Jan 28	28.7 (30.2)	12.4	11.82	23.85
MKW4	0.0200	83.4	3234	2002 Nov 24	27.6 (29.7)	9.4	11.81	22.15
A3581	0.0230	96.2	1650	2001 June 07	7.2 (7.2)		11.51	23.85
NGC 5129	0.0230	96.2	6944	2006 April 13	20.5 (20.5)	5.5	11.63	21.90
			7325	2006 May 14	25.6 (25.6)			
NGC 1132	0.0233	97.5	3576	2003 Nov 16	20.5 (37.1)		11.64	21.79
UGC 2755	0.0245	102	2189	2001 Feb 7	7.2 (15.6)	16.4	11.49	24.26
NGC 4325	0.0257	108	3232	2003 Feb 4	25.6 (29.9)	4.8	11.31	< 21.32
HCG 51	0.0258	108	4989	2004 Feb 15	18.4 (18.9)		11.47	< 21.32
			5304	2004 Feb 16	12.2 (12.7)			
3C 442A	0.0263	110	5635	2005 July 27	26.6		11.51, 11.40	24.70
			6353	2005 July 28	13.6			
			6359	2005 Oct 7	19.4			
			6392	2006 Jan 12	31.7			
UGC 5088	0.0274	115	3227	2002 March 10	33.8		11.26	21.04
NGC 6338	0.0274	115	4194	2003 Sep 17	39.9	3.5	11.73	22.95
NGC 4104	0.0282	118	6939	2006 Feb 16	35.8 (35.8)	13.6	11.85	21.60
RBS 461	0.0296	124	4182	2003 March 11	22.0		11.41	22.57
ESO 552-020	0.0314	132	3206	2002 Oct 14	18.7		11.92	< 21.72
A1177	0.0316	133	6940	2006 Dec 27	32.8 (33.5)		11.73	< 21.50
IC 1262	0.0326	138	2018	2001 Aug 23	25.6 (30.5)		11.49	23.22
			6949	2006 April 17	38.1			
			7321	2006 April 19	36.8			
			7322	2006 April 22	37.4			
NGC 6269	0.0348	147	4972	2003 Dec 29	38.6	10.1	11.94	23.11
ESO 306-017	0.0358	151	3188	2002 March 8	13.6		11.91	22.58
			3189	2002 March 9	13.8			
			914*	2000 July 26	50.4			
NGC 5098	0.0368	156	2231	2001 Aug 4	10.0		11.44, 11.36	23.38
			6941	2005 Nov 1	37.9 (38.6)			
A1139	0.0398	169	9387	2008 March 28	10.0		11.50	23.16
A160	0.0447	190	3219	2002 Oct 18	54.5		11.69	24.65
UGC 842	0.0452	192	4963	2005 Feb 13	38.9 (39.2)		11.77	22.24
A2717	0.0498	213	6973	2006 Aug 17	46.1	8.5	11.82	24.52
			6974	2006 April 10	18.9			
RXJ 1022+3830	0.0543	233	6942	2006 Oct 14	40.9 (41.4)	10.3	11.69, -	< 21.98
AS1101	0.0564	242	1668	2001 Aug 13	9.2 (9.4)	11.9	11.89	24.27
ESO 351-021	0.0571	245	5784	2005 April 24	34.8 (35.1)		11.95	22.71
A3880	0.0581	250	5798	2004 Dec 23	19.7		11.93	24.22
A1991	0.0587	253	3193	2002 Dec 16	36.8 (36.3)	20.0	11.86	23.47
A1275	0.0637	275	6945	2006 Feb 5	49.1 (48.4)		11.31	< 22.13
A2092	0.0669	290	9384	2007 Nov 13	9.7		11.44	< 22.17
RXJ 1206-0744	0.0680	295	9388	2007 Nov 15	10.0		11.75	< 22.19
A1238	0.0720	313	4991	2004 March 28	18.2		11.70	24.44
A744	0.0729	317	6947	2006 Oct 22	36.3		11.80	22.24
A2462	0.0733	319	4159	2002 Nov 19	37.9 (38.6)	3.4	11.82	25.36
RXJ 1159+5531	0.0808	354	4964	2004 Feb 11	69.6 (74.2)		11.97	< 22.34
A1692	0.0848	372	4990	2004 Aug 12	21.5		11.88	22.33
			6930*	2006 March 6	76.0			
			7289*	2006 March 9	75.0			
A2550	0.122	550	2225	2001 Sep 3	57.3 (58.8)		11.62	23.18

Notes.
[a] The group redshift is extracted from NASA/IPAC Extragalactic Database (NED)
[b] The luminosity distance of the group derived from its redshift
[c] The ObsIDs with * are observations that happened to be close to the interested groups. We used these observations to constrain the local soft CXB.
[d] Effective exposure after excluding time intervals of background flares. For observations with ACIS-S3 at the optical axis, two exposure values are listed, with the one in the brackets as the exposure for the FI chips.
[e] *ROSAT* PSPC clean exposure time (in ksec) if the pointed PSPC observations exist.
[f] 2MASS K_s band luminosity of the cD galaxy as shown as $\log(L_{K_s}/L_\odot)$, $M_{K\odot} = 3.39$ mag. There are three groups (3C 442A, NGC 5098 and RXJ 1022+3830) with two BCGs at the center. The K_s band magnitude of one central galaxy in RXJ 1022+3830 is unknown.
[g] 1.4 GHz luminosity of the cD galaxy as shown as $\log(L_{1.4GHz}/\text{W Hz}^{-1})$ from the NRAO VLA Sky Survey (NVSS) or the Sydney University Molonglo Sky Survey (SUMSS), assuming a spectral index of -0.8, unless it can be derived from NED.

Table 2
Absorption, Radial Range of the Analysis and the Local CXB

Group	N_H[a] (10^{20} cm^{-2})	R45[b]	Outermost bin[c] (%)	$r_{det,spe}$[d] (kpc)	$r_{det,sur}$[e] (kpc)	kT_{hot}[f] (keV)	$f_{0.47--1.21keV}$[g]	$f_{2--8keV}$[h]	$f_{2--8keV,expected}$ (f_{limit})[i]
NGC 1550	12.5 (10.0)	125	11	355	364	$0.20^{+0.04}_{-0.07}$	$4.5^{+0.2}_{-0.4}$	$13.5^{+4.2}_{-4.5}, 7.4^{+4.5}_{-4.0}$	$\sim$12.6 ($\sim$2.1), $\sim$8.5 ($\sim$0.56)
NGC 3402	11.0 (4.0)	119	31	239	239	(0.25)	$5.0^{+0.2}_{-0.6}$	$6.5^{+2.5}_{-3.5}$	$\sim$6.8 ($\sim$ 0.27)
A262	8.1 (5.8)	152	19	363	387 (800)	0.27 ± 0.03	$2.7^{+0.6}_{-0.5}$	$10^{+4.0}_{-4.5}, 8.4^{+3.4}_{-4.0}$	$\sim$9.4 (0.51-1.1), $\sim$7.7 (0.31-0.65)
NGC 383	5.3	100	21	289	350 (500)	(0.25)	$3.2^{+0.4}_{-0.9}$	$9.3^{+3.2}_{-2.6}$	$\sim$8.4 (0.47--0.61)
3C 449	13.3 (9.0)	161	32	230	230 (380)	(0.25)	$6.7^{+0.8}_{-0.3}$	$10.0^{+5.0}_{-2.6}$	$\sim$8.4 ($\sim$0.47)
NGC 533	5.7 (3.0)	103	26	238	340 (380)	0.31 ± 0.05	$3.9^{+0.9}_{-0.5}$	$7.1^{+2.5}_{-2.2}$	$\sim$ 7.2 ($\sim$ 0.33)
NGC 741	5.9 (4.3)	100	33	271	360 (420)	$0.23^{+0.05}_{-0.03}$	$3.7^{+0.5}_{-0.3}$	$6.7^{+3.0}_{-3.5}$	$\sim$ 7.5 ($\sim$ 0.36)
MKW4	3.1 (1.8)	117	10	490	490 (720)	(0.25)	$4.7^{+0.6}_{-0.3}$	$7.5^{+3.7}_{-3.9}$	$\sim$8.4 (0.34--0.78)
A3581	5.8 (4.5)	296	25	322	450	$0.27^{+0.03}_{-0.02}$	$12.5^{+0.4}_{-0.2}$	$10.6^{+2.3}_{-5.5}$	$\sim$10.1 ($\sim$0.98)
NGC 5129	5.5 (1.7)	298	45	214	222 (270)	$0.29^{+0.02}_{-0.01}$	$12.3^{+0.7}_{-0.3}$	$7.0^{+3.9}_{-4.8}$	$\sim$7.0 (0.17--0.41)
NGC 1132	7.8 (5.5)	92	33	284	310	0.28 ± 0.04	$2.5^{+0.7}_{-0.3}$	$7.3^{+2.9}_{-2.5}$	$\sim$6.5 ($\sim$0.22)
UGC 2755	13.6	93	52	193	193 (205)	$0.26^{+0.06}_{-0.04}$	$3.3^{+0.6}_{-0.5}$	$10.4^{+3.0}_{-3.7}$	$\sim$ 8.7 (0.55--0.73)
NGC 4325	2.4	143	23	232	232 (250)	(0.25)	$4.5^{+1.2}_{-1.3}$	$8.1^{+5.4}_{-5.0}$	$\sim$ 7.0 ($\sim$ 0.30)
HCG 51	5.3 (1.1)	118	30	329	360	(0.25)	$2.2^{+0.6}_{-0.3}$	$6.8^{+2.5}_{-3.0}$	$\sim$ 7.2 ($\sim$ 0.33)
3C 442A	6.1 (4.8)	85	68	396	530	(0.25)	$2.0^{+0.5}_{-0.6}$	6.6 ± 3.4	$\sim$7.6 (0.25--0.7)
UGC 5088	1.2	90	63	317	320	(0.25)	$2.5^{+0.3}_{-0.4}$	$6.5^{+2.4}_{-2.2}$	$\sim$7.0 ($\sim$0.27)
NGC 6338	2.3	133	43	349	360 (510)	(0.25)	$2.0^{+0.5}_{-0.6}$	$9.2^{+4.6}_{-2.8}$	$\sim$7.0 ($\sim$0.31)
NGC 4104	4.4 (1.8)	113	33	407	420 (550)	$0.23^{+0.07}_{-0.05}$	$2.7^{+0.4}_{-0.2}$	$8.1^{+5.0}_{-5.8}$	$\sim$7.0 ($\sim$0.30)
RBS 461	17.7 (15.0)	65	54	359	515	(0.25)	$3.6^{+0.3}_{-0.6}$	$10.0^{+6.0}_{-3.7}$	$\sim$8.6 ($\sim$ 0.56)
ESO 552-020	3.9	119	51	380	480	(0.25)	$2.4^{+0.4}_{-0.7}$	$8.8^{+3.4}_{-3.5}$	$\sim$7.8 ($\sim$ 0.46)
A1177	4.6 (1.1)	103	35	418	420	0.15 ± 0.02[j]	$2.0^{+0.4}_{-0.2}$	$6.5^{+2.8}_{-3.4}$	$\sim$ 7.3 ($\sim$ 0.34)
IC 1262	3.4 (1.8)	162	74	375	390	0.32 ± 0.04	$5.4^{+0.4}_{-1.0}$	$8.1^{+3.1}_{-2.2}$	6.0--7.3 (0.15--0.31)
NGC 6269	5.2	106	48	439	510 (740)	(0.25)	2.5 ± 0.4	$8.2^{+2.3}_{-3.3}$	$\sim$ 7.0 ($\sim$ 0.30)
ESO 306-017	3.0	105	77	484	490	$0.23^{+0.04}_{-0.03}$	$4.9^{+0.6}_{-0.8}$	$11.0^{+4.9}_{-2.6}$	$\sim$ 9.7 ($\sim$ 0.85)
NGC 5098	6.8 (1.3)	120	81	421	480	$0.25^{+0.05}_{-0.04}$	$2.6^{+0.4}_{-0.5}$	$5.9^{+3.7}_{-3.9}, 9.5^{+4.8}_{-4.2}$	$\sim$ 10.1 ($\sim$ 0.95), $\sim$ 6.9 ($\sim$ 0.26)
A1139	3.2	93	94	318	370	(0.25)	$2.6^{+0.4}_{-0.5}$	$10.8^{+5.8}_{-4.3}$	$\sim$ 9.6 ($\sim$ 0.87)
A160	4.0	100	62	507	640	(0.25)	3.2 ± 0.5	$7.8^{+3.7}_{-2.9}$	$\sim$ 6.7 ($\sim$ 0.22)
UGC 842	4.0	99	25	410	510	0.26 ± 0.03	$4.4^{+0.5}_{-0.6}$	$7.5^{+3.5}_{-2.6}$	$\sim$6.8 ($\sim$ 0.22)
A2717	1.2	122	37	730	800 (760)	$0.31^{+0.07}_{-0.06}$	3.6 ± 0.6	$7.1^{+3.2}_{-2.9}, 9.4^{+4.1}_{-3.2}$	$\sim$ 6.3 ($\sim$ 0.20), $\sim$ 8.6 ($\sim$ 0.58)
RXJ 1022+3830	3.3 (1.5)	116	32	548	610 (670)	0.30 ± 0.06	2.5 ± 0.6	$8.8^{+5.2}_{-3.8}$	$\sim$ 7.0 ($\sim$ 0.27)
AS1101	1.1	130	23	568	650 (850)	0.28 ± 0.07	3.5 ± 0.9	$13.0^{+6.5}_{-5.0}$	$\sim$10.1 ($\sim$ 0.95)
ESO 351-021	2.4	129	34	511	515	$0.28^{+0.07}_{-0.04}$	$2.5^{+0.4}_{-0.6}$	$7.2^{+3.7}_{-2.9}$	$\sim$6.8 ($\sim$ 0.26)
A3880	1.2	149	37	779	810	(0.25)	$3.5^{+1.0}_{-0.6}$	$9.2^{+3.5}_{-3.9}$	$\sim$8.0 ($\sim$ 0.43)
A1991	2.5	280	31	655	820 (750)	0.33 ± 0.02	14.4 ± 0.6	$6.7^{+2.9}_{-2.5}$	$\sim$7.0 ($\sim$ 0.29)
A1275	6.2 (2.0)	91	42	495	530	$0.21^{+0.06}_{-0.09}$	$2.1^{+0.5}_{-0.4}$	$7.7^{+3.8}_{-3.4}$	$\sim$6.3 ($\sim$ 0.16)
A2092	2.2	130	79	555	600	(0.25)	$3.1^{+0.3}_{-0.4}$	$6.3^{+1.9}_{-1.8}$	$\sim$ 9.2 ($\sim$ 0.79)
RXJ 1206-0744	2.3	134	92	451	580	(0.25)	$2.1^{+0.6}_{-1.2}$	$9.2^{+4.3}_{-3.0}$	$\sim$ 9.4 ($\sim$ 0.84)
A1238	3.5	103	81	673	690	$0.22^{+0.09}_{-0.05}$	$2.4^{+0.4}_{-0.7}$	$8.3^{+4.2}_{-3.3}$	$\sim$ 8.2 ($\sim$ 0.49)
A744	3.5	104	92	433	600	$0.20^{+0.30}_{-0.06}$	$2.7^{+0.4}_{-0.5}$	$6.4^{+3.3}_{-2.6}$	$\sim$ 6.8 ($\sim$ 0.24)
A2462	3.1	158	50	564	650 (800)	0.26 ± 0.02	7.8 ± 0.6	$7.6^{+5.0}_{-2.1}$	$\sim$6.4 ($\sim$ 0.19)
RXJ 1159	1.2	134	56	529	560	0.27 ± 0.03	2.7 ± 0.5	$6.0^{+3.1}_{-2.5}$	$\sim$5.5 (0.08--0.14)
A1692	1.8	158	80	766	770	$0.26^{+0.05}_{-0.04}$	4.2 ± 0.5	$7.3^{+3.9}_{-3.0}$	$\sim$8.0 ($\sim$ 0.39)
A2550	1.9	130	75	597	740	0.28 ± 0.03	4.8 ± 0.7	$7.8^{+3.4}_{-3.1}$	$\sim$ 5.9 ($\sim$ 0.13)

Notes.

[a] The absorption column density in our analysis. If the value from our spectral analysis (Section 3.3) is consistent with the Galactic value from the Leiden/Argentine/Bonn (LAB) HI survey (Kalberla et al. 2005), the LAB value is used. Both values are listed if they are significantly different, with the number in brackets is the LAB value.

[b] The *ROSAT* All-Sky Survey R45 flux (Snowden et al. 1997), in a unit of 10^{-6} cts/s/arcmin^2, measured from an annulus centered on the source. The inner radius of the annulus is 0.4--0.8 deg (depending on the source size), while the outer radius is the inner radius + 0.4 deg. In a few cases, we have to use partial apertures to exclude the bright sources near our targets (e.g., A1692 and A2550).

[c] The fraction of the outermost radial bin for the spectral analysis covered by the *Chandra* data, compared with the full annulus. The median is 42%. Note this fraction is always less than one because of point sources and chip gaps.

[d] The outermost radius for the *Chandra* spectral analysis

[e] The radius where X-ray surface brightness is detected at $>2\sigma$. $r_{out}/r_{in} = 1.06$-1.1. Note that our estimate of local background is conservative so our 2σ range is smaller than V06's 3σ range for A1991 and RXJ 1159+5531. The value in brackets is for PSPC if available.

[f] The temperature of the hotter component of the local soft CXB

[g] The 0.47--1.21 keV observed flux of the local soft CXB (in unit of 10^{-12} ergs cm^{-2} s^{-1} deg^{-2}). The energy band is chosen to match that of the RASS R45 band.

[h] The 2--8 keV unabsorbed flux of the unresolved hard CXB (in unit of 10^{-12} ergs cm^{-2} s^{-1} deg^{-2})

[i] The expected 2--8 keV unabsorbed flux of the unresolved hard X-ray CXB (in unit of 10^{-12} ergs cm^{-2} s^{-1} deg^{-2}), estimated based on the limiting flux (shown in brackets, in unit of 10^{-14} ergs cm^{-2} s^{-1}) and from the derived average relation in K07.

[j] The 0.1 keV component has zero normalization in this case.

fitted by a single thermal component in most cases. However, the abundance usually has to be free and the best-fit value is usually very close to zero. Therefore, we conclude that the two-component soft CXB model is adequate and also necessary for our analysis.

The *Chandra* observations in our sample can be classified into two categories, one with regions free of group emission in the field of view (FOV), another with group emission detected to

the edge of the field. Cool systems at higher redshifts (e.g., $z > 0.04$) usually have group-emission-free regions in the off-center chips (e.g., S2 for ACIS-I observations, I2/3 and S1 for ACIS-S observations). There are also two groups with adjacent *Chandra* pointings for unrelated targets in coincidence (ESO 306-017 and A1692). We took the following approach to look for group-emission-free regions. The radial surface brightness profile is derived with the exposure correction and

background subtraction using the scaled stowed background. Different pointings for the same group are combined. The obtained surface brightness profile has group emission plus the CXB. The region where CXB is more dominant than the group emission, if present, can be determined from the flattened portion at the outer region of the surface brightness profile. We used a power law plus a constant at large radii to determine whether a significant group-emission-free region exists and the radial range of that region. If such a region is found, we have a control field with only CXB. In this work, the inner radius of the group-emission-free region is $> 3'$ larger than the outermost radius for the group temperature profile. This control field may be a single region on the S2 chip (for the ACIS-I data) or two separate regions on the S1 and I2/I3 chips respectively (for the ACIS-S data). Although we could simply fit the spectrum (or spectra) of this control field to determine the local CXB, the statistics are generally not sufficient. Moreover, the hard CXB in this control field may be larger than that in the outermost bin for the group temperature profile, as the flux of the hard CXB depends on point source excision. Thus, we fit the spectra of the control field and the outermost bin for the group temperature profile together to better constrain the local CXB. The normalizations of the soft CXB in different regions are linked by the ratios of their covered solid angles of the sky, while the normalizations of the hard CXB are not linked. Therefore, we can determine the local CXB in the outermost bin for the group temperature profile. In this work, we assume that the soft CXB is constant across the examined group area. Accurate determination of the local CXB is only important for large radii. The covered area at large radii tends to be in the same direction from the group center so the assumption should be reasonable. There is a complication that the hard CXB may be smaller in inner radial bins, but it is a small effect and can be corrected (also discussed later in this section).

However, many groups in our sample have group emission detected to the edge of the field, so we have to fit the CXB components with the group emission together. Since these groups are limited by the *Chandra* FOV, the group emission is generally still significant near the edge of the field. We fit the spectra from the two outermost radial bins together, with the normalizations of the soft CXB components linked. Generally in this work, we are conservative and do not include the outermost bin in the temperature profile as the uncertainties are generally large. However, there are a few groups that remain bright to the edge of the field (e.g., NGC 1550, A262, and MKW4). They all have S1 data, so the soft CXB component can be easily separated from the group emission (e.g., Figure 1), owing to the good response of the BI chips at < 1 keV. As the temperatures of the cool gas can be well constrained from the iron hump centroid, group emission can be robustly separated from the soft CXB even to the edge of the field. Thus, we derive temperature profiles to the edge of the field for these groups.

As we separate the PB from the CXB, the absolute CXB flux can be derived in each group field. In Table 2, we list the flux of the local background components, for both the soft CXB and the hard unresolved CXB (in the outermost bin). We expect the derived soft CXB is on average correlated with the RASS R45 flux in the surrounding area (excluding the source region, see Table 2), which is true as shown in Figure 2. One should be aware of the uncertainty in the R45 flux, as the RASS soft X-ray background maps have 0.2 deg pixels and the various uncertainties combined are not small (e.g., variable SWCX emission). There are also uncertainties related to cross-
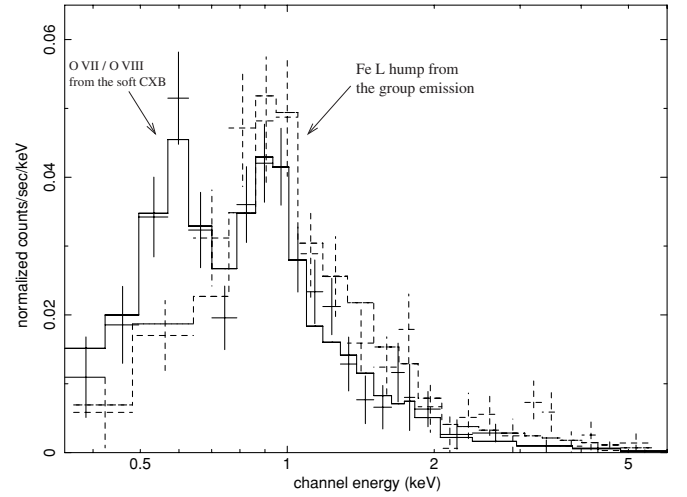

Figure 1. Spectra of the NGC 1550 in the outermost radial bin that is to the edge of the *Chandra* FOV (one from the S1 chip of the ObsID 5800 in the solid line and another from the S2 chip of the ObsID 3187 in the dashed line). Besides the still significant iron L hump from the group emission, the O hump from the soft CXB is also strong in the S1 spectrum, which allows a robust separation of these two components.
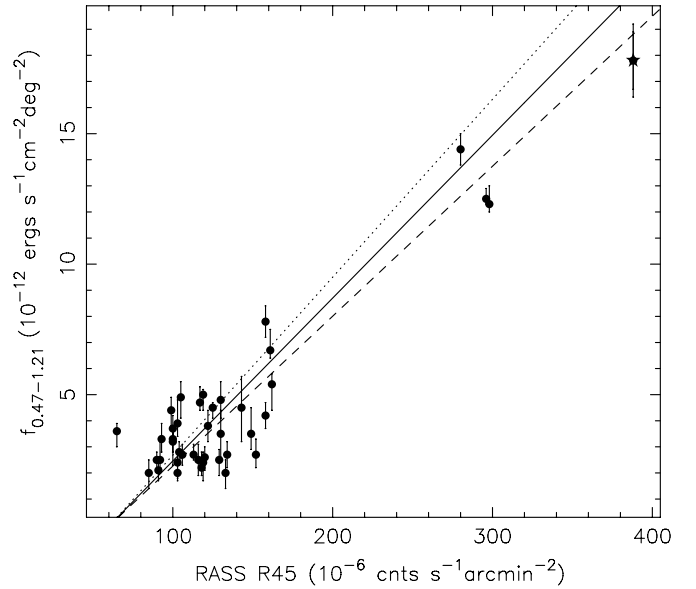

Figure 2. 0.47–1.21 keV observed flux surface density of the soft CXB from the *Chandra* data vs. the RASS R45 flux (in RASS channels of 13–18) measured in an annulus around the target (inner radius of 0.4–0.8 deg and the outer radius is the inner radius + 0.4 deg). The three lines are the expected conversions between two fluxes, with the assumed two thermal components for the soft CXB (all with $T_{cool} = 0.1$ keV). The solid line is for $T_{hot} = 0.25$ keV and $NORM_{hot}$ / $NORM_{cool} = 0.5$. The dotted line is for the $T_{hot} = 0.2$ keV and $NORM_{hot}$ / $NORM_{cool} = 0.5$. The dashed line is for: $T_{hot} = 0.3$ keV and $NORM_{hot}$ / $NORM_{cool} = 1$. The assumed absorption is 4×10^{20} cm^{-2}. The total hard CXB (1.74×10^{-11} ergs s^{-1} cm^{-2} deg^{-2} in the 2–8 keV band from K07) is added in the conversion. The good agreement on average can be seen. One should be aware that the RASS R45 flux is extracted in a much larger area surrounding the interested group range and some of the soft CXB may come from the time-variable SWCX emission. We also include 3C 296 ($T_{hot} = 0.38 \pm 0.03$) in the high CXB flux end (star). It is an 1 keV group but was left out as the high local soft CXB (on NPS) prohibits deriving gas properties to r_{2500}.

calibration and cosmic variance of both the soft and hard CXB, so a detailed one-to-one comparison is hardly meaningful. The derived 2–8 keV flux of the hard CXB component depends on the limiting flux of the observation. As discussed in the Appendix, there is an empirical relation between the limiting

flux for point sources and the average 2–8 keV flux of unresolved hard CXB (K07). We estimated the average limiting flux of the group observations in the outermost spectral bin. The regions we used to control the local background generally have an area of about one ACIS chip. As shown in Hickox & Markevitch (2006, HM06 hereafter) and K07, the cosmic variance in this angular scale (depending on the two-point angular correlation function of point sources) is 20%–30% and the total hard CXB flux has $\sim 10\%$ uncertainty. Thus, the expected hard CXB flux from the empirical relation is only meaningful in an average sense. We use the CIAO tool MKPSF to generate several PSFs (at an energy of 1.4 keV) in the outermost spectral bin. We then derive the 90% enclosed power aperture and measure the 3σ limits at these regions. Their average is taken as the estimate for the limiting flux for point sources. Compared with the average growth curve determined by K07 (their Figure 19), we have an estimate of the unresolved hard CXB, which is also listed in Table 2. We can see from Table 2 that the general agreement is quite good, while the uncertainties for the hard X-ray CXB are much larger than the difference. It is also true that the limiting flux for point sources depends on the off-axis angle. The *Chandra* limiting flux changes little within the central 6–7′ from the aim point, but increases rapidly beyond 10′. This can be corrected from the slope of the limiting flux versus unresolved hard CXB in K07 and the absolute flux in the outermost bin. The correction is small, also because the errors of the hard CXB are not small.

Besides the 3% uncertainty on the PB mentioned above (5% for BI data in period E), we also included the following error budgets and added them (and the PB uncertainty) to the statistical uncertainties of temperatures, abundances, and surface brightness in quadrature. For the hard CXB, we set the photon index at 1.1 and 1.9 (e.g., HM06) and repeat the analysis to estimate the local background in those situations. For the soft CXB component, if the temperature of the hotter component cannot be derived from the data and is fixed at 0.25 keV, we change it to 0.2 keV and 0.3 keV and repeat the analysis to estimate the local background in those situations. Thus, we are conservative in the uncertainties for the local CXB.

3.3. Spectral Analysis and Deprojection

Once the local CXB is determined, we proceed to derive the projected temperature profile. The radial bins for temperature measurement are decided from the outermost bin, by requiring the temperature to be constrained to better than 30% (1σ with all error budgets) and $r_{out}/r_{in} = 1.3$–1.75. After determining the outermost bin, the inner bins are determined progressively with $r_{out}/r_{in} = 1.25$–1.6. Point sources and subclumps are excluded. The absorption column is determined from the MEKAL fit to the integrated spectrum between $0.1r_{500}$ and $0.4r_{500}$. In this process, we also tried the VMEKAL model with extra free parameters of O, Ne, Mg, Si, S, Fe, and Ni abundances, as a lower O/Fe ratio may cause excess absorption (Buote et al. 2003). This process and the determination of the local CXB are done in iterations to obtain the final value of the absorption. If the derived absorption is consistent with the Galactic absorption from the HI survey (Table 2) within 1σ, the Galactic value is used. Only when both MEKAL and VMEKAL fits show excess absorption, the X-ray absorption from the MEKAL fit (always consistent with the VMEKAL fit within 1σ) is adopted (Table 2). About 44% of groups show excess absorption relative to the Galactic value, and indeed we find *IRAS* 100 μm enhancement in many of these groups (see the Appendix for discussions of some groups). We also examined the absorption variation with

radius in each group. Beyond the central 20 kpc, no significant absorption variation is found for any group so we used a fixed absorption column for each group. In several cases, we observed an absorption increase within the central 20 kpc, but this analysis is complicated by the possible multiphase gas around the center. Nevertheless, it has little effect on any of our results. We also discuss the systematic error related to absorption in Section 9.

We used the MEKAL model to fit the spectra of the group emission. The free parameters are temperature, abundance, and normalization, once the absorption is determined. For spectra around the center, we also include a component to account for the LMXB emission from the cD galaxy. The LMXB component is represented by a power law with an index of 1.7, within D_{25} aperture obtained from HyperLeda. The total LMXB luminosity is fixed from the L_X–L_{Ks} relation derived in Kim & Fabbiano (2004), where L_{Ks} is the total K_s band luminosity of the cD from 2MASS. We also assume that the LMXB emission follows the K_s band light (see also Gilfanov 2004).

The projected group temperature profiles are shown in Figures 3–5. We used the algorithm determined by Vikhlinin (2006) to derive the deprojected temperature profiles in a parametric way, which was first applied in V06. The required inputs are the three-dimensional or deprojected profiles of gas density and abundance, and the projected temperature profile. V06 simply used the projected abundance profile as their sample is dominated by hot clusters. However, the emissivity of $\lesssim 2$ keV plasma is sensitive to the chemical abundances so the three-dimensional abundance profile is required for our work. We applied the nonparametric geometrical deprojection (summarized in e.g., Pizzolato et al. 2003; G07) to derive deprojected abundances in wider radial bins, generally merging 2–3 adjacent bins for the temperature profile. The deprojected abundance is an emission-weighted average in each bin so an effective radius in each bin is required. We define the effective radius as the emissivity weighted radius in each bin, where the plasma emissivity, $\varepsilon(T, Z, r)$, depends on the three-dimensional profiles of temperature, abundance, and density.

Since the determination of the three-dimensional profiles of temperature, abundance, and density depends on each other, iterations have to be done to derive the best-fit three-dimensional profiles. Usually at most three iterations are required to stabilize the best fits of these profiles. We assumed the following three-dimensional abundance profile:

$$Z(r) = Z_0 + Z_1 \exp(-(r/r_Z)^{\alpha_Z}). \tag{1}$$

This simple form can fit the abundance profiles of all groups in the sample. An example is shown in Figure 6 that represents the best-constrained three-dimensional abundance profile in this sample (thus the most difficult to fit, as the errors are the smallest). Most groups in this sample only have three-dimensional abundances constrained in 3–5 bins with larger errors so good fits can always be achieved with this simple function. Once the best fits of all profiles are achieved, we applied 1000 Monte Carlo simulations to address the uncertainties of the three-dimensional abundance profile. The simulation is realized by scattering the three-dimensional abundance profile according to the measurement errors. In this process, to be conservative, we also include an uncertainty of 10% of the bin size on the effective radius of each bin for the abundance profile. Thus, besides the best-fit three-dimensional abundance profile, we have 1000 simulated profiles to cover the error ranges, which will be used to estimate the uncertainties of the three-dimensional temperature and density profiles.
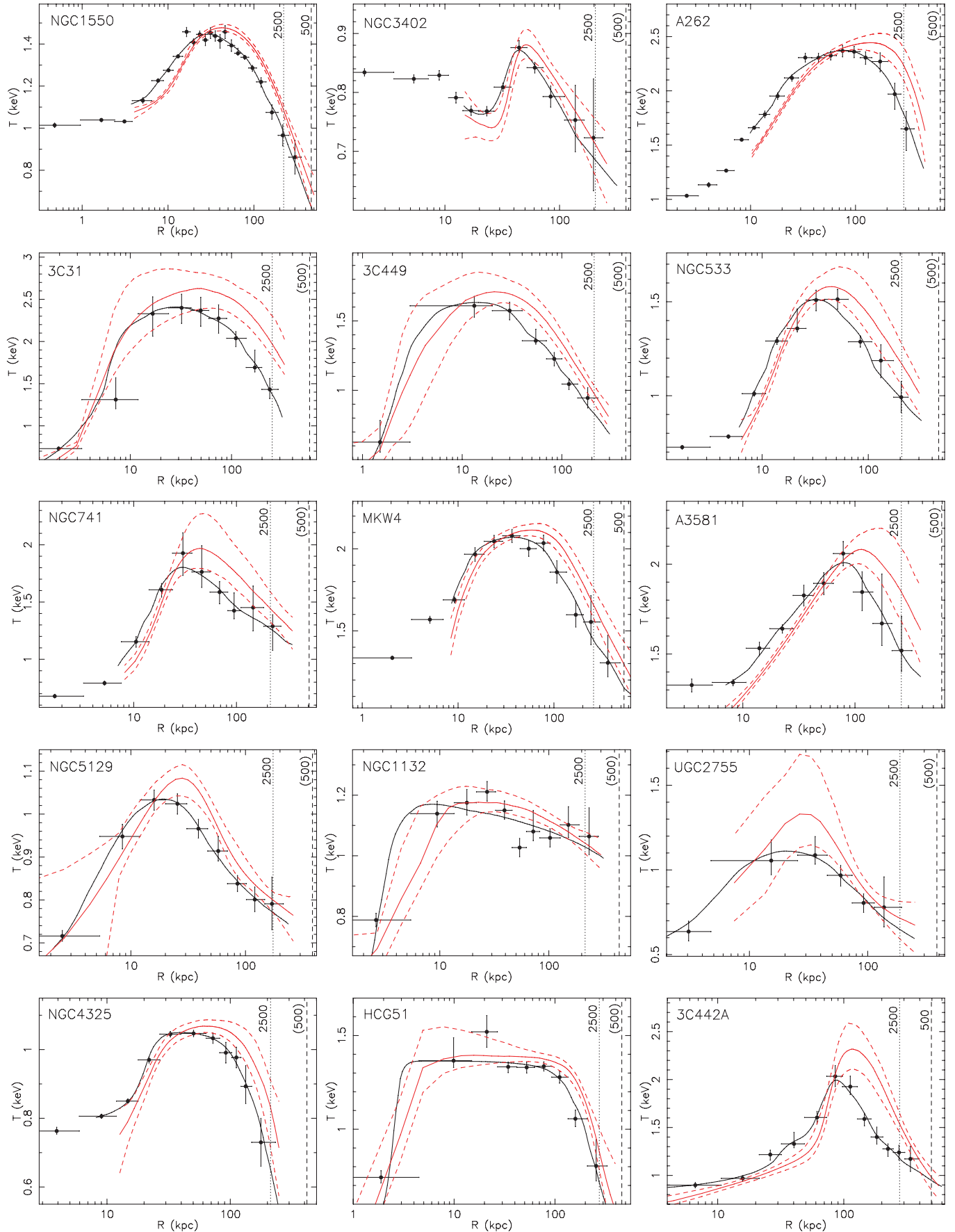
Figure 3. Temperature profiles of 43 groups in our sample. The solid and dashed curves are the reconstructed three-dimensional temperature profile with the 1σ errors, derived from 1000 simulations. The dashed-dotted line is the best-fit projected temperature profile. The effective radius of each bin for the projected temperature profile is derived by weighting the projected emissivity profile with the actual spatial coverage of the each bin. r_{2500} and r_{500} are marked. The r_{500} in parentheses is estimated from the $M_{500}-T_{500}$ relation.

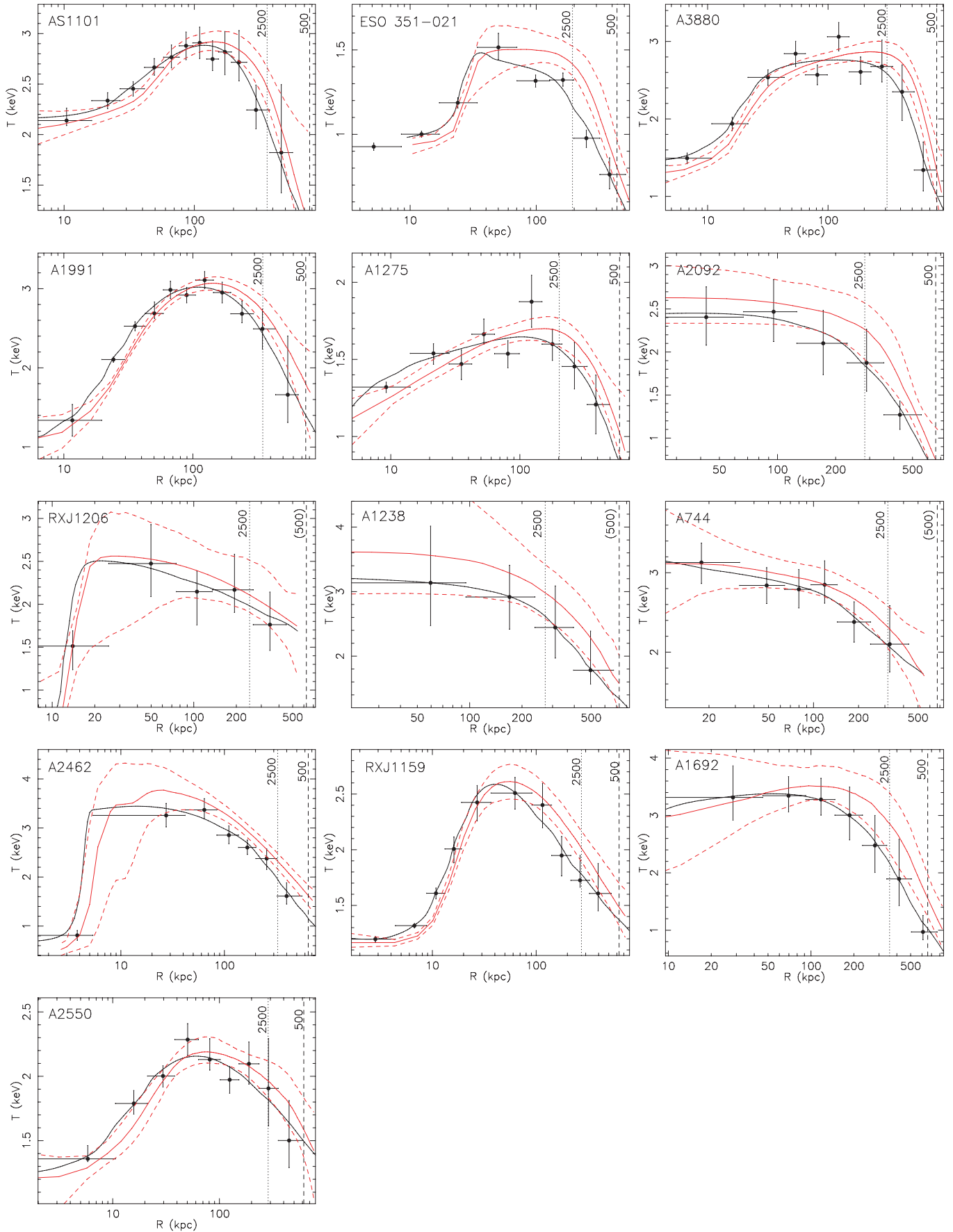(A color version of this figure is available in the online journal.)
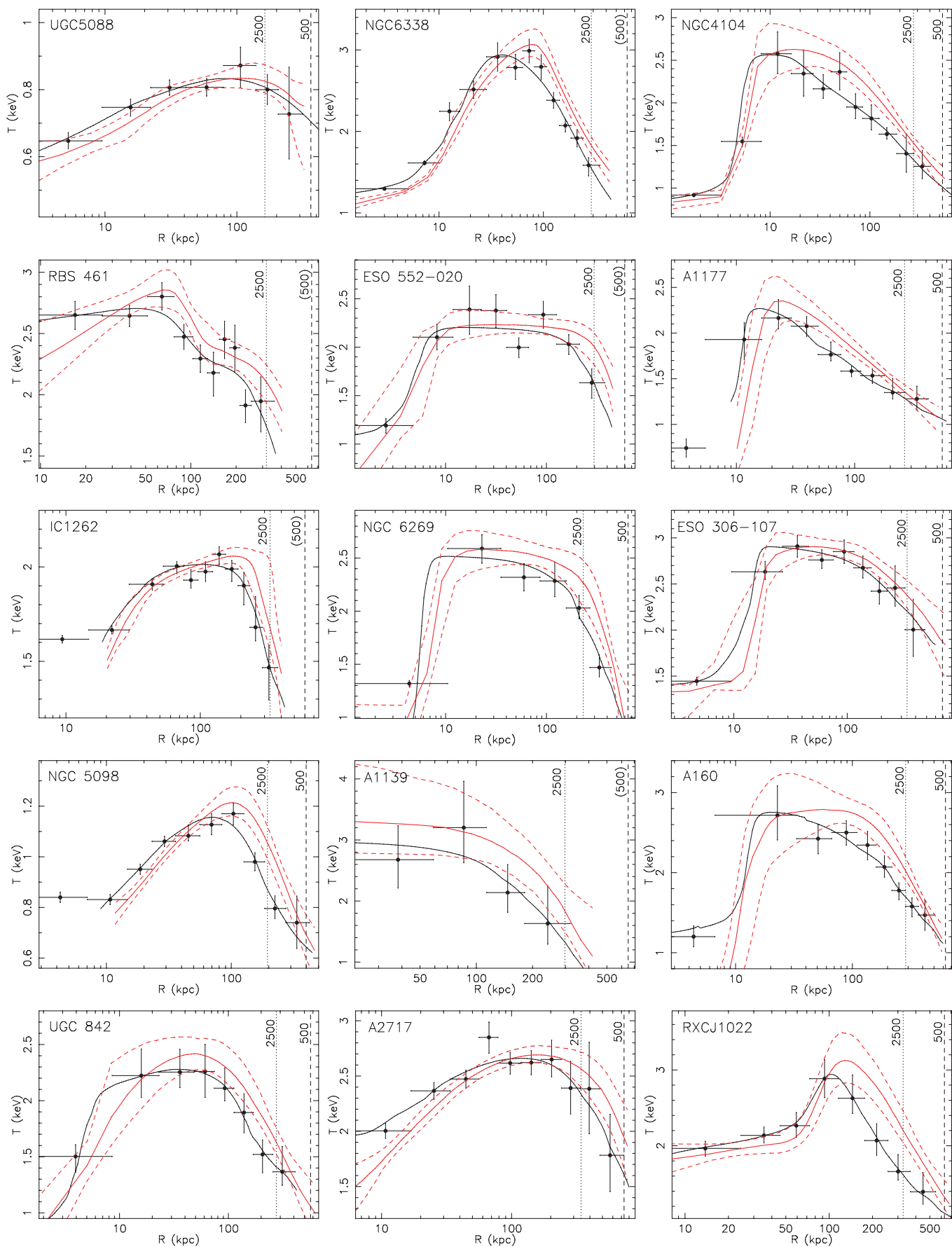
Figure 4. Continue from Figure 3.

(A color version of this figure is available in the online journal.)

Figure 5. Continue from Figure 4.

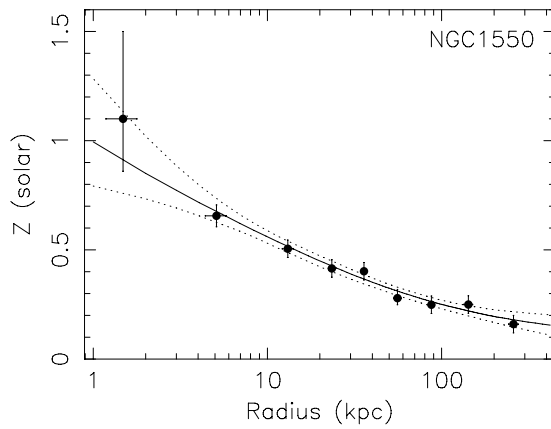(A color version of this figure is available in the online journal.)

Figure 6. Best constrained three-dimensional abundance profile in this sample with the best parametric fit (Section 3.3) and 1σ errors from 1000 simulations. The 1000 simulated abundance profiles are all used to derive 1000 simulated temperature and density profiles. As errors of other abundance profiles in this sample are larger and there are fewer bins, our simple three-dimensional abundance model (Section 3.3) always fits well beyond the central 10 kpc.

We used the same form of the three-dimensional temperature profile as used in V06:

$$T(r) = \frac{T_0(r/r_{\text{cool}})^{a_{\text{cool}}} + T_{\min}}{(r/r_{\text{cool}})^{a_{\text{cool}}} + 1} * \frac{(r/r_t)^{-a}}{[1 + (r/r_t)^b]^{c/b}}. \quad (2)$$

The exceptions are A1139, A1238, and A2092, which are faintest 2–3 keV systems in this sample so the errors on temperatures are large. Their three-dimensional temperature profiles are modeled as: $T(r) = T_0[1 + (r/r_t)^a]^{b/a}$, which fits their temperature profiles very well (Figures 4 and 5). The inner boundary of the fit is 5–20 kpc, depending on the quality of the fits at the center. As we focus on properties at large radii, the detailed choice of the inner boundary (5–20 kpc) is not a concern. Because the sizes of bins at large radii are not small, each bin is further divided into six subbins. The temperature modeling is done at the center of each subbin, only added up (with the algorithm by Vikhlinin 2006) at the end to obtain the expected temperature for each original bin of spectral analysis. In this way, the binsize effect is minimized and we don't need to worry about the accurate determination of effective radius for each radial bin, as most previous work had to address. The uncertainty of the three-dimensional temperature profile is derived from 1000 Monte Carlo simulations. In each simulation, the measured projected temperature profile is scattered according to the measurement errors, and a new simulated abundance profile is input. The density profile is fixed at the best-fit value, as the temperature error is the dominant error source. The reconstructed three-dimensional temperature profiles, with 1σ uncertainties from simulations, are also shown in Figures 3–5. There are groups where a central corona exists (e.g., Sun et al. 2007), so naturally the temperature gradient at 5–20 kpc is large in these cases (e.g., A2462, A160, ESO 306-107, HCG 51, and NGC 6269). Sometimes the three-dimensional temperature appears too low within 5–10 kpc radius (e.g., A160 and NGC 6269), which however affects none of our results in this work as core properties are excluded.

3.4. Gas Density

We extract the surface brightness profile in the 0.7–2 keV band, as suggested by V06 to avoid the 0.6 keV hump in the soft CXB. Point sources and chip gaps are excluded. The

scaled stowed background is subtracted so only the group emission and the local CXB is left. Some previous analysis on a surface brightness profile involved the correction of a single exposure map. However, the *Chandra* exposure map is energy and position dependent. It is not accurate to use a single exposure map (even one convolved with the group spectrum) as there is spectral variation in a group. The most accurate approach is to generate response files for each bin of the surface brightness and convert the raw count rate (without corrections on vignetting and other response) to density, from the derived three-dimensional temperature and abundance profiles and response files. To achieve that, we use XSPEC to generate an MEKAL emissivity matrix that depends on temperature, abundance and position of the radial bin for surface brightness (or response files there), once the absorption is determined. The ranges for temperatures and abundances cover the observed ranges for any particular group. This emissivity matrix provides the conversion factor needed to transfer the observed count rate to the emission measure. We assume the following density model (with 11 free parameters):

$$n_e^2 = n_0^2 \frac{(r/r_c)^{-\alpha}}{[1 + (r/r_c)^2]^{3\beta - \alpha/2}} \frac{1}{[1 + (r/r_s)^\gamma]^{\delta/\gamma}} + n_{02}^2 [1 - (r/r_{c2})^{\alpha_2}]^{3\beta_2/\alpha_2} \ (r < r_{c2}) \quad (3)$$

This model combines the profile used in V06 and the profile proposed by Ettori (2000) for cool cores. We find that this model provides very good fits for all groups in our sample. The density profile is then converted to the emissivity profile from the emissivity matrix. The emissivity profile is then projected along line of sight with the formula of geometrical deprojection (e.g., McLaughlin 1999). The local CXB can be added later with the known CXB spectra and the radial set of the response files. The resulting surface brightness profile can be compared with the observed one. To avoid the binsize effect that may especially affect outskirts as wider bins are required there, we further divide bins within 100 kpc to three subbins and bins beyond the central 100 kpc to six subbins. The conversion and deprojection are done in these subbins. They are later merged to compare with the observed profile. The density errors are estimated from 1000 Monte Carlo simulations, with 1000 corresponding simulated abundance and temperature profiles as inputs.

This method is similar to that used in V06, but we use the three-dimensional temperature and abundance profiles to convert count rates to density. Like V06, we also analyzed the *ROSAT* PSPC pointed observations for the purpose of constraining gas density profiles at large radii. The inclusion of the PSPC data is especially useful to $z < 0.04$ groups. We used the software developed by Snowden et al. (1994) to produce flat-fielded PSPC images in the 0.7–2 keV band (more exactly, R567 bands, or PI channels of 70–201). The images are further analyzed as described in Vikhlinin et al. (1999). Seventeen groups have sufficiently long PSPC data (listed in Table 1 with effective exposure), and we included the PSPC surface brightness profile in the modeling of the density profile. The probed outermost radius of the PSPC data for each group is listed in Table 2. We only used the PSPC surface brightness profiles outside the central 3′ to avoid the point-spread function (PSF) correction in the core. In all cases, there is good agreement between the *Chandra* and PSPC surface brightness data. One example is shown in Figure 7.

Table 3
Derived Properties of Groups (I. Temperature, Mass and Gas Fraction)

Group	T_{500}[a] (keV)	T_{2500} (keV)	r_{500}[a] (kpc)	r_{2500} (kpc)	M_{500}[a] ($10^{13}\,M_\odot$)	$f_{\rm gas,500}$[a]	$f_{\rm gas,2500}$	$f_{\rm gas,2500-500}$[a]	c_{500}[b]
NGC 1550	1.06 ± 0.02*	1.18 ± 0.02	465^{+15}_{-19}*	222 ± 6	$3.18^{+0.32}_{-0.37}$*	$0.097^{+0.012}_{-0.009}$*	0.056 ± 0.003	$0.149^{+0.033}_{-0.024}$*	$4.93^{+0.50}_{-0.46}$ (10)
NGC 3402	(0.74 ± 0.03)	0.80 ± 0.02	(380)	205^{+62}_{-22}			$0.032^{+0.008}_{-0.014}$		
A262	$(1.94^{+0.11}_{-0.15})$	$2.18^{+0.06}_{-0.07}$	(644)	288^{+17}_{-16}			$0.064^{+0.005}_{-0.007}$		$3.48^{+0.49}_{-0.45}$ (9)
NGC 383	$(1.67^{+0.13}_{-0.11})$	$1.89^{+0.17}_{-0.10}$	(593)	252^{+35}_{-20}			$0.031^{+0.003}_{-0.004}$		$3.09^{+1.84}_{-1.30}$ (6)
3C 449	$(0.97^{+0.04}_{-0.05})$	1.08 ± 0.04	(437)	211^{+11}_{-21}			$0.041^{+0.006}_{-0.004}$		$2.97^{+2.60}_{-1.64}$ (5)
NGC 533	$(1.06^{+0.08}_{-0.07})$	$1.21^{+0.06}_{-0.07}$	(461)	207^{+18}_{-29}			$0.031^{+0.005}_{-0.004}$		$4.58^{+3.90}_{-2.34}$ (5)
NGC 741	$(1.27^{+0.08}_{-0.12})$	$1.37^{+0.08}_{-0.12}$	(510)	214^{+20}_{-14}			$0.026^{+0.004}_{-0.003}$		$3.05^{+1.68}_{-1.22}$ (6)
MKW4	1.58 ± 0.09	$1.75^{+0.05}_{-0.04}$	538^{+24}_{-29}	259^{+12}_{-8}	$4.85^{+0.71}_{-0.68}$	0.086 ± 0.009	$0.047^{+0.002}_{-0.003}$	$0.134^{+0.38}_{-0.26}$	$3.93^{+1.16}_{-0.78}$ (7)
A3581	$(1.68^{+0.10}_{-0.09})$	$1.85^{+0.12}_{-0.07}$	(593)	259^{+22}_{-17}			$0.067^{+0.006}_{-0.007}$		$7.43^{+2.06}_{-1.40}$ (6)
NGC 5129	(0.76 ± 0.03)	0.83 ± 0.02	(384)	174^{+7}_{-9}			$0.035^{+0.004}_{-0.003}$		$3.43^{+1.72}_{-1.22}$ (5)
NGC 1132	(0.99 ± 0.04)	1.08 ± 0.03	(442)	215 ± 11			$0.039^{+0.005}_{-0.002}$		$1.77^{+0.70}_{-0.58}$ (6)
UGC 2755	(0.76 ± 0.05)	$0.83^{+0.05}_{-0.05}$	(384)	188^{+11}_{-12}			0.031 ± 0.005		
NGC 4325	(0.89 ± 0.03)	0.97 ± 0.03	(418)	212 ± 31			$0.037^{+0.014}_{-0.007}$		$5.19^{+3.68}_{-2.36}$ (7)
HCG 51	$(1.06^{+0.04}_{-0.03})$	$1.15^{+0.04}_{-0.03}$	(460)	275^{+13}_{-14}			0.028 ± 0.003		$2.11^{+0.89}_{-0.56}$ (6)
3C 442A	1.34 ± 0.04*	$1.61^{+0.05}_{-0.06}$	495^{+12}_{-16}*	277^{+16}_{-15}	$3.90^{+0.22}_{-0.40}$*	$0.068^{+0.006}_{-0.003}$*	$0.028^{+0.003}_{-0.002}$	$0.230^{+0.210}_{-0.060}$*	
UGC 5088	0.81 ± 0.03*	$0.83^{+0.02}_{-0.03}$	364^{+27}_{-19}*	163^{+10}_{-8}	$1.48^{+0.36}_{-0.24}$*	$0.049^{+0.008}_{-0.010}$*	0.029 ± 0.003	$0.067^{+0.021}_{-0.013}$*	$4.15^{+1.66}_{-1.16}$ (5)
NGC 6338	$(1.92^{+0.06}_{-0.07})$	2.14 ± 0.05	(636)	288^{+13}_{-11}			0.053 ± 0.003		$5.27^{+2.66}_{-1.80}$ (8)
NGC 4104	$1.41^{+0.09}_{-0.06}$*	$1.64^{+0.05}_{-0.08}$	535^{+19}_{-20}*	274 ± 12	$4.85^{+0.55}_{-0.53}$*	$0.069^{+0.009}_{-0.006}$*	0.036 ± 0.003	$0.137^{+0.043}_{-0.025}$*	$4.29^{+1.58}_{-1.12}$ (7)
RBS 461	(1.93 ± 0.10)	2.17 ± 0.06	(637)	318^{+25}_{-27}			0.059 ± 0.006		$5.45^{+1.32}_{-1.16}$ (9)
ESO 552-020	$(1.72^{+0.13}_{-0.09})$	1.97 ± 0.09	(598)	297^{+27}_{-24}			0.039 ± 0.005		$4.27^{+1.84}_{-1.22}$ (5)
A1177	$1.37^{+0.06}_{-0.07}$*	$1.48^{+0.06}_{-0.07}$	550^{+29}_{-27}*	264^{+20}_{-25}	$5.28^{+0.84}_{-0.73}$*	$0.060^{+0.009}_{-0.007}$*	0.037 ± 0.004	$0.091^{+0.033}_{-0.020}$*	$5.26^{+4.68}_{-2.61}$ (6)
IC 1262	$(1.73^{+0.06}_{-0.05})$	$1.91^{+0.06}_{-0.05}$	(600)	330^{+20}_{-40}			$0.045^{+0.004}_{-0.010}$		
NGC 6269	$1.72^{+0.12}_{-0.11}$*	$2.16^{+0.08}_{-0.10}$	645^{+50}_{-52}*	232^{+27}_{-21}	$8.49^{+1.97}_{-2.01}$*	$0.076^{+0.011}_{-0.010}$*	$0.044^{+0.003}_{-0.004}$	$0.087^{+0.027}_{-0.015}$*	
ESO 306-017	$2.37^{+0.12}_{-0.14}$*	$2.54^{+0.08}_{-0.10}$	690^{+44}_{-30}*	337^{+16}_{-14}	$10.3^{+2.1}_{-1.3}$*	$0.081^{+0.010}_{-0.011}$*	$0.052^{+0.003}_{-0.004}$	$0.119^{+0.031}_{-0.026}$*	
NGC 5098	0.96 ± 0.04	$1.05^{+0.02}_{-0.03}$	398^{+17}_{-33}	195^{+17}_{-13}	$2.00^{+0.28}_{-0.46}$	$0.108^{+0.018}_{-0.012}$	$0.048^{+0.006}_{-0.004}$	$0.205^{+0.131}_{-0.060}$	$4.29^{+1.46}_{-1.06}$ (7)
A1139	$(2.01^{+0.33}_{-0.34})$	$2.20^{+0.35}_{-0.33}$	(650)	298^{+37}_{-36}			$0.026^{+0.016}_{-0.008}$		
A160	$1.68^{+0.10}_{-0.10}$	$2.05^{+0.07}_{-0.06}$	626^{+27}_{-31}	286^{+25}_{-23}	$7.90^{+1.06}_{-1.10}$	$0.085^{+0.009}_{-0.008}$	$0.043^{+0.003}_{-0.004}$	$0.121^{+0.038}_{-0.023}$	$2.73^{+0.70}_{-0.60}$ (8)
UGC 842	$1.54^{+0.14}_{-0.12}$*	1.78 ± 0.09	570^{+84}_{-45}*	276^{+23}_{-29}	$5.60^{+2.60}_{-1.10}$*	$0.056^{+0.012}_{-0.014}$*	0.032 ± 0.003	$0.089^{+0.041}_{-0.041}$*	$6.06^{+3.31}_{-2.19}$ (6)
A2717	$2.43^{+0.13}_{-0.12}$	$2.60^{+0.08}_{-0.09}$	732^{+49}_{-32}	342^{+13}_{-11}	$12.9^{+2.7}_{-1.7}$	0.076 ± 0.010	0.053 ± 0.003	$0.098^{+0.029}_{-0.025}$	$2.15^{+0.36}_{-0.32}$ (9)
RXJ 1022+3830	$1.94^{+0.20}_{-0.14}$	$2.36^{+0.17}_{-0.12}$	631^{+32}_{-41}	326^{+25}_{-23}	$8.00^{+1.31}_{-1.40}$	$0.075^{+0.007}_{-0.013}$	$0.038^{+0.004}_{-0.005}$	$0.134^{+0.074}_{-0.046}$	$4.03^{+1.24}_{-0.80}$ (6)
AS1101	$2.57^{+0.14}_{-0.11}$*	$2.69^{+0.10}_{-0.09}$	768^{+90}_{-65}*	362^{+21}_{-18}	$14.1^{+5.0}_{-3.4}$*	$0.114^{+0.021}_{-0.020}$*	0.085 ± 0.008	$0.129^{+0.088}_{-0.041}$*	$5.05^{+2.37}_{-1.34}$ (10)
ESO 351-021	$1.14^{+0.07}_{-0.04}$	$1.34^{+0.07}_{-0.03}$	437^{+78}_{-38}	194^{+28}_{-35}	$3.22^{+1.80}_{-0.90}$	$0.074^{+0.013}_{-0.018}$	$0.036^{+0.007}_{-0.005}$	$0.119^{+0.066}_{-0.050}$	$2.42^{+1.20}_{-0.76}$ (6)
A3880	$2.49^{+0.14}_{-0.12}$	2.75 ± 0.11	799^{+89}_{-68}	309^{+24}_{-12}	$14.9^{+5.0}_{-3.5}$	$0.088^{+0.016}_{-0.021}$	$0.074^{+0.005}_{-0.007}$	$0.090^{+0.047}_{-0.022}$	$4.03^{+1.54}_{-1.26}$ (8)
A1991	$2.68^{+0.10}_{-0.08}$	2.86 ± 0.07	749^{+45}_{-35}	348^{+13}_{-10}	$13.4^{+2.5}_{-1.9}$	$0.094^{+0.010}_{-0.012}$	0.066 ± 0.004	$0.115^{+0.038}_{-0.022}$	$4.69^{+0.76}_{-0.70}$ (9)
A1275	$1.46^{+0.08}_{-0.07}$*	$1.63^{+0.06}_{-0.07}$	592^{+87}_{-59}*	202^{+12}_{-9}	$6.90^{+3.00}_{-1.67}$*	$0.094^{+0.018}_{-0.031}$*	0.069 ± 0.004	$0.100^{+0.032}_{-0.035}$*	$4.10^{+1.69}_{-1.27}$ (7)
A2092	$1.67^{+0.13}_{-0.12}$*	$2.14^{+0.17}_{-0.21}$	659^{+45}_{-40}*	283^{+34}_{-24}	$8.95^{+1.81}_{-1.62}$*	0.078 ± 0.013*	$0.050^{+0.006}_{-0.007}$	$0.096^{+0.027}_{-0.020}$*	
RXJ 1206-0744	$(1.91^{+0.20}_{-0.21})$	$2.14^{+0.19}_{-0.21}$	(624)	248^{+28}_{-27}			$0.053^{+0.009}_{-0.007}$		
A1238	$(2.51^{+0.27}_{-0.32})$	$2.88^{+0.35}_{-0.36}$	(725)	272^{+63}_{-59}			0.035 ± 0.008		
A744	$(2.24^{+0.19}_{-0.16})$	2.49 ± 0.16	(681)	325^{+30}_{-24}			$0.046^{+0.005}_{-0.006}$		$3.33^{+1.66}_{-1.04}$ (6)
A2462	$2.32^{+0.12}_{-0.12}$	2.62 ± 0.09	646 ± 30	327^{+13}_{-12}	$8.80^{+1.29}_{-1.19}$	$0.099^{+0.011}_{-0.009}$	0.052 ± 0.003	$0.180^{+0.058}_{-0.034}$	$3.41^{+1.56}_{-0.84}$ (6)
RXJ 1159	$1.84^{+0.14}_{-0.08}$*	$2.12^{+0.09}_{-0.10}$	630^{+77}_{-30}*	273^{+15}_{-13}	$8.30^{+3.10}_{-1.12}$*	$0.065^{+0.007}_{-0.012}$*	0.042 ± 0.003	$0.080^{+0.019}_{-0.023}$*	$2.95^{+1.16}_{-0.90}$ (6)
A1692	$2.61^{+0.16}_{-0.24}$	$3.06^{+0.25}_{-0.22}$	658^{+64}_{-47}	356^{+42}_{-32}	$9.70^{+2.99}_{-1.91}$	$0.090^{+0.014}_{-0.020}$	0.043 ± 0.006	$0.216^{+0.155}_{-0.087}$	$5.46^{+1.77}_{-1.19}$ (7)
A2550	1.95 ± 0.10	2.05 ± 0.08	617^{+74}_{-27}	286 ± 9	$7.90^{+2.90}_{-1.00}$	$0.093^{+0.011}_{-0.016}$	$0.067^{+0.003}_{-0.004}$	$0.119^{+0.027}_{-0.038}$	$4.57^{+0.92}_{-0.76}$ (7)

Notes.

[a] The T_{500} in parenthesis are from the empirical relation between T_{1500} and T_{500} (Section 4). The r_{500} in parenthesis are estimated from the $M_{500}-T_{500}$ relation in this work. The values with an asterisk are for tier 2 groups from extrapolation.

[b] The value in parenthesis is the number of radial points between 40 kpc and $r_{\rm det,spe}$ (including 40 kpc and $r_{\rm det,spe}$) are used in the NFW fit (Section 7.3).

4. CHARACTERISTIC RADII AND DEFINITION OF SYSTEM TEMPERATURES

As stated above, we generated 1000 simulated profiles of the three-dimensional temperature, abundance, and density profiles, which cover the ranges of the measurement errors. Assuming hydrostatic equilibrium, each set of the three-dimensional temperature and density profiles determine a set of characteristic radii of the group (r_{500}, r_{1000}, r_{1500}, and r_{2500}). The profiles of interesting quantities, e.g., total mass, gas mass, and entropy, and their values at the characteristic radii are also determined. For each quantity, the peak in the distribution from 1000 simulations defines the most probable value (or "best fit"). The 1σ errors at two sides are estimated by determining the regions that contain 68% of realizations at each side. The results are listed in Tables 3 and 4. r_{500} is the basic characteristic radius that is used in most scaling relations in this work. However, it cannot be robustly determined for all groups in our sample so the $r_{500}-T$ scaling relation is required. As the radial coverage of data in

this sample differs from one group to another, we define four tiers of groups for which group properties (entropy, mass, Y_X, and gas fraction) are derived to different characteristic radius.

Tier 1. Groups with surface brightness (including the PSPC profile) derived at $> 2\sigma$ levels to $> r_{500}$ (note we are conservative to estimate the errors of the local CXB, see notes of Table 2) and a temperature profile derived to $> 80\%$ of r_{500}. Eleven groups in our sample are in this tier, and their temperature profiles are derived to 81%–117% of r_{500} with a median of 97%. Groups in this tier have density profiles derived to $> r_{500}$, so the density gradient at $\sim r_{500}$ is constrained. Temperature profiles are derived beyond r_{500} or sufficiently close to r_{500} for reasonable extrapolation. We note that in V06, there are three clusters and groups (A383, MKW4 and A1991) with temperature profiles derived only to 73%–89% of r_{500}, but properties at r_{500} are still derived from extrapolation. Thus, our criteria are similar to those in V06 and V09.
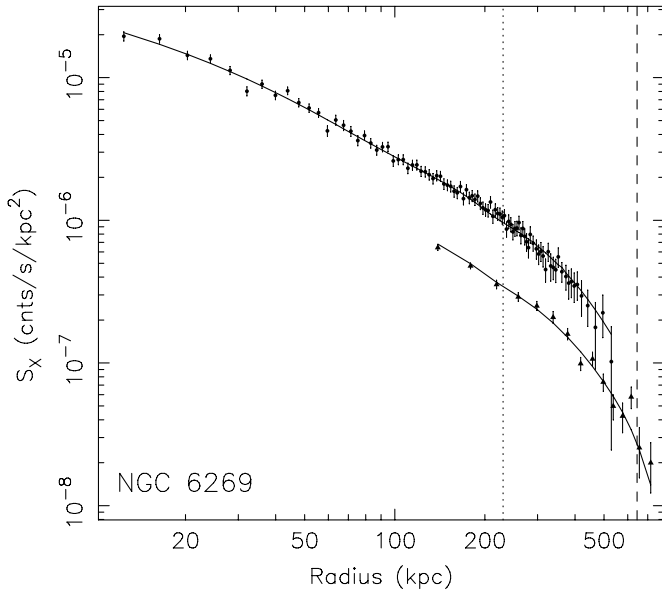
Figure 7. One example of the surface brightness profiles (*Chandra* + PSPC) with the best fits derived from the best-fit three-dimensional temperature and abundance profiles. The *Chandra* profile is the upper one, while the PSPC profile is the lower one. We generated response files for each *Chandra* radial bin. Note that the density errors are derived from 1000 Monte Carlo simulations with 1000 simulated three-dimensional temperature and abundance profiles folded in. The dashed and dotted lines mark r_{2500} and r_{500} (see Figure 4 for NGC 6269).

Tier 2. Groups with surface brightness and temperature profiles all derived to at least r_{1000} but not in tier 1. Twelve groups are in this tier, and their temperature profiles are derived to 68%–87% of r_{500} with a median of 77%. We consider that groups in this tier have properties well constrained close to r_{500}, so r_{500} is determined in these groups. Group properties at r_{500} are also derived from extrapolation. However, in figures of scaling relations at r_{500}, tier 2 groups are always marked differently from tier 1 groups. The fits with or without them are both listed.

Tier 3. Groups with surface brightness and temperature profiles derived to at least r_{1500} but not in tiers 1 and 2. Eleven groups are in this tier. Nine of them have temperature profiles derived to 52%–72% of r_{500}, which is close to r_{1000} ($\sim 0.73 r_{500}$ in this sample). Thus, group properties at r_{1000} are also derived from extrapolation. A1238 and RXJ 1206-0744 are put in this tier as the temperature and density errors are large, although r_{1000} is reached in both cases.

Tier 4. Nine other groups with surface brightness and temperature profiles derived to at least r_{2500}. Group properties at r_{1500} are also derived from extrapolation in this tier.

Previous X-ray work on clusters and groups often defined $\langle T \rangle$, which is the emission-weighted temperature within a certain aperture. As definitions are generally different, it is necessary to use an unified definition that is easily accessible from observations. In this work, we define the system temperature as follows.

T_{500}. The spectroscopic temperature measured from the integrated spectrum in the projected $0.15\,r_{500}$–r_{500} annulus.

We derive T_{500} by integrating the three-dimensional temperature profile from $0.15\,r_{500}$ to $1.6\,r_{500}$ (or $\sim r_{180}$), in an annular cylinder with projected radii of $0.15\,r_{500}$–r_{500} along the line of sight, with the algorithm by Vikhlinin (2006). The choice of the

Table 4
Derived Properties of Groups (II: Entropy)

Group	K_{500}[a]	K_{1000}[a]	K_{1500}[a]	K_{2500}	$K_{0.15r500}$	K_{30kpc}
NGC 1550	(297^{+46}_{-42})	253 ± 23	228 ± 15	198^{+9}_{-8}	94 ± 3	49 ± 1
NGC 3402			(278^{+218}_{-88})	226^{+100}_{-52}	66 ± 4	34 ± 2
A262		(385^{+87}_{-67})	383^{+73}_{-46}	354^{+43}_{-29}	161^{+9}_{-7}	69 ± 2
NGC 383			(495^{+83}_{-46})	448^{+71}_{-39}	327^{+23}_{-24}	214^{+28}_{-25}
3C 449			(217^{+28}_{-37})	199^{+22}_{-27}	158^{+11}_{-12}	96 ± 6
NGC 533		(336^{+52}_{-76})	317^{+45}_{-66}	289^{+44}_{-50}	171^{+13}_{-11}	103 ± 6
NGC 741		(460^{+64}_{-114})	428^{+57}_{-86}	388^{+53}_{-66}	243^{+36}_{-29}	146^{+15}_{-17}
MKW4	574^{+54}_{-96}	454^{+44}_{-39}	388^{+42}_{-39}	332^{+31}_{-24}	161 ± 6	80^{+3}_{-4}
A3581		(384^{+84}_{-78})	344^{+72}_{-59}	298^{+49}_{-41}	124 ± 7	38 ± 1
NGC 5129		(262^{+32}_{-30})	229^{+23}_{-22}	193^{+18}_{-17}	100 ± 6	75^{+6}_{-4}
NGC 1132			336^{+49}_{-45}	238 ± 26	97^{+7}_{-6}	68^{+9}_{-7}
UGC 2755			(260^{+65}_{-72})	211^{+50}_{-45}	120^{+15}_{-14}	113^{+24}_{-18}
NGC 4325			(195^{+86}_{-70})	179^{+46}_{-36}	84^{+7}_{-6}	39 ± 2
HCG 51		(371^{+196}_{-166})	348^{+120}_{-101}	303^{+49}_{-47}	126 ± 5	82 ± 4
3C 442A	(455^{+49}_{-77})	438^{+34}_{-49}	431^{+29}_{-40}	419^{+33}_{-37}	210^{+27}_{-26}	72 ± 8
UGC 5088	(414^{+91}_{-191})	326^{+48}_{-49}	288^{+32}_{-33}	230 ± 23	84^{+8}_{-7}	51^{+6}_{-4}
NGC 6338		(401^{+46}_{-45})	371^{+36}_{-35}	334^{+28}_{-23}	239^{+14}_{-11}	108 ± 5
NGC 4104	(571^{+74}_{-85})	471^{+42}_{-50}	421^{+32}_{-36}	360^{+26}_{-29}	221^{+16}_{-15}	148^{+12}_{-11}
RBS 461			(446^{+59}_{-56})	370^{+43}_{-41}	165 ± 8	93 ± 5
ESO 552-020		(580^{+107}_{-124})	550^{+79}_{-87}	460^{+58}_{-61}	190 ± 9	97^{+6}_{-5}
A1177	(648^{+130}_{-111})	480^{+74}_{-70}	397^{+48}_{-47}	317^{+28}_{-45}	179^{+11}_{-12}	138^{+13}_{-11}
IC 1262			(489^{+63}_{-99})	411^{+70}_{-63}	134 ± 4	47 ± 2
NGC 6269	(390^{+189}_{-183})	440^{+56}_{-68}	434^{+54}_{-50}	406^{+38}_{-40}	272^{+21}_{-21}	127^{+7}_{-8}
ESO 306-017	(914^{+203}_{-192})	700^{+108}_{-81}	596^{+74}_{-59}	475^{+44}_{-38}	191 ± 12	86 ± 6
NGC 5098	217 ± 43	210^{+28}_{-26}	205 ± 21	194^{+16}_{-17}	84^{+7}_{-8}	45 ± 2
A1139			(486^{+429}_{-206})	431^{+112}_{-100}	368^{+69}_{-48}	261^{+69}_{-43}
A160	477^{+86}_{-90}	429^{+34}_{-36}	407^{+29}_{-28}	379^{+33}_{-25}	268^{+17}_{-16}	172^{+31}_{-26}
UGC 842	(652^{+231}_{-149})	522^{+90}_{-77}	459^{+60}_{-58}	406^{+48}_{-39}	238^{+22}_{-20}	122^{+11}_{-9}
A2717	1022^{+163}_{-181}	817^{+106}_{-102}	673^{+71}_{-77}	502^{+40}_{-41}	186 ± 11	75 ± 5
RXJ 1022+3830	655^{+89}_{-94}	587^{+69}_{-64}	548^{+62}_{-51}	488^{+72}_{-46}	223^{+33}_{-30}	77^{+6}_{-7}
AS1101	(476^{+457}_{-218})	465^{+142}_{-91}	441^{+73}_{-53}	386^{+39}_{-36}	120^{+15}_{-13}	29 ± 1
ESO 351-021	309^{+105}_{-84}	315^{+85}_{-40}	310^{+58}_{-34}	289^{+35}_{-38}	175^{+19}_{-20}	57 ± 4
A3880	624^{+198}_{-236}	681^{+103}_{-98}	560^{+88}_{-52}	420^{+44}_{-35}	176 ± 20	50 ± 3
A1991	752^{+252}_{-275}	653^{+95}_{-142}	568^{+68}_{-94}	463^{+43}_{-63}	166^{+11}_{-23}	39 ± 1
A1275	(464^{+278}_{-98})	324^{+66}_{-30}	284^{+23}_{-30}	231^{+18}_{-17}	130^{+16}_{-15}	59 ± 3
A2092	(423^{+192}_{-140})	449^{+90}_{-66}	439^{+85}_{-69}	401^{+69}_{-57}	202^{+24}_{-21}	200^{+57}_{-34}
RXJ 1206-0744		432^{+97}_{-104}	402^{+80}_{-80}	354^{+68}_{-67}	201^{+34}_{-41}	102^{+32}_{-35}
A1238		805^{+347}_{-165}	676^{+167}_{-113}	584^{+114}_{-91}	464^{+129}_{-76}	341^{+200}_{-78}
A744		(695^{+249}_{-220})	580^{+134}_{-115}	470^{+72}_{-63}	215^{+16}_{-15}	115^{+12}_{-11}
A2462	627^{+102}_{-118}	537^{+79}_{-77}	488^{+62}_{-60}	422^{+48}_{-40}	247^{+12}_{-13}	172^{+20}_{-21}
RXJ 1159	(800^{+200}_{-121})	580^{+78}_{-56}	491^{+49}_{-40}	410^{+35}_{-28}	230^{+16}_{-17}	92 ± 6
A1692	622^{+202}_{-176}	644^{+186}_{-167}	636^{+174}_{-156}	576^{+126}_{-120}	252 ± 29	149^{+30}_{-24}
A2550	704^{+132}_{-128}	530^{+65}_{-67}	431^{+46}_{-45}	331^{+27}_{-26}	114^{+11}_{-8}	46 ± 3

Note. [a] The values in parentheses are from extrapolation (see Section 4).

outer radius in the three-dimensional integration little affects T_{500} as it is emission weighted. The same definition of the system temperature was also used in Nagai et al. (2007b, NKV07 hereafter), Maughan (2007) and V09. This definition excludes the central region, where a cool core or a locally heated region may exist. Indeed the group temperature profiles are much more similar at $r > 0.15 r_{500}$ (Section 5 and Figure 8). This temperature can also be directly derived from data, provided that the full coverage of r_{500} is achieved (generally not the case for groups in our sample). Similarly, we can define T_{1000}, T_{1500}, and T_{2500}, with the projected inner boundary always at $0.15\,r_{500}$ and the projected outer boundary at r_{1000}, r_{1500}, and r_{2500} respectively (three-dimensional temperature profile still integrated to $1.6\,r_{500}$). Their empirical relations can also be determined.

As we cannot derive r_{500} for groups in tiers 3 and 4, the r_{500}–T_{500} relation needs to be determined. The r–T relation is just a manifestation of the M–T relation, so it is presented in Section 7.1. We also derived the average ratios of the characteristic radii from 23 tiers 1 and 2 groups: $r_{1000}/r_{500} = 0.741 \pm 0.013$, $r_{1500}/r_{500} = 0.617 \pm 0.011$, and $r_{2500}/r_{500} = 0.471 \pm 0.009$, which are about what are expected for the average c_{500} of this sample (~ 4.2, Section 7.3), 0.727, 0.599, and 0.465 respectively (assuming an NFW profile).
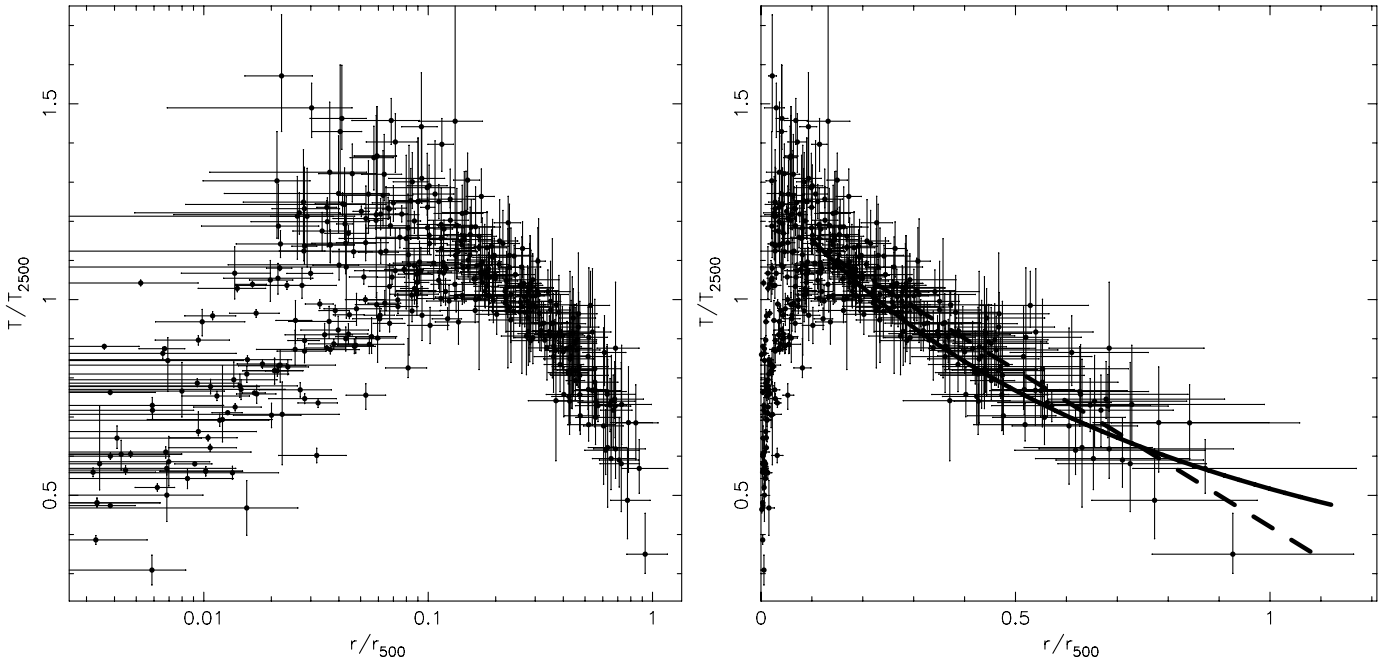
Figure 8. Temperature profiles in the logarithmic and linear scales of r_{500}. Temperatures are scaled by T_{2500}. Despite the large scatter at small radii, the temperature profiles outside of $0.2\,r_{500}$ are generally similar. The thick solid line in the linear plot is the universal temperature profile (also projected) derived from the simulations in Loken et al. (2002). We simply used T_{2500} to replace T_0 in Loken et al. (2002). Good agreement can be seen even though the normalization is not adjusted. The thick dashed line is a simple linear fit to the data (see Section 5).

We also need empirical relations between T_{500} and T_{1500} (or T_{2500}) to estimate T_{500} for groups in tiers 3 and 4. For 23 groups in the first and second tiers, we found

$$kT_{500}/kT_{1500} = 0.93 \pm 0.02. \qquad (4)$$

This ratio is not temperature dependent in our sample, and the fit is very good ($\chi^2/\text{dof} = 6.6/22$). If we only fit 11 groups in the first tier, the ratio is the same. We note that V09 derived a similar empirical relation between T_{500} and temperature measured at 0.15–$0.5\,r_{500}$ (close to our T_{2500}). V09 also included a linear term as they explored a wider temperature range. We also derived $kT_{500}/kT_{2500} = 0.89 \pm 0.02$, but the scatter is larger as shown by the poorer fit ($\chi^2/\text{dof} = 18.6/22$). The empirical relation between kT_{500} and kT_{1500}, combined with the r_{500}–T_{500} scaling, allows us to estimate r_{500} for groups in tiers 3 and 4 in a few iterations. We specifically used the r_{500}–T_{500} relation from 23 tiers 1 and 2 groups and 14 clusters in V06 and V09 (the fourth row of Table 6). For reference, we also give the best fit of the r_{2500}–T_{500} relation for all 43 groups in this sample: $(E(z)r_{2500}/155 \pm 4\,\mathrm{h}^{-1}\,\mathrm{kpc}) = (T_{500}/1\,\mathrm{keV})^{0.520\pm0.040}$, which is similar to the V06 result, $(E(z)r_{2500}/146 \pm 3\,\mathrm{h}^{-1}\,\mathrm{kpc}) = (T_{500}/1\,\mathrm{keV})^{0.547\pm0.020}$.

5. TEMPERATURE PROFILES

Scaled temperature profiles for these groups are shown in Figure 8 in logarithmic and linear scales. We scale temperatures with T_{2500}, which is robustly determined for each group. While the scatter within the central $0.15\,r_{500}$ is large, the group temperature profiles are more similar beyond $0.15\,r_{500}$, with a declining slope similar to that predicted from simulations (e.g., Loken et al. 2002). From $0.15\,r_{500}$ to $\sim r_{500}$, we can fit the projected temperature profiles with this simple form

$$T/T_{2500} = (1.22 \pm 0.02) - (0.79 \pm 0.04)r/r_{500}. \qquad (5)$$

Interestingly, V05 derived an average form of $T/<T> = 1.22$–$1.2r/r_{180}$ ($0.125 < r/r_{180} < 0.6$) for 13 systems in their sample, which is very similar to ours as $r_{500} \sim 0.62r_{180}$. If we use a similar form as used in Loken et al. (2002), we can also fit the projected temperature profiles at $0.15\,r_{500}$–r_{500} with this form

$$T/T_{2500} = (1.37 \pm 0.03)(1 + r/r_{500})^{-(1.34\pm0.21)}. \qquad (6)$$

Based on *ASCA* data, Markevitch et al. (1998) first suggested that temperature profiles of clusters are self-similarly declining with radius. This result was later confirmed by De Grandi & Molendi (2002) with the *BeppoSAX* data, and by V05 with the *Chandra* data, and by Piffaretti et al. (2005), Pratt et al. (2007), and Leccardi & Molendi (2008, LM08 hereafter) with the XMM-*Newton* data. Self-similarly declining temperature profiles are also generally observed in simulations (e.g., Loken et al. 2002; Borgani et al. 2004; Kay et al. 2004). The self-similar decline in groups was also suggested by Sun et al. (2003), G07, and Rasmussen & Ponman (2007). Our group sample is the largest one so far with detailed studies. As shown in Figure 8, group temperature profiles are generally self-similar with a slope consistent with that in simulations, although there is some scatter. We also combine all data points to make a mean temperature profile (Figure 9). Figure 9 also plots the mean temperature profile of hot clusters at $z = 0.1$–0.3 from LM08, as well as the mean temperature profile of 1–3 keV systems from the Borgani et al. (2004) simulations. We do not plot the mean temperature profiles from De Grandi & Molendi (2002), V05, and Pratt et al. (2007), but they are close to LM08's (Figure 21 in LM08). Clearly, the group temperature profiles are more peaky than those of clusters, starting to decline at $\sim 0.2r_{500}$, where the mean cluster temperature profile is still flat. This difference was also noticed by V06. The group temperature profiles actually agree more with simulations (e.g., Loken et al. 2002; Borgani et al. 2004), which generally have problems explaining the flat

Relation	K_1 (keV cm^2)	α
K_{500}–T_{500} (tier 1)	286 ± 60	1.12 ± 0.28
K_{500}–T_{500} (tiers 1+2)	356 ± 45	0.825 ± 0.200
K_{1000}–T_{500} (tiers 1+2+3)	310 ± 19	0.832 ± 0.100
K_{1500}–T_{500} (all groups)	288 ± 14	0.790 ± 0.078
K_{2500}–T_{2500} (all groups)	230 ± 10	0.760 ± 0.061
$K_{0.15r500}$–T_{2500} (all groups)	114 ± 9	0.778 ± 0.124
K_{30kpc}–T_{2500} (all groups)	68 ± 9	0.459 ± 0.229
K_{500}–T_{500} (tier 1 + clusters)	286 ± 23	1.08 ± 0.05
K_{500}–T_{500} (tiers 1+2 + clusters)	329 ± 25	0.994 ± 0.054
K_{1000}–T_{500} (tiers 1+2+3 + clusters)	303 ± 13	0.887 ± 0.034
K_{2500}–T_{500} (all groups + clusters)	252 ± 8	0.740 ± 0.027
$K_{0.15r500}$–T_{500} (all groups + clusters)	137 ± 9	0.494 ± 0.047

Note. [a] $E(z)^{4/3} K = K_1 (T/1\,\mathrm{keV})^{\alpha}$, where K_1 is the corresponding entropy at 1 keV. The last four relations include 14 clusters from V06 and V09. There is little correction between K_{30kpc} and T_{2500}, but we still list it for the studies of intrinsic scatter (Figure 11). We used the Bivariate Correlated Errors and Intrinsic Scatter (BCES) (Y|X) regression (Akritas & Bershady 1996) as the temperature errors are smaller than the entropy errors.

temperature profiles of clusters at $0.15r_{500}$–$0.3r_{500}$ (e.g., Borgani et al. 2004).

6. ENTROPY

The ICM entropy, defined as $K = T/n_e^{2/3}$, is a fundamentally important quality of the ICM as summarized in Voit (2005). Entropy records the thermodynamic history of the ICM, as nongravitational processes (e.g., AGN heating, cooling and star formation) deviate the entropy relations from the self-similar relations determined with only gravity and accretion shocks (e.g., Ponman et al. 1999; Voit & Bryan 2001). Voit et al. (2005, VKB05 hereafter) derived the baseline ICM entropy profile from simulations in the absence of nongravitational processes, $K(r)/K_{200,\mathrm{adi}} = 1.32(r/r_{200})^{1.1}$. $K_{200,\mathrm{adi}}$ is an entropy scale of a nonradiative cluster at r_{200} (VKB05). This baseline entropy profile can be compared with our observational results to measure the impact of nongravitational processes on the ICM. With a weighted average of ~ 4.2 for c_{500} in this sample (Section 7.3), $r_{500}/r_{200} = 0.669$ for an NFW mass profile and the baseline entropy relation is converted to $K(r)/K_{500,\mathrm{adi}} = 1.40(r/r_{500})^{1.1}$ (note that we use $K_{500,\mathrm{adi}}$ here for the adiabatic entropy scale at r_{500}, see the definition of $K_{200,\mathrm{adi}}$ in VKB05 and Voit 2005). For the cosmology assumed in this paper and a baryon fraction (f_b) of 0.165 (Komatsu et al. 2009),

$$K_{500,\mathrm{adi}} = 342\ \mathrm{keV cm^2} \left(\frac{M_{500}}{10^{14} M_\odot}\right)^{2/3} E(z)^{-2/3} h_{73}^{-4/3}. \quad (7)$$

Note that $K_{500,\mathrm{adi}}$ has a different h dependence from the observed entropy $\left(K \propto h_{73}^{-1/3}\right)$. From the derived temperature and density profiles, we obtained entropy profiles for each group. The best-fit scaled entropy profiles are shown in Figure 10. Substantial scatter is present within 0.3–$0.4\ r_{500}$. As Figure 10 is basically a plot showing the large scatter of the density profiles, it is clear that there is a wide range of X-ray luminosities in this sample, which is also implied by the K–T relations shown next. We discuss the ICM entropy of these groups in the following three sections.

6.1. K–T Relations

We first examined the K–T relations at 30 kpc, $0.15\ r_{500}$, r_{2500}, r_{1500}, r_{1000}, and r_{500} (Figure 11). Entropy values at these radii are
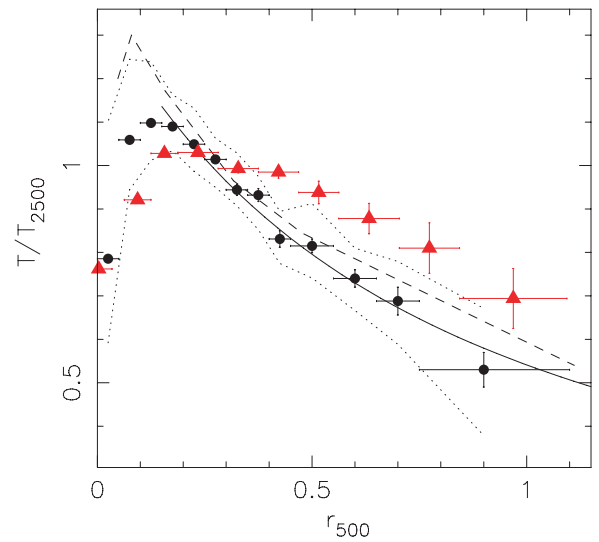

Figure 9. Mean temperature profile of groups (black circles) and the 1σ scatter in dotted lines. The solid line is the best fit from Equation (6). The dashed line is the mean temperature profile of 1–3 keV systems from Borgani et al. (2004) simulations. The data points in triangles are the mean temperature profile from LM08 on 48 $kT > 3.3$ keV clusters at $z = 0.1$–0.3. Note the mean temperature T_M defined in LM08 is computed by fitting the profile with a constant after excluding the central $0.1\ r_{180}$ region. It should be smaller than T_{2500} as T_{2500} is emission-weighted within r_{2500}. Nevertheless, it is clear that the group temperature profiles are more peaky than those of clusters around the center.

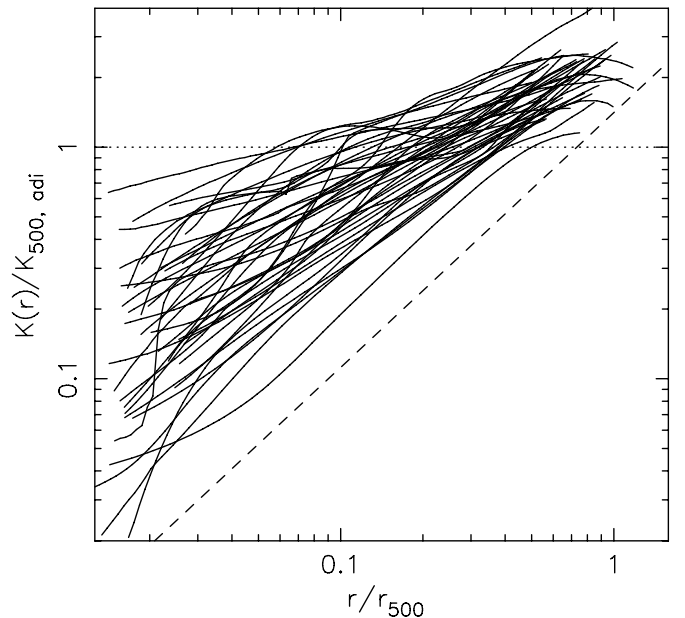(A color version of this figure is available in the online journal.)

Figure 10. Entropy profiles scaled by $K_{500,\mathrm{adi}}$ (Section 6). The dashed line represents the baseline entropy profile derived by VKB05 with a power index of 1.1. The observed entropy profiles all lie above the baseline.

K_{30kpc}, $K_{0.15r500}$, K_{2500}, K_{1500}, K_{1000}, K_{500}, respectively (note the difference between K_{500} and $K_{500,\mathrm{adi}}$ defined earlier). We chose 30 kpc to represent the entropy level around the BCG. Previous studies often discussed entropy at $0.1\ r_{200}$ (e.g., Ponman et al. 2003), which is about $0.15\ r_{500}$. We also performed the Bivariate Correlated Errors and Intrinsic Scatter (BCES) (Y|X) regression (Akritas & Bershady 1996) to these relations, and the results are listed in Table 5. The entropy values at 30 kpc
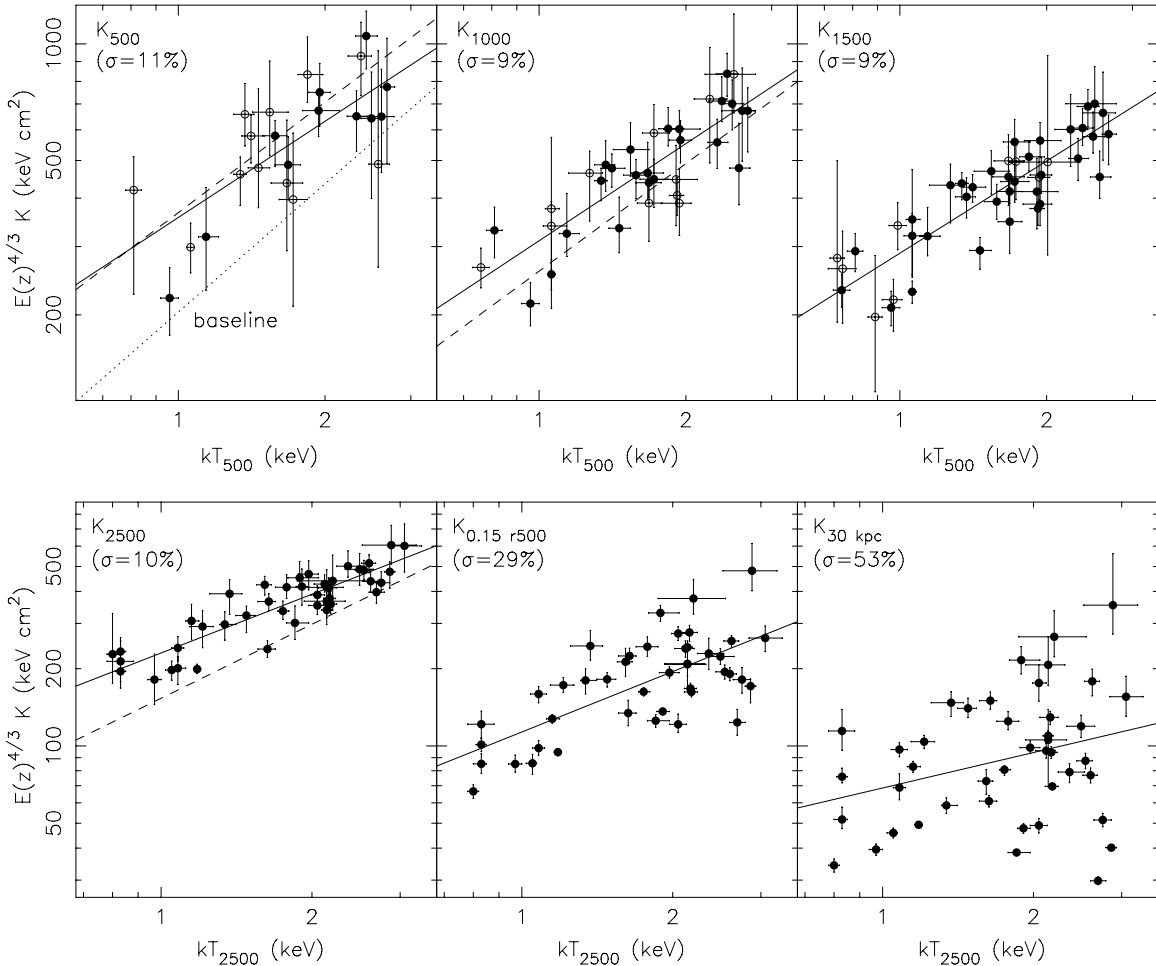
Figure 11. Entropy values at r_{500}, r_{1000}, r_{1500}, r_{2500}, 0.15 r_{500}, and 30 kpc vs. system temperature (T_{500} or T_{2500}). The open data points (in the upper three panels) are based on extrapolation of the temperature and density profiles (see Section 4 for details). The solid lines are the best fits to our data from the BCES (Y|X) estimator (Table 5), while the dashed lines are the best fits from the NKV07 simulations. The entropy excess above the NKV07 simulations (with cooling and SF) is significant at r_{2500}, while the agreement is better at larger radii. The dotted line in the K_{500} plot represents the base-line entropy by VKB05 (or 1.40 $K_{500,adi}$, Section 6). Note that the baseline has a slope of 1.1 rather than 1.0 as the $M_{500}-T_{500}$ relation used (the fourth row of Table 6) has a slope of 1.65 (rather than 1.5). It is also clear that the entropy values at 0.15 r_{500} and 30 kpc show large intrinsic scatter. The measured intrinsic scatter in the K–T relations decreases with radius and stays the same from r_{2500} to r_{500} at ∼ 10%.

radius hardly show any correlation with the system temperature. The K–T relation is stronger at 0.15 r_{500}, but the intrinsic scatter is still substantial. The large scatter of gas entropy around the center has been known for a while (e.g., Ponman et al. 2003). We also examined the connection between the luminosity of the central radio source (see Table 1) and the entropy scatter at 0.15 r_{500}. No correlation is found, before or after the temperature dependence of entropy is removed. However, in Section 7.2, we show that the entropy scatter at 0.15 r_{500} is tightly correlated with the scatter of the gas fraction within r_{2500}.

Despite large entropy scatter from the core to at least 0.15 r_{500}, the K–T relations are tighter at r_{2500} and beyond. We derived the intrinsic scatter in these relations, using the method described in Pratt et al. (2006) and Maughan (2007). As shown in Figure 11, the intrinsic scatter reduces to 10% at r_{2500} and stays at that level to r_{500}. As the derived intrinsic scatter decreases with increasing measurement errors, could this trend be due to the increasing measurement errors with radius? To answer this question, we compared $K_{2500}-T_{2500}$ and $K_{0.15r500}-T_{2500}$ relations. If we use the relative measurement errors of $K_{0.15r500}$ for the corresponding K_{2500}, the intrinsic scatter only increases to 12%. Similarly, if we use the relative measurement errors of K_{2500} for the corresponding $K_{0.15r500}$, the intrinsic scatter only

decreases to 28%. Therefore, the significant tightening of the K–T relation from 0.15 r_{500} to r_{2500} is not caused by different measurement errors. Similarly, we find that the intrinsic scatter in entropy at radii from r_{2500} to r_{1000} is affected little by switching measurement errors. The K_{500} values have large measurement errors and half of systems are extrapolated from r_{1000}. Clearly more groups with K_{500} robustly determined are required, but the intrinsic scatter in the current $K_{500}-T_{500}$ relation is consistent with the level from r_{2500} to r_{1000}. Thus, groups behave more regularly from r_{2500} outward than inside 0.15 r_{500}.

We also include 14 clusters from V06 and V09 for comparison and to constrain the K–T relations in a wider temperature range (Figure 12 and Table 5). The measured slopes increase from ∼ 0.50 at 0.15 r_{500} to ∼ 1 at r_{500}, mainly caused by the excess entropy of groups at their centers. The slope we find at 0.15 r_{500}, 0.494 ± 0.047, is consistent with what Pratt et al. (2006) found at 0.1 r_{200} for 10 groups and clusters with the XMM-*Newton* data, 0.49 ± 0.15, but smaller than what Ponman et al. (2003) found at 0.1 r_{200} with *ROSAT* and *ASCA* data, ∼ 0.65. We, however, caution that the V09 cluster sample lacks noncool core clusters. Pratt et al. (2006) also gave the K–T relation at 0.3 r_{200}, which is about r_{2500}. The slope they found, 0.64 ± 0.11, is also consistent with our result, 0.740 ± 0.027. At r_{500},
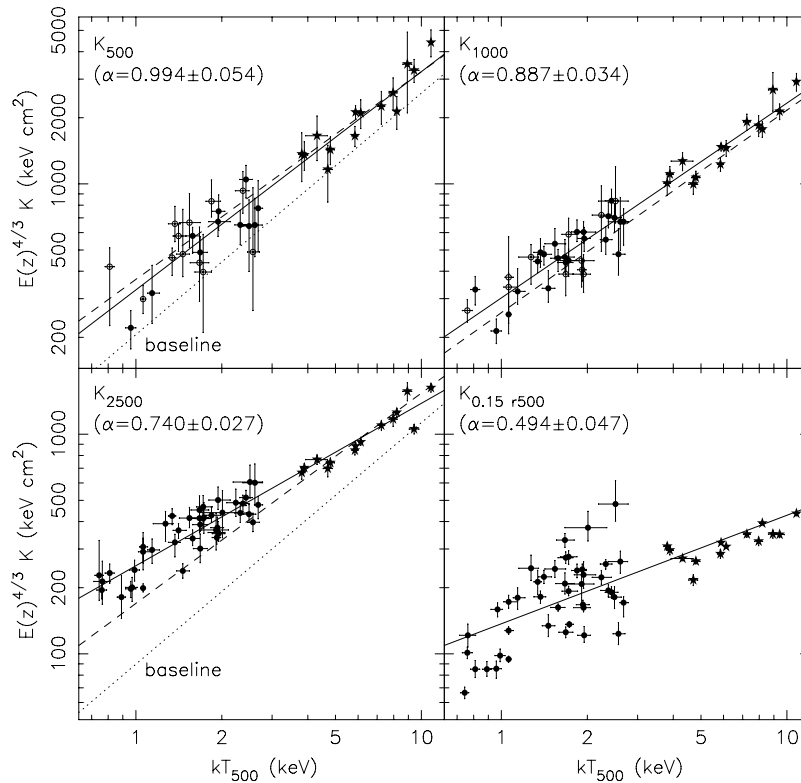
Figure 12. K–T_{500} relations at r_{500}, r_{1000}, r_{2500}, and 0.15 r_{500} for groups in our sample and 14 clusters from V09. The solid lines are the best fits of the data from the BCES (Y|X) estimator (Table 5), while the dashed lines are the best fits from the NKV07 simulations. The dotted lines in the K_{500} and K_{2500} plots represent the base-line entropy by VKB05. The best-fit slopes from observations are also shown. The agreement between observations and the NKV07 simulations becomes better with increasing radius. At r_{2500}, the observed entropy values are on average 56%–22% higher than those from the NKV07 simulations at 0.8–2.5 keV. At r_{1000}, the difference is 18%–8% from 0.8–10 keV. At r_{500}, the NKV07 line is basically the same as our best fit, which also has a slope expected from the self-similar relation (1.0). The $K_{0.15\,r500}$–T_{500} relation has significant scatter. Almost all clusters in the V09 sample have dense cool cores. Inclusion of noncool-core clusters may steepen the K–T relation at 0.15 r_{500}.

the slope we found is consistent with the expected value from the self-similar relation (1.0). Interestingly, the derived K_{500}–T_{500} relation agrees very well with the NKV07 simulations with cooling + star-formation (Figure 12), although the agreement is progressively worse with decreasing radius. The tightening of the K–T relation at r_{2500} and beyond was also reported in the NKV07 simulations, but the predicted K_{2500}–T relation by NKV07 lies below all groups in our sample (Figures 11 and 12). The NKV07 simulations with cooling + star-formation achieve entropy amplification with strong condensation to drop dense materials out of the X-ray phase. The resulting stellar fraction is about twice the observed value as too much material has cooled. If the star formation is suppressed with more efficient feedback, entropy is lower in the NKV07 simulations, between the results from the simulations with cooling + star-formation and the nonradiative simulations, which further disagrees with observations. It seems that the most challenging task is to explain the excess entropy of groups at r_{2500}. As shown in Borgani & Viel (2009), simply increasing entropy floor from preheating produces too large voids in the Lymanα forest. Thus, it is still an open question on how to generate enough entropy in groups from the center to r_{500} and still preserve other relations like the condensed baryon fraction and properties of the Lymanα forest.

6.2. Entropy Ratios

We derived the ratios of the observed entropy to the baseline entropy from VKB05 at r_{500}, r_{1000}, and r_{2500} (Figure 13). For

comparison, we also include the entropy ratios for 14 clusters from V06 and V09. The entropy ratios are always larger than or comparable to unity at all radii. The average ratio decreases with radius, for both groups and clusters, although the decrease is more rapid in groups. For groups, the weighted mean decreases from 2.2 at r_{2500} to 1.57–1.60 at r_{500}, while the mean decreases only $\sim 9\%$ for clusters. Thus, there is still a significant entropy excess over the VKB05 entropy baseline at r_{500}, in both groups and clusters. The weighted mean entropy of groups at r_{500} is $\sim 18\%$ larger than that of clusters. If we consider only the $T_{500} \lesssim 1.4$ keV groups, the weighted mean for seven groups is 1.68. Similar studies have been done with *ASCA* and *ROSAT* data (Finoguenov et al. 2002; Ponman et al. 2003). When the observed entropy values at r_{500} are scaled with $M_{500}^{-2/3}$ (which is proportional to $K_{500,\mathrm{adi}}^{-1}$), both works found that groups have on average twice the scaled entropy of clusters. Ponman et al. (2003) further concluded that the excess entropy is observed in the full mass range. Thus, the results from this work, V06 and V09 confirm the previous finding of the excess entropy at r_{500} over the full mass range, but the magnitude of the excess is smaller, and the difference between groups and clusters is also smaller than previous results, $\sim 15\%$–20% versus $\sim 100\%$ in Finoguenov et al. (2002) and Ponman et al. (2003).

As pointed out by Pratt et al. (2006), the magnitude of the excess may be affected by the systematics of the M–T relation, or how robust the hydrostatic equilibrium (HSE) mass is. The NKV07 simulations show that the HSE mass is systematically lower than the real mass, and the difference is biggest in low-mass systems. The real mass is 45% higher than the HSE mass
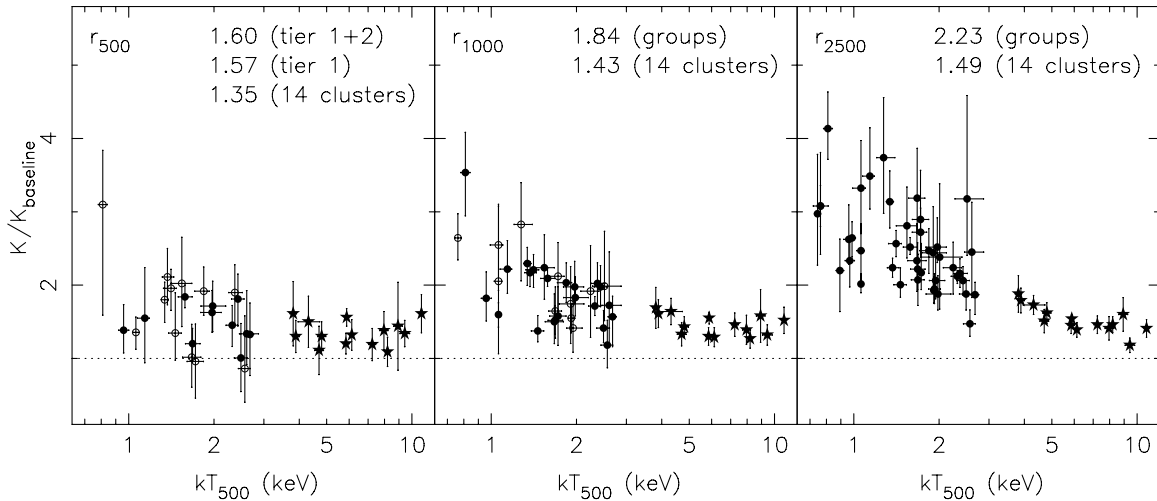
Figure 13. Ratios of the observed entropy values to the entropy baseline from VKB05 at r_{500}, r_{1000}, and r_{2500}. Fourteen clusters from V06 and V09 are included for comparison. The open data points are from extrapolation. We also show weighted means at each radius for the group and cluster samples. The observed entropy values are always larger than or comparable to the baseline at all radii, but the average ratios decrease with radius for both clusters and groups. The decrease is more dramatic in groups.

for 1 keV groups, while the difference reduces to 13% for 10 keV clusters. The best-fit M_{500}–T_{500} relation from this work and V06 (Section 7.1) is close to the relation for the HSE mass in NKV07. Thus, if this bias is real, the actual entropy ratios at r_{500} are smaller. For 1 keV groups, a 45% higher total mass means a 13% larger r_{500}. For a typical entropy slope of 0.7 in this sample (Section 6.3), the entropy ratio at r_{500} is reduced by 17%. Similarly for 5 keV clusters, the entropy ratio at r_{500} is reduced by 8% for an average entropy slope of 0.9 at large radii. Thus, this bias can explain only part of the entropy excess observed. The entropy baseline, we adopted in this work, is from the smoothed particle hydrodynamics simulations, while the Adaptive Mesh Refinement (AMR) simulations produce a baseline with 7% higher normalization (VKB05), likely because of its better capability to catch shocks. However, the entropy excess for groups at r_{500} remains significant.

There are several mechanisms to achieve entropy amplification at r_{500}. The first idea relies on modification of accretion, without extra nongravitational processes (Ponman et al. 2003; Voit et al. 2003; Voit & Ponman 2003). If preheating or feedback in small subhalos that are being accreted can eject gas out of the halo and thicken the filaments significantly, the accretion may be smoother than the lumpy accretion in hierarchical mergers. Voit (2005) showed that the smooth accretion can generate ∼ 50% more entropy throughout the cluster than would lumpy hierarchical accretion. However, Borgani et al. (2005) argued that this entropy amplification effect is substantially reduced by cooling. The other ideas resort to nongravitational processes. As discussed in the last section, although the NKV07 simulations predict the K_{500}–T_{500} relation very well, they produce too many stars. Thus, models with only cooling may not be enough. Borgani et al. (2005) showed that galactic winds from SN explosions are rather localized and cannot boost entropy enough at large radii. Thus, a feedback mechanism that can distribute heat in a very diffuse way is required. As groups are smaller than hot clusters, AGN outflows from the central galaxy can reach a larger scaled radius. One good example in this sample is 3C449 (Section 8 and the Appendix), with radio lobes extending to at least 3.7 r_{500}. Thus, it is still an open question to explain the entropy excess at r_{500}, especially in groups. But the much reduced entropy ratios from this work largely alleviate the problem. It is

also clear that more systems with the entropy ratio constrained at r_{500} are required for better comparison, especially $T_{500} \lesssim$ 1.4 keV groups.

6.3. Entropy Slopes

We also derived the entropy slopes at 30 kpc–$0.15 r_{500}$, 0.15 r_{500}–r_{2500}, r_{2500}–r_{1500} (or $r_{\mathrm{det,spe}}$) and r_{1500}–$r_{\mathrm{det,spe}}$ (Figure 14). The scatter is large but the average slopes are about the same (∼ 0.7) beyond 0.15 r_{500}. The slope is always shallower than that from pure gravitational processes (∼ 1.1). Mahdavi et al. (2005) analyzed the XMM-*Newton* data of eight nearby groups and found their entropy profiles are best fitted by a broken power law with the break radius of ∼ $0.1 r_{500}$. Across the break radius, the entropy slope decreases from 0.92 to 0.42. As the break radius is very near the core, this kind of entropy profiles may be caused by a cool core within 0.1 r_{500}. From 0.15 r_{500}, there are systems in our sample with an entropy slope of around 0.42, but the weighted mean is significantly larger. The measured average slopes in this work are consistent with the result by Finoguenov et al. (2007; 0.6–0.7) for groups.

7. MASS AND GAS FRACTION

7.1. M–T and M–Y_X Relations

One of the most important aspects of cluster science is to use clusters to study cosmology, which often involves derivation of a cluster mass function. Assuming hydrostatic equilibrium, X-ray observations can be used to derive the cluster mass (at least the HSE value), provided the radial coverage of the data is good. Often we estimate cluster mass from another X-ray observable used as a mass proxy. A frequently used mass proxy is gas temperature, so it is important to understand the cluster M–T relation. There had been a lot of work on the cluster M–T relation before the *Chandra* and XMM-*Newton* era (e.g., Finoguenov et al. 2001; Sanderson et al. 2003). However, as emphasized in V06, it is crucial to constrain the gas properties (both the temperature gradient and the density gradient) at large radii (e.g., around r_{500}). Systematics like the assumption of a polytropic equation of state and the inadequate fit of the density profile at large radii can bias the HSE mass to lower values (Borgani et al. 2004; V06). The M–T relations have also been constrained with
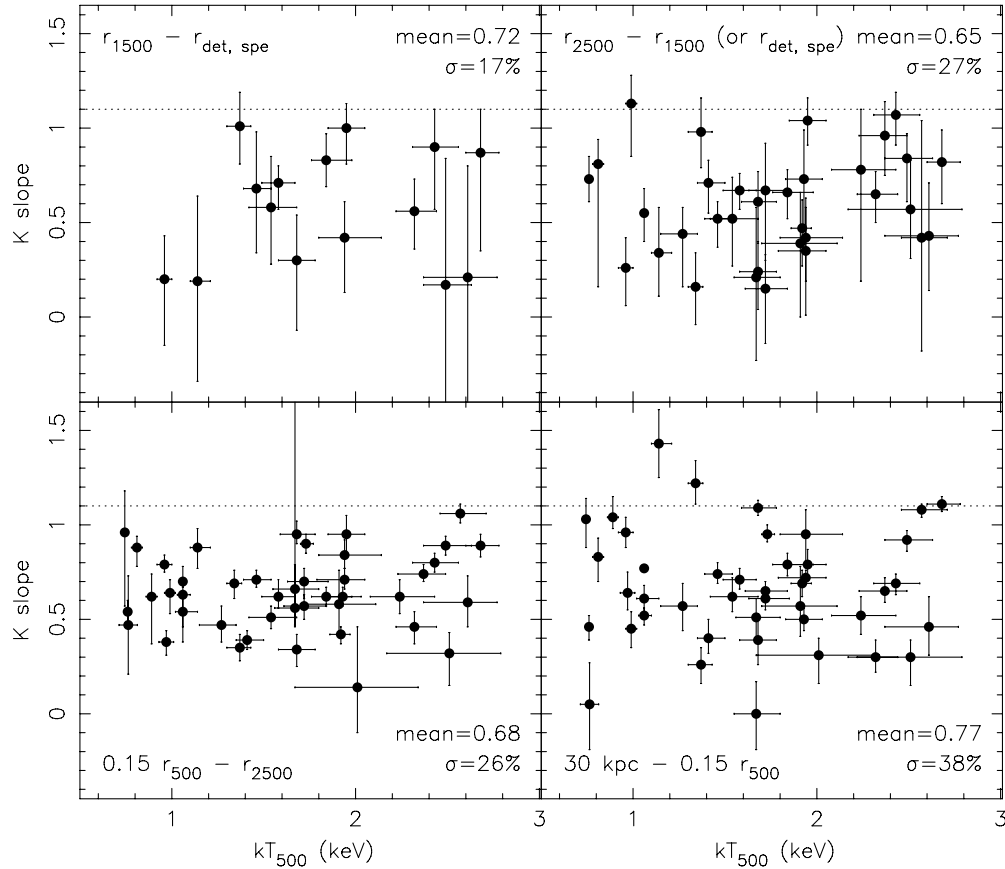
Figure 14. Entropy slopes between $r_{1500}-r_{\rm det,spe}$, $r_{2500}-r_{1500}$ (or $r_{\rm det,spe}$), $0.15\ r_{500}-r_{2500}$, and 30 kpc–$0.15\ r_{500}$ vs. T_{500}. Beyond $0.15\ r_{500}$, the slopes are always shallower than 1.1 and the weighted averages are all around 0.7.
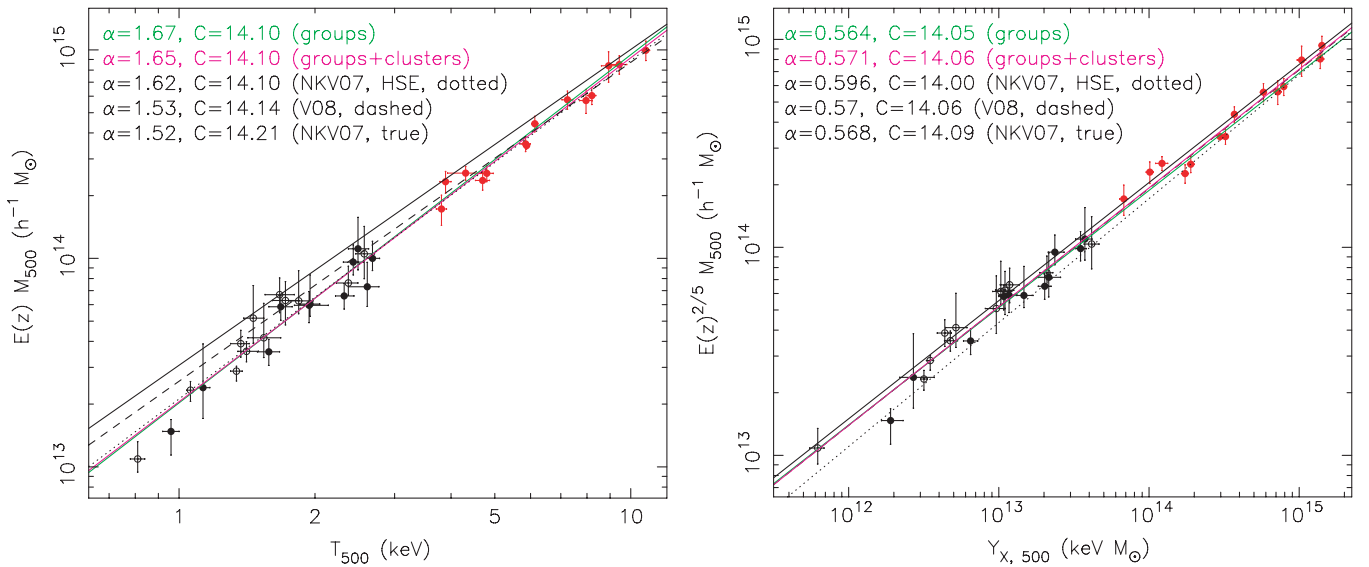

Figure 15. $M_{500}-T_{500}$ (left panel) and $M_{500}-Y_{\rm X,500}$ (right panel) relations, combining the results from this work (circles) and V09 (filled stars). The open circles are tier 2 groups. The dashed lines are the relations for the real mass in the NKV07 simulations, while the dotted lines are the relations for the mass derived under the assumption of hydrostatic equilibrium in the NKV07 simulations. The dashed-dotted-dotted-dotted lines are the best-fit relations from V09. The $M_{500}-T_{500}$ relation can be well described by a power law down to at least M_{500} of $2\times10^{13}\ h^{-1}\ M_\odot$, although the HSE mass may be systematically lower than the real mass. The $M_{500}-Y_{\rm X,500}$ relation has a smaller scatter and the agreement with the NKV07 simulations is much better. Note as $Y_{\rm X,500}\propto h^{-2.5}$, the h-dependence of M_{500} should be $h^{1/2}$ for the self-similar relation, $M_{500}\propto Y_{\rm X,500}^{3/5}$. We still use the h^{-1} dependence to directly compare with the left panel.

(A color version of this figure is available in the online journal.)

Chandra and XMM-*Newton* (Arnaud et al. 2005 with the XMM-*Newton* data; V06 and V09 with the *Chandra* data). However, the number of clusters used to constrain the M–T relation is still small (10 in Arnaud et al. 2005 and 17 in V09). There are only four systems with temperatures of 2.1–3.0 keV in Arnaud et al. (2005) and only three systems with temperatures of 1.6–3.0 keV

Table 6
M_{500}–T_{500} Relation[a]

Sample	M_3 ($10^{14}h^{-1}M_\odot$)	α	r_3 (h^{-1} Mpc)
Tier 1	1.17 ± 0.21	1.64 ± 0.21	0.587 ± 0.035
Tier 1 + clusters	1.21 ± 0.08	1.68 ± 0.04	0.593 ± 0.014
Tier 1+2	1.27 ± 0.12	1.67 ± 0.15	0.602 ± 0.020
Tier 1+2 + clusters	1.26 ± 0.07	1.65 ± 0.04	0.600 ± 0.011
Tier 1+2 (> 1 keV) + clusters	1.27 ± 0.06	1.60 ± 0.03	0.602 ± 0.010

Notes.
[a] $E(z)M_{500} = M_3 (T_{500} / 3 \text{ keV})^\alpha$, where T_{500} is spectroscopic temperature. r_3 is the corresponding scale in the r_{500}–T_{500} relation ($E(z)r_{500} = r_3 (T_{500}/3 \text{ keV})^{\alpha/3}$). The cluster sample includes 14 $T_{500} > 3.7$ keV systems from V09. We used the BCES orthogonal regression (Akritas & Bershady 1996).

Figure 16. Density gradient at r_{500} in terms of β_{eff} (see the appendix of V06) for tiers 1 and 2 groups that M_{500} is derived. Most groups have β_{eff} of 0.55–0.75.

in V09 (two overlapping with the Arnaud et al. sample). Our paper adds more < 2.7 keV systems (23 tier 1/2 groups).

The total mass values and uncertainties at interesting radii are derived from the 1000 simulated density and temperature profiles. The determination of the best-fit value and the 1σ errors (at two sides) is mentioned in Section 4. One difference from the determination of entropy is that we include only simulations that produce physically meaningful mass density profiles (mass density always larger than zero). The derived M_{500}–T_{500} relation with the tiers 1+2 groups is shown in Figure 15. The BCES fits are listed in Table 6. We also included 14 clusters from V09 to constrain the M–T relation in a wider mass range. Our results show that the M_{500}–T_{500} relation can be described by a single power law down to at least $M_{500} = 2 \times 10^{13}$ h^{-1} $M_\odot$. At $T_{500} < 1$ keV, more systems are needed to examine whether the relation steepens or not. Our M_{500}–T_{500} relation is steeper than but still consistent with V09's (1.65 ± 0.04 versus 1.53 ± 0.08). Our slope is consistent with the Borgani et al. (2004) simulations with nongravitational processes included (1.59 ± 0.05), especially if two groups at $T_{500} < 1$ keV are excluded. The derived M_{500}–T_{500} relation can also be compared with that by Arnaud et al. (2005), which has a slope of 1.71 ± 0.09. Arnaud et al. (2005) defined the system temperature as the overall spectroscopic temperature of the 0.1 r_{200}–0.5r_{200} region, which should be close to T_{1000} defined in this work (note $r_{500} \sim 0.66r_{200}$). The data of the tiers 1 and 2 groups give $T_{500}/T_{1000} = 0.96$ on average. Then we find that the *Chandra* M_{500}–T relation constrained from 23 groups + 14 V09 clusters is 3%–18% higher than that by Arnaud et al. (2005) at 1–10 keV. We also note that at 1 keV, the normalization of the *Chandra* M_{500}–T_{500} relation is 54% higher than that by Finoguenov et al. (2001). This is expected from the generally higher density gradient around r_{500} derived in this work (Figure 16) than the typical values in Finoguenov et al. (2001; also see the Appendix of V06).

As shown in Figure 15, our M_{500}–T_{500} relation is offset from the true M_{500}–T_{500} relation in the NKV07 simulations, from 33% lower at 1 keV to 9% lower at 10 keV. The agreement with the Borgani et al. (2004) simulations is better, from 18% lower at 1 keV to 6% lower at 10 keV. Interestingly, the $M_{500,\text{HSE}}$–T_{500} relation from the NKV07 simulations is almost the same as the *Chandra* M_{500}–T_{500} relation from 23 groups + 14 V09 clusters. NKV07 attribute turbulence as the extra pressure to deviate the HSE mass from the true mass (also see Rasia et al. 2004; Kay et al. 2004). Indeed for the ICM without a magnetic field, the dynamic viscosity is roughly proportional to $T_{\text{ICM}}^{2.5}$. Thus, it may not be surprising that cool groups can develop stronger turbulence. However, the ICM is magnetized and the real magnitude of the ICM
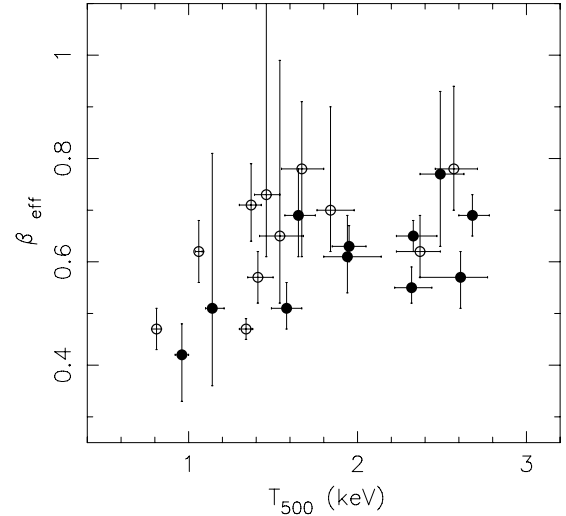
turbulence is unknown. The NKV07 simulations only have numerical viscosity that is small. Simulations with viscosity at different strengths are required to better determine this bias term. High resolution X-ray spectra of the ICM may be ultimately required to constrain the turbulence pressure in the ICM.

Kravtsov et al. (2006) suggested a new mass proxy, the Y_X parameter (product of the gas temperature and the gas mass derived from the X-ray image, or $M_{\text{gas},500}T_{500}$ in this work), which in simulated clusters has a remarkably low scatter of only 5%–7%, regardless of whether the clusters are relaxed or not. The agreement between simulations and observations is also better for the M–Y_X relation than the M–T relation (NKV07). We examined the M_{500}–$Y_{X,500}$ relation for 23 groups + 14 V09 clusters (Figure 15 and Table 7). Our results indicate that a single power law relation can fit the data very well. Our best fit (0.57 ± 0.01) is the same as the V09 best fit at $Y_X > 2 \times 10^{13} M_\odot$ keV (0.57 ± 0.05), implying the groups aligned well with clusters. Our best fit is also consistent with the XMM-*Newton* result by Arnaud et al. (2007) (10 clusters at $Y_X > 10^{13} M_\odot$ keV), on both the slope (0.548 ± 0.027) and the normalization (within $\sim$ 3%). Maughan (2007) assembled 12 clusters at $z = 0.14$–0.6 from their work and literature ($Y_X > 8 \times 10^{13} M_\odot$ keV) and found that the slope of the M_{500}–$Y_{X,500}$ relation is consistent with the fit to the V06 clusters (0.564 ± 0.009). Intrinsic scatter in both the M–T and M–Y_X relations is consistent with zero as the measurement errors for groups are large. If we simply move the best-fit lines up or down to estimate the range of the scatter from the best-fit mass values, the scatter in the M–Y_X relation is about the half that in the M–T relation. The slope is very close to the self-similar value of 0.6, especially if only tier 1 groups are included (0.588 ± 0.012). Our best fits lie between the true mass and the HSE mass from the NKV07 simulations, but the offset is much smaller than that in the M_{500}–T_{500} relation. Thus, the Y_X parameter appears to be a robust mass proxy down to at least 2×10^{13} h^{-1} $M_\odot$. With the derived M–T and M–Y_X relations in this work, the slope of the $M_{\text{gas},500}$–T_{500} relation is 1.89 ± 0.05 (for tier 1+2 groups + V09 clusters), or 1.86 ± 0.06 (for tier 1 groups + V09 clusters). This value of the slope is consistent with the result by Mohr et al. (1999), 1.98 ± 0.18 (90% confidence).
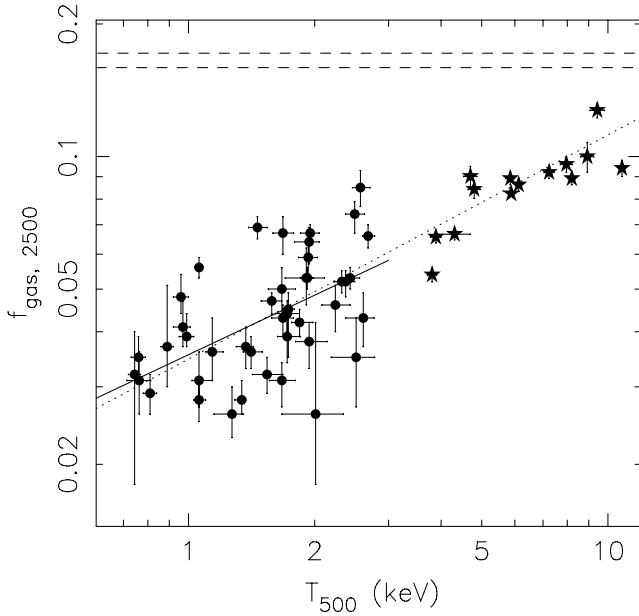
Figure 17. Enclosed gas fraction within r_{2500} vs. T_{500} (groups + 14 clusters from V06 and V09). The solid line is the BCES fit to the group sample ($0.0355 \pm 0.0018 (T_{500}/1 \text{ keV})^{0.449\pm0.096}$), while the dotted line is the BCES fit to the group + cluster sample ($0.0347 \pm 0.0016 (T_{500}/1 \text{ keV})^{0.509\pm0.034}$). The intrinsic scatter on the $f_{\text{gas},2500}$–T_{500} relation is 22%. Two dashed lines enclose the 1σ region of the universal baryon fraction derived from the *WMAP* Five year data combined with the data of the Type Ia supernovae and the Baryon Acoustic Oscillations (0.1669 ± 0.0063, Komatsu et al. 2009).

7.2. Gas Fraction

We derived the enclosed gas fraction profile for each group. The enclosed gas fraction generally increases with radius, and this trend continues to the outermost radius in our analysis, as generally found in V06. The enclosed gas fractions for groups at r_{2500} have a large scatter (Figure 17). For groups with similar T_{500}, $f_{\text{gas},2500}$ can be different by a factor as large as 2.5. Both the weighted average and the median of $f_{\text{gas},2500}$ in our sample is 0.043, much smaller than the typical value of ~ 0.09 for V09 clusters. This mean can be compared with the average $f_{\text{gas},2500}$ by G07 (0.050 ± 0.011), and we note that the 16 groups in G07 are on average brighter than our systems in a similar redshift range. The intrinsic scatter of $f_{\text{gas},2500}$ is tightly correlated with the intrinsic scatter of $K_{0.15r500}$, after the temperature dependence of both variables are removed from their relations with temperature (Figure 18). Groups with low $f_{\text{gas},2500}$ have high $K_{0.15r500}$ relative to the average relations. Thus, the large scatter of the gas fraction within r_{2500} for groups is tightly correlated with the large scatter of entropy at 0.15 r_{500}, and likely also the large scatter of X-ray luminosities for groups. Group properties (e.g., luminosity and central entropy) have large scatter because of the large scatter of the gas fraction around the center (e.g., r_{2500}). Groups are on average fainter than what is expected from the self-similar L–T relation, because groups are generally "gas-poor" within r_{2500}, compared with clusters.

The enclosed gas fraction within r_{500} is also derived for tiers 1 + 2 groups (Figure 19). We added 14 clusters from V06 and V09 to constrain the f_{gas}–T_{500} relations. The $f_{\text{gas},500}$–T_{500} relation has a slope of ~ 0.16–0.22, depending on whether both tiers 1 and 2 are included (Figure 19). We also give the $f_{\text{gas},500}$–M_{500} relation from the BCES orthogonal fit. For tiers 1 + 2

groups + clusters:

$$f_{\text{gas},500} = (0.0616 \pm 0.0060)\, h_{73}^{-1.5} \left(\frac{M_{500}}{10^{13}\, h_{73}^{-1}\, M_\odot} \right)^{0.135\pm0.030}. \tag{8}$$

For tier 1 groups + clusters

$$f_{\text{gas},500} = (0.0724 \pm 0.0078)h_{73}^{-1.5} \left(\frac{M_{500}}{10^{13}\, h_{73}^{-1}\, M_\odot} \right)^{0.093\pm0.031}. \tag{9}$$

We note that the NKV07 simulations predict $f_{\text{gas},500} \propto T_{500}^{0.152}$ (or $M_{500}^{0.10}$), from their best-fit M_{500}–T_{500} and M_{500}–$Y_{\text{X},500}$ relations. The gas fraction predicted in simulations depends on the modeling of cooling (e.g., Kravtsov et al. 2005) and is often tangled with the problem of predicting the right stellar mass fraction in clusters. We also derived the enclosed gas fraction between r_{2500} and r_{500} for 23 groups in tiers 1 and 2 (Figure 19). Combined with the V06 and V09 results for clusters, the average f_{gas}–T_{500} has little or no temperature dependence with an average value of ~ 0.12, although the measurement errors are not small. $f_{\text{gas},2500-500}$ can also be derived as

$$f_{\text{gas},2500-500} = f_{\text{gas},500} \left(\frac{1 - a \frac{f_{\text{gas},2500}}{f_{\text{gas},500}}}{1 - a} \right) \tag{10}$$

$$(a = M_{2500}/M_{500} = 5(r_{2500}/r_{500})^3).$$

We use $f_{\text{gas},2500} = 0.0347 T_{500}^{0.509}$ (from the BCES fit to 43 groups and 14 clusters, Figure 17) and $f_{\text{gas},500} = 0.0708 T_{500}^{0.220}$ (from the BCES fit to 23 groups and 14 clusters, Figure 19). Combining our results on c_{500} (Section 7.3) with V06's for clusters, roughly we have $c_{500} = 5.0(M_{500}/10^{13} M_\odot)^{-0.09}$. Assuming an NFW profile, the r_{2500}/r_{500} ratio can be well approximated as $r_{2500}/r_{500} \approx 0.322 + 0.178\, lg(1.523 c_{500})$ at $c_{500} = 1.3$–5.0. Thus, combined with the M_{500}–T_{500} relation derived in this work, we can estimate the $f_{\text{gas},2500-500}$–T_{500} relation. Indeed as shown in Figure 19, $f_{\text{gas},2500-500}$ is nearly constant at 1–10 keV. The average $f_{\text{gas},2500-500}$ is still $\sim 27\%$ lower than the universal baryon fraction (0.1669 ± 0.0063 from Komatsu et al. 2009). However, one should be aware that the enclosed gas fraction still rises beyond r_{500}, as generally found in V06 and this work. We also note that the observed $f_{\text{gas},2500-500}$ is consistent with what was found in the simulations of Kravtsov et al. (2005) with cooling and star formation. We conclude that the low gas fraction generally observed in groups is mainly due to the low gas fraction of groups within r_{2500}, or the generally weak ability of the group gas to stay within r_{2500}. Beyond r_{2500}, the groups are more regular and more similar to hot clusters, as also shown by the smaller scatter of their entropy values at $r \gtrsim r_{2500}$.

A natural question motivated by these results on entropy and gas fraction is: what is the fraction of the group luminosities within 0.15 r_{500} or r_{2500}? Detailed work on the group L_X–T relation is beyond the scope of this paper and will be presented in a subsequent paper with an extended sample (including nonrelaxed groups). Here we give the curves of the enclosed count fluxes for 17 groups that r_{500} is reached by *Chandra* or (and) PSPC (Figure 20). As the previous L_X–T relations only used the global spectrum to convert the count rate to the group flux, Figure 20 can be regarded as the growth curves of the enclosed group luminosities. At 0.15 r_{500}, the fraction
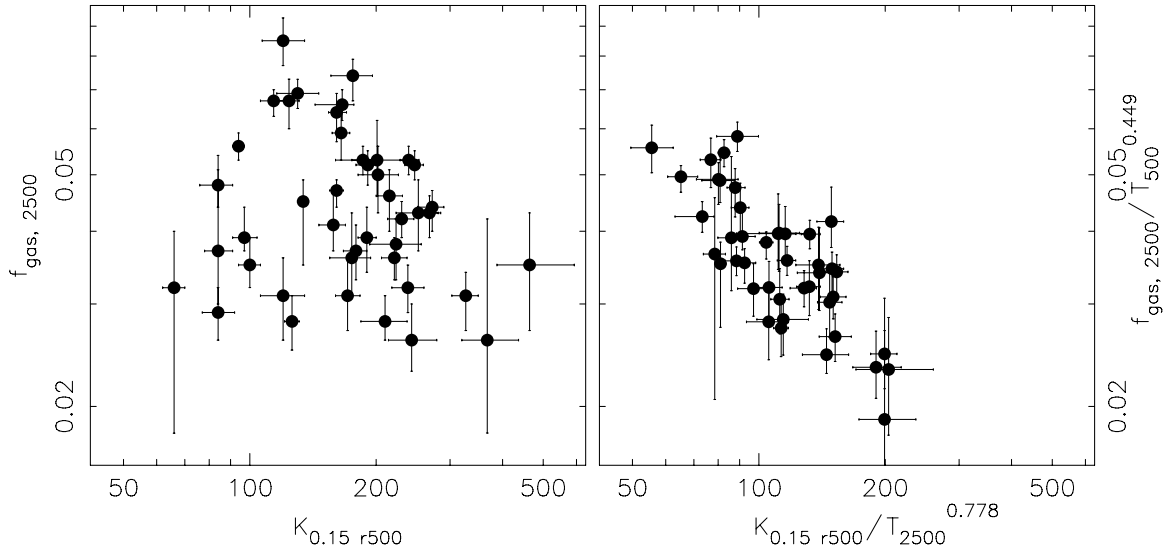
Figure 18. Enclosed gas fraction within r_{2500} is correlated with the entropy at $0.15\,r_{500}$, after the temperature dependence on both variables are removed (right panel). The slope is about -0.7. The intrinsic scatter on the scaled $f_{gas,2500}$ and the scaled $K_{0.15r500}$ is 11% and 14% respectively, compared with 22% and 29% intrinsic scatter in their relations to temperature. This is primarily driven by density–density correlation, but quantitatively shows their connection.
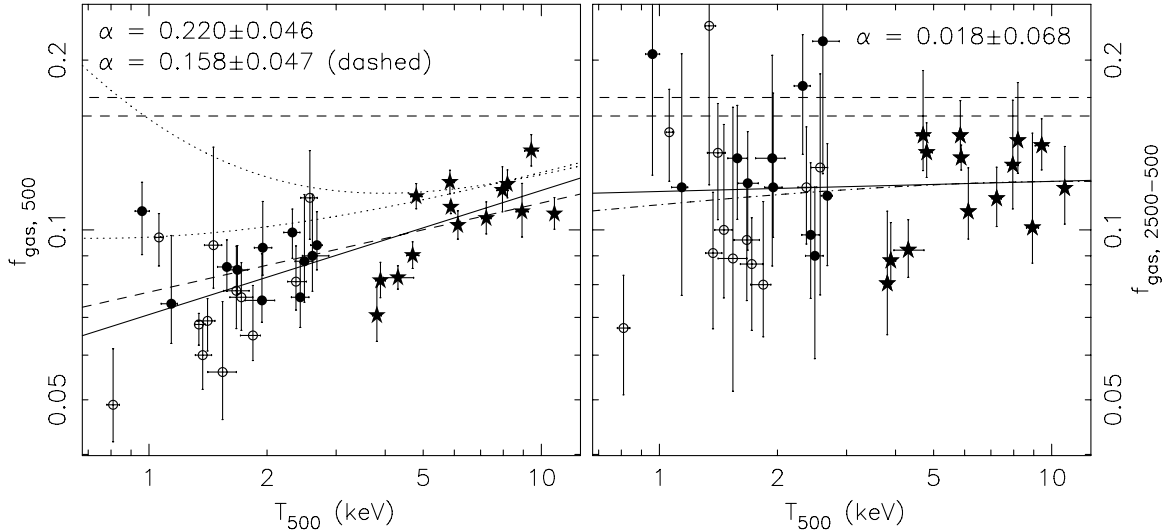

Figure 19. Enclosed gas fraction within r_{500} (left panel) and between $r_{2500}-r_{500}$ (right panel) vs. T_{500}. The open data points are tier 2 groups. The solid lines are fits to all 23 groups and 14 V09 clusters, $0.0708 \pm 0.0046\,(T_{500}/1\,\mathrm{keV})^{0.220\pm0.046}$, while the dashed line in the left panel is the fit excluding 12 tier 2 groups, $0.0776 \pm 0.0057\,(T_{500}/1\,\mathrm{keV})^{0.158\pm0.047}$. The listed power law index can be compared with that in NKV07 simulations (0.152). Two horizontal dashed lines enclose the 1σ region of the universal baryon fraction (see the caption of Figure 17). We also estimate the total baryon fraction within r_{500} by adding the $f_{gas,500}-T_{500}$ relation from 23 groups and 14 V09 clusters and the relation for stellar fraction from Lin et al. (2003) and Gonzalez et al. (2007), as shown by the two dotted lines. The upper one uses the Gonzalez et al. relation, while the lower one uses the Lin et al. relation (see Section 7.4, note that the Gonzalez et al. relation includes the intracluster light). It appears that gas fraction between $r_{2500}-r_{500}$ has no temperature dependence ($f_{gas} \sim 0.12$) on average, although there is still scatter. The solid line is the fit to all 23 groups and 14 clusters with a slope of 0.018 ± 0.068. The dashed-dotted line is the expected average $f_{gas,2500-500}$ expected from the best-fit $f_{gas,500}-T_{500}$ and $f_{gas,2500}-T_{500}$ scaling relations in this work (see Section 7.2).

ranges from 13% to 69%. At r_{2500}, the fraction ranges from 51% to 94%. Two extreme cases defining the boundaries are A1238 and AS1101, also two systems with similar T_{500} but very different $f_{gas,2500}$ (Table 3). A system with a bright cool core (like AS1101) has a large fraction of the X-ray luminosity within $0.15\,r_{500}$. Its system temperature without excluding the central core (e.g., $0.15\,r_{500}$), therefore, is biased to a lower value. A system without a bright cool core (like A1238) has a small fraction of the X-ray luminosity within $0.15\,r_{500}$, and its system temperature without excluding the central core (e.g., $0.15\,r_{500}$) is usually biased to a higher value (Figures 3–5). All these factors contribute to the large scatter of the group L_X-T relation (e.g., Osmond & Ponman 2004). Thus, the group L_X-T relation can be

significantly contaminated by the large difference in the cores (e.g., within $0.15\,r_{500}$).

7.3. c_{500}

We also fitted the total mass density profile with the NFW profile and derived the concentration parameter, $c_{500} = r_{500}/r_s$, where r_s is the characteristic radius of the NFW profile. V06 used an inner radius of $0.05\,r_{500}$, since the stellar mass of the cD is dominant in the center. The V06 sample is mainly composed of clusters. The groups in our sample have r_{500} of 440–800 kpc, so the contribution of the stellar mass at $0.05\,r_{500}$ is still significant for low-temperature systems (see e.g., G07). Thus, we use a fixed inner radius of 40 kpc. The outer radius is the outermost
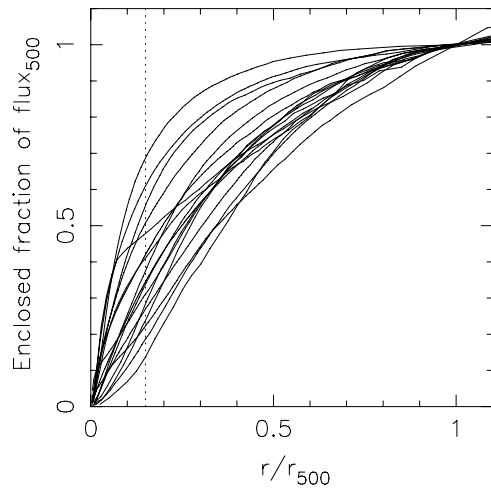
Figure 20. Enclosed fraction of the count flux for 17 groups in our sample that r_{500} is reached by *Chandra* or (and) PSPC. The dotted line marks the position of 0.15 r_{500}. There is large scatter for the enclosed fractions within 0.15 r_{500} and r_{2500} ($\sim 0.465\, r_{500}$ on average in this sample), mainly depending on the existence of a central cool core.
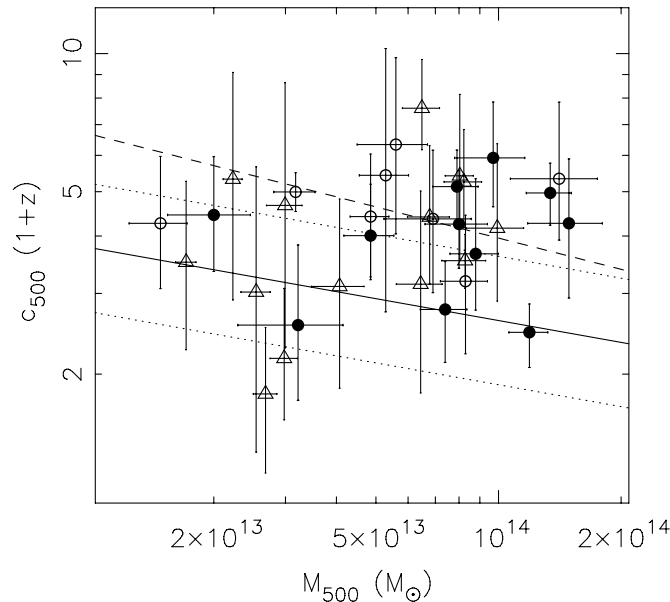

Figure 21. c_{500}–M_{500} relation from this work. The filled and open circles are for tiers 1 and 2 groups respectively. The open triangles are for tiers 3 and 4 groups with mass estimated from the M_{500}–T_{500} relation derived in this work. The solid line is the median relation from the model of Bullock et al. (2001) with parameters $F = 0.001$ and $K = 2.8$, while the two dotted lines enclose the 1σ region. We use: $\sigma_8 = 0.817$, $\Omega_M = 0.279$, $n_s = 0.96$ (tilt) from Komatsu et al. (2009). Note that σ_8 affects the predicted c_{500} significantly (see Buote et al. 2007). The dashed line is the best fit from G07. Our results show no significant mass dependence of c_{500} in this narrow mass range and are generally consistent with the prediction under the current value of σ_8. The weighted mean of c_{500} is 4.2.

radius for the spectral analysis ($r_{\rm det,spe}$ in Table 2). We derived the total mass with 1σ uncertainties at radii corresponding to the boundaries of radial bins for spectral analysis between 40 kpc and $r_{\rm det,spe}$ (Figures 3–5). The resulting mass density profile (at 4–10 radial points in this work) is fitted with an NFW profile and the uncertainty is estimated from 1000 Monte Carlo simulations. The results for 33 groups are present in Table 3 and are plotted with the system mass in Figure 21. For the other 10 groups, c_{500} is very poorly constrained. Our errors on c_{500} are larger than those in V06 and G07 as our errors on mass are larger.

We compare our results with the best-fit c–M relation from G07. G07 gave the best-fit $c_{\rm vir}$–$M_{\rm vir}$ relation. For their range of $c_{\rm vir}$, $c_{500} \sim 0.51 c_{\rm vir}$ (for $c_{\rm vir} = 10.35$). For $\Delta = 101$, we convert G07's best-fit relation to $c_{500}(1+z) = 3.96(M_{500}/10^{14}M_\odot)^{-0.226}$ (adjusted to our cosmology). As shown in Figure 21, at $M_{500} > 4.5 \times 10^{13}M_\odot$, the G07 fit describes our results very well. But our results do not show significant mass dependence, so at $M_{500} < 4.5 \times 10^{13}M_\odot$, our results are systematically below the G07 fit, although the errors are not small. However, the difference mainly comes from three groups (NGC 1550, NGC 533, and NGC 5129) for which G07 found $r_s = 41$–46 kpc (adjusted to our cosmology), and our inner radius cut at 40 kpc prevents us from measuring such a small value of r_s. In fact, the overdensity radii of these three groups agree better between G07 and this work: $r_{2500} = 206 \pm 2$ kpc (G07) versus 222 ± 6 from this work for NGC 1550, $r_{1250} = 251 \pm 2$ kpc (G07) versus 275 ± 30 for NGC 533, $r_{1250} = 217 \pm 7$ kpc (G07) versus 236 ± 13 for NGC 5129. Excluding these three groups, our results agree well with G07's. Thus, the difference mainly hinges on the determination of r_s that is related to the subtraction of stellar mass, while the results at large radii agree better. We also compare our results with the simulations of Bullock et al. (2001) and further work.[7] As c_{500} is sensitive to the halo formation time, smaller σ_8, Ω_M, and tilt drive c_{500} smaller. We used the parameters derived in Komatsu et al. (2009; see the caption of Figure 21). As shown in Figure 21, our results are generally consistent with the Bullock et al. simulations. Detailed discussions on the difference of the observed concentration parameter from the prediction can be found in Buote et al. (2007). We should point out that both our and the V06 analyses do not subtract the stellar mass and the X-ray gas mass, while G07 subtracted both components. G07 also included the XMM-*Newton* data for most of their groups. Future work on c_{500} may need very good measurement of the gas properties to $> r_{500}$ and careful modeling of the stellar and gas components (e.g., G07). The group dark matter mass profile may also need to be examined first to see whether a single NFW profile is the best fit.

7.4. The Baryon Fraction and Fossil Groups in this Sample

We can estimate the enclosed baryon fraction from the cluster stellar fraction estimated before. Lin et al. (2003) gave $M_{*,500} = 7.30 \times 10^{11}M_\odot(T_X/1{\rm keV})^{1.169}$ (adjusted to our cosmology) from the 2MASS data of nearby groups and clusters, which includes the stellar mass in cluster galaxies. With the M–T relation derived in this work from 23 groups and 14 V09 clusters, $f_{*,500,{\rm Lin}} = 0.0263(T_X/1{\rm keV})^{-0.481}$. Gonzalez et al. (2007) included the intracluster stellar mass and found $f_{*,500,{\rm Gonzalez}} = 0.0380(M_{500}/10^{14}M_\odot)^{-0.64}$ (adjusted to our cosmology). With our M_{500}–T_{500} relation, $f_{*,500,{\rm Gonzalez}} = 0.0864(T_{500}/1{\rm keV})^{-1.056}$. Adding the relation for $f_{\rm gas,500}$, the total baryon fraction from groups to clusters can be estimated. As shown in Figure 19, there is substantial difference for groups. We also examined the stellar mass of the cD and its relation with other group properties. As shown in Figure 22, the stellar mass of the group cD (which is proportional to its K_s band luminosity) is weakly correlated with the system mass. Low-mass cDs generally reside in low-mass groups. We also examined the relation between L_{Ks} of the cD and $f_{\rm gas,2500}$ but found no correlation. However, in low-mass systems with low $f_{\rm gas,2500}$, the stellar mass of the cD can be comparable to the gas mass within r_{2500}.

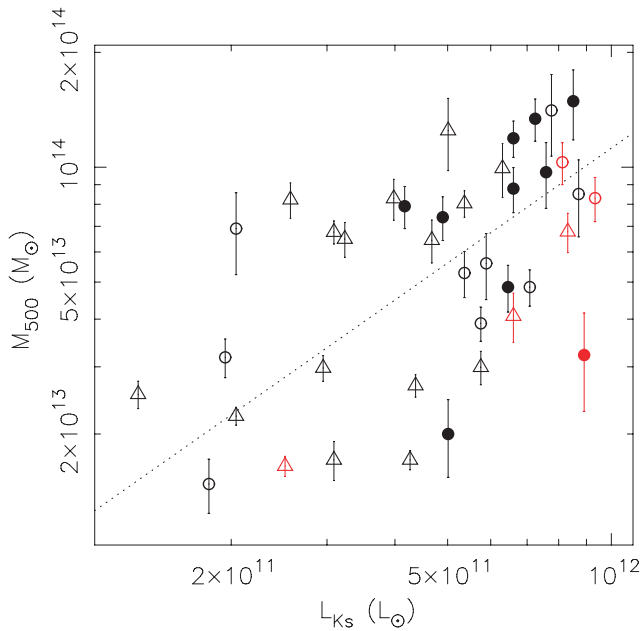[7] http://www.physics.uci.edu/~bullock/CVIR/

Figure 22. 2MASS K_s band luminosity of the cD galaxy vs. M_{500}. The filled and open circles are for tiers 1 and 2 groups respectively. The open triangles are for tiers 3 and 4 groups with mass estimated from the M_{500}–T_{500} relation derived in this work. The six data points with a horizontal bar are fossil groups identified in this work. There is a general trend that more massive groups host more massive central galaxies. The dotted line represents a constant $M_{500}/L_{Ks,cD}$ line. For the same system mass, the fossil groups host more luminous (or more massive) cDs than nonfossil groups.

(A color version of this figure is available in the online journal.)

We also searched for fossil groups in this sample. From Jones et al. (2003), fossil groups are defined as a bound system of galaxies with the R-band magnitude difference of the two brightest galaxies within half the virial radius larger than 2 mag. In this work, because we do not have homogeneous R-band magnitudes for group galaxies in this sample, we used the 2MASS K_s band magnitude, which is a good indicator of the stellar mass. To ensure large and blue spirals are not left out, we also checked NED and HyperLeda to examine the B-band magnitude difference. Jones et al. (2003) used r_{200} as the virial radius, while we use the exact definition of the virial radius for our cosmology, $r_{vir} = r_\Delta$ ($\Delta \sim 101$). For the typical mass concentration of groups in this sample, $0.5\, r_{vir} \sim r_{500}$. Thus, we examined the K_s- and B-band magnitude difference for group galaxies within r_{500}. Six fossil groups are selected: NGC 741, ESO 306-017, RXJ 1159+5531, NGC 3402, ESO 552-020, and ESO 351-021. RXJ 1159+5531 and ESO 306-017 are known fossil groups (Vikhlinin et al. 1999; Sun et al. 2004). We note that NGC 1132 was considered a fossil group (Mulchaey & Zabludoff 1999). However, NGC 1126 is 8.4′ from NGC 1132 with a velocity difference of 438 km s^{-1} ($r_{500} = 16.2'$ or 440 kpc for the NGC 1132 group). The 2MASS K_s magnitude difference is 1.49 mag, and the B magnitude difference is 2.07 mag. Thus, we do not consider NGC 1132 a fossil group based on the Jones et al. (2003) definition.

Although the sample is small and not representative, we examined whether these fossil groups populate a different position of the scaling relations than nonfossil groups. No significant difference in K–T, f_{gas}–T, and M–T relations is found. As shown in Figure 22, these fossil groups indeed have massive cDs. The c_{500} of these fossil groups (four listed in Table 3, others poorly constrained) are ~ 2.4–4.3, on average smaller than the average of this sample, which differs from the claim by Khosroshahi et al. (2007) that fos-

sil groups have higher mass concentration than nonfossil systems.

8. AGN HEATING AND RADIO GALAXIES

8.1. Sign of Heating in Entropy Profiles

Besides preheating (from SNe and AGN) and cooling, impulsive heating from the central AGN is often required to explain the observed scaling relations like L–T and K–T (e.g., Lapi et al. 2005). Strong shocks driven by the central AGN may boost the ICM entropy and create an entropy bump. This transient anomaly in the entropy profile may be detected in a large sample. We have searched for such entropy features in our sample and find two promising cases: UGC 2755 and 3C 449 (Figure 23). There are also three groups with a significant break observed in their surface brightness profiles (3C442A, IC1262, and A2462) that may be related to AGN heating. We briefly discuss them in the Appendix. Both UGC 2755 and 3C 449 host a strong FR I radio source with two-sided radio lobes. UGC 2755 has a central corona with a radius of ~ 3 kpc (see Sun et al. 2007 for the connection of thermal coronae with strong radio sources). From 10 kpc to 80 kpc in radius, the surface brightness profile is very flat. Then there is a sharp break at ~ 90 kpc. UGC 2755's radio lobes extend to ~ 100 kpc from the nucleus in the NVSS image, which may naturally explain the entropy bump within ~ 90 kpc. 3C 449 also has a central corona with a radius of ~ 3 kpc. Its entropy bump is at ~ 40 kpc–100 kpc and less significant as that in UGC 2755. 3C449's radio outflow is spectacular and can be traced to at least 1.6 Mpc in radius from the NVSS image (compared to its r_{500} of 433 kpc estimated from r–T relation). Nevertheless, the brighter inner part of the radio jets/lobes ends at ~ 100 kpc from the nucleus. Thus, the entropy bump we observed in 3C 449 may represent the most recent heating event.

Strong shocks are required to effectively boost entropy. Using the standard Rankine–Hugoniot conditions, the entropy increase after shocks is a sensitive function of the shock Mach number, and weak shocks have little effect on amplifying entropy. A shock with a Mach number of 1.2 only increases entropy by 0.44%. A Mach 2 shock increases entropy by 20%, while Mach 3.3 and 4.4 shocks increase entropy by 100% and 200% respectively. The entropy bump in 3C449 is only at the level of 20%, which can be produced by a single Mach 2 shock. The entropy boost in UGC 2755 is 1.5–2 times, which can be produced by a single Mach 3 shock. The adiabatic sound speed in groups is not high, 540–630 km s^{-1} in 1.1–1.5 keV ICM for these two groups. In these low density groups, the ambient pressure is much lower than that in the dense cores of hot clusters. Shock deceleration may also be slower. The velocity of the outflow-driven shock is $\sim f_P(P_{kin}/\rho r^2)^{1/3}$, where ρ is the ICM density and f_P is a structure factor of order unity that depends on the outflow geometry and the preshock density profile (e.g., Ostriker & McKee 1988). $n_e \sim 10^{-3}$ cm^{-3} around the entropy bumps and $P_{kin} \sim 10^{44}$ ergs s^{-1} from the radio luminosities of two radio AGN and the relation derived by Bîrzan et al. (2004). The estimated velocity is then $\sim 1300 f_P$ km s^{-1}, which is comparable to the requirement of the entropy boost. Therefore, radio outflows in these two groups are capable of driving Mach 2–3 shocks to produce the observed entropy bumps.

8.2. Strong Central Radio Sources in this Sample

There are ten groups hosting a central radio source that is more luminous than $L_{1.4GHz} = 10^{24}$ W Hz^{-1}: 3C 31, 3C 449, UGC 2755, 3C 442A, A160, A2717, AS1101, A3880, A1238

and A2462. What is the typical X-ray gas environment around these radio sources? Six of them lack large cool cores (e.g., $\gtrsim$ 30 kpc radius), 3C31, 3C 449, UGC 2755, A160, A1238 and A2462. However, all of them host a central corona with a radius of ∼ 3–8 kpc, typical for massive cluster and group galaxies as discussed in Sun et al. (2007). This component is reflected in their temperature profile, except for A1238 as it is faint. The spectrum of A1238's central source can be described by a ∼ 0.8 keV thermal component. Its X-ray luminosity and K_s band luminosity fall on the typical region for coronae and its properties are similar to ESO 137-006 in A3627 (a nearby bright corona, Sun et al. 2007). Four other groups (3C442A, A2717, A3880 and AS1101) host larger cool cores with a radius of ∼ 30 kpc or larger. The cool cores in 3C442A and A2717 are clearly disrupted, likely by the radio sources. Thus, all these strong radio sources have low-entropy ICM ($<$ 30 keV cm^2) at the center.

9. SYSTEMATIC ERRORS

We follow Humphrey et al. (2006), G07 and V09 to discuss the systematic error budgets in our results. The uncertainties of the local X-ray background are the main error budget at large radii. As shown in Section 3.2, we have included a conservative estimate of the background uncertainties into the errors of temperatures and densities. This is the primary reason that our results at large radii have larger errors than those of V06 for the same systems.

We used the LAB survey data (Kalberla et al. 2005) for the galactic hydrogen column density (Table 2) and examined the *Chandra* spectra for excess absorption. The LAB column density is on average ∼ 6% lower than the column density from Dickey & Lockman (1990). Out of 43 groups we studied, 19 show significant excess absorption. We can compare this fraction to that of V05, 6 out of 13 with excess absorption. For the five groups that were studied in V05 and this work, both works find excess absorption for the same three groups. On the other hand, G07 used the galactic hydrogen column density from Dickey & Lockman (1990) for all groups. The incidence of excess absorption in our work increases with the galactic hydrogen column density. At $N_{21cm} > 4 \times 10^{20}$ cm^{-2}, eight of eleven groups (most of them at $z < 0.03$) show excess absorption. This trend is qualitatively consistent with the result by Arabadjis & Bregman (1999). We also examined the effects of a conservative N_H uncertainty of $\pm 2 \times 10^{20}$ cm^{-2} (see e.g., V09) on our results. For $T < 1.6$ keV gas, the determination of temperature is little affected by absorption. An N_H change of $\pm 2 \times 10^{20}$ affects the temperature by ∼ ∓ 1.4% and the density by ∼ ± 6.1%. The subsequent changes on K, M, Y_X, and f_{gas} at an overdensity radius are ∼ ∓6.3%, ∓2.1%, ±3.9% and ±7.6% respectively, assuming an entropy slope of 0.7 (note that the overdensity radius also depends on mass). For $T > 1.6$ keV gas, an N_H change of $\pm 2 \times 10^{20}$ affects the temperature by ∼ ∓ 5.3% and the density by ∼ ± 3.7%. The subsequent changes on K, M, Y_X, and f_{gas} at an overdensity radius are ∼ ∓5.9%, ∓8.0%, ∓4.4% and ±9.7% respectively. At small radii, uncertainties at these levels are not important as they are smaller than the intrinsic scatter (e.g., $K_{0.15r500}$ and $f_{gas,2500}$). At large radii, the statistical errors (including uncertainties from the local X-ray background) overwhelm. Nevertheless, the systematic errors from N_H should be kept in mind.

We use the deprojection algorithm derived by Vikhlinin (2006). The form of the three-dimensional temperature profile is the same as that used in V06. The robustness of this

deprojection algorithm has been presented in Vikhlinin (2006), with uncertainties of ∼ 0.05 keV. Nagai et al. (2007a) presented mock *Chandra* analysis of cluster simulations, using the deprojection algorithm proposed by Vikhlinin (2006) and the form of the temperature profile used in V06. The best-fit three-dimensional temperature profile is well consistent with the true temperature profile in simulations, with residuals in a similar level as shown in Vikhlinin (2006). This test further validates the approach used in the present work. We have also performed a test on a sub-sample of 6 groups with best-quality data. The traditional onion-peeling method (e.g., McLaughlin 1999; G07) was used. The resulting deprojected temperature profiles often show small magnitude of oscillating. If we use the form of Equation (2) to fit them, the best fits are consistent with those shown in Figures 3–5 within ∼ 0.05 keV on average. The uncertainties on temperatures range from 2%–6%, while the uncertainties on densities are 0.5%–3% (both directions). Thus, this systematic error (larger for < 1 keV groups) are smaller than the systematic error related to the uncertainty of N_H.

There are other systematic errors, like the choice of the plasma spectral codes, and departures from spherical symmetry in the group gas. Those are either small in magnitude or have little impact on the scaling relations, as discussed in Humphrey et al. (2006), G07 and V09. As mock data from simulations are starting to be analyzed in the same way as the observational data (Nagai et al. 2007a; Rasia et al. 2008), these factors are becoming better controlled.

10. SUMMARY AND CONCLUSIONS

We present an analysis of 43 galaxy groups with *Chandra* observations. With inclusion of many faint systems (e.g., the ones hosting strong radio sources), our sample is not much biased to X-ray luminous groups, as shown by the wide range of ICM entropy values around the group center (Section 6). We used the ACIS stowed background and modeled the local CXB for each group. Uncertainties of local background are folded into the derived temperature and density profiles. The projected temperature profile and the surface brightness profile are modeled with sophisticated models, which have enough freedom to describe the data from the core to the outskirts. The three-dimensional abundance profile is also derived. The three-dimensional temperature and density profiles are constrained through iterative fitting. The uncertainties are estimated from 1000 Monte Carlo simulations. Gas properties are derived to at least r_{2500} for all 43 groups. For 11 groups, we can derive gas properties robustly to r_{500}. For another 12 groups, gas properties can be robustly derived to $\gtrsim r_{1000}$, so we extrapolate the results to r_{500}. The main results of this paper are:

1. We present the M_{500}–T_{500} and M_{500}–$Y_{X,500}$ relations in $M_{500} = 10^{13}$ $h^{-1}M_\odot$–10^{15} $h^{-1}M_\odot$, combined with the V09 results on 14 $T_{500} > 3.7$ keV clusters. Both relations are well behaved at the low-mass end and can be well fitted with a single power law (Section 7.1 and Figure 15). The M_{500}–$Y_{X,500}$ relation indeed has a smaller scatter than the M_{500}–T_{500} relation (about half). The M_{500}–T_{500} relation from observations is still offset from simulations (e.g., NKV07). Interestingly, the *Chandra* M_{500}–T_{500} relation is very close to the $M_{500,HSE}$–T_{500} relation in the NKV07 simulations. Although it is tempting to attribute the difference to a mass bias, better understanding of the ICM viscosity is required.
2. The group gas fraction within r_{2500} is on average much smaller than that of clusters (e.g., ∼ 0.043 for ∼ 1.5 keV

groups vs. ~ 0.09 for ~ 6 keV clusters, Section 7.2 and Figure 17), which is consistent with G07's results. The group gas fraction within r_{2500} also has a large scatter, spanning a factor of ~ 2 at any fixed temperature. On the other hand, the gas fraction measured between r_{2500} and r_{500} has no temperature dependence with an average value of ~ 0.12 (Figure 19). Thus, the generally low gas fraction in groups is due to the general low gas fraction within r_{2500}.

3. We derived the K–T relations at 30 kpc, $0.15\,r_{500}$, r_{2500}, r_{1500}, r_{1000}, and r_{500} (Section 6.1, Figure 11). The large scatter of the entropy values at 30 kpc and $0.15\,r_{500}$ reflect the wide luminosity range of groups in this sample. The K–T relation is significantly tighter beyond r_{2500} and the intrinsic scatter of entropy is the same at 10%–11% from r_{2500} to r_{500}. Thus, the group properties are more regular from r_{2500} outward, in line with the gas fraction results. With 14 clusters from V06 and V09 included, we also present K–T relations in the full temperature range (Figure 12 and Table 5). At r_{500}, the slope of the K–T relation is consistent with the value from self-similar relation (1.0).

4. The ratios of the observed entropy values to the baseline values (from adiabatic simulations) decrease with radius (Section 6.2 and Figure 13). At r_{2500}, the ratio ranges from ~ 1.8–3.5, with a weighted mean of 2.2. The weighted mean decreases to ~ 1.8 at r_{1000} and ~ 1.6 at r_{500}. The still significant entropy excess at r_{500} in groups may require a diffuse way to distribute heat (e.g., AGN heating, see Section 8.1), but it may also be understood with smoother accretion and the mass bias that may be especially large in groups (Section 6.2). The entropy excess at r_{500} is also detected for 14 clusters from V06 and V09 ($\sim 35\%$, Section 6.2). The difference in the entropy excess at r_{500} between groups and clusters ($\sim 17\%$) is not as large as previously claimed from the *ROSAT* and *ASCA* data.

5. The entropy slopes are determined at 30 kpc–$0.15\,r_{500}$, $0.15\,r_{500}$–r_{2500}, r_{2500}–r_{1500}, and r_{1500}–$r_{det,spe}$ (Section 6.3 and Figure 14). The slopes are all shallower than 1.1 beyond $0.15\,r_{500}$. Scatter is large but the average slope is ~ 0.7 beyond $0.15\,r_{500}$.

6. The group temperature profiles are similar at $> 0.15\,r_{500}$, despite large scatter within $0.15\,r_{500}$ (Section 5 and Figure 8). The average slope is consistent with the "Universal temperature profile" (Markevitch et al. 1998; De Grandi & Molendi 2002; Loken et al. 2002; V05; Pratt et al. 2007; G07; Rasmussen & Ponman 2007; LM08) but there is still scatter. The group temperature profiles also appear more peaky than those of clusters (Figure 9).

7. We also derived the concentration parameter (c_{500}) for 33 groups (Section 7.3). Our results are generally consistent with the Bullock et al. (2001) simulations under the current WMAP5+SN+BAO cosmology.

8. We selected six fossil groups in this sample and four are new. The X-ray gas properties of these fossil groups have no significant difference from nonfossil groups (Section 7.4) in scaling relations.

9. We found two groups with substantial entropy bumps (Section 8.1), which may indicate a recent strong heating episode. Both host strong radio galaxies at the center and we estimate that the radio AGN is capable of driving shocks to boost entropy to the observed level.

The emerging picture of groups from this work is that the main difference between groups and hotter clusters is the general weak ability of the group gas to stay within r_{2500}, which explains

Table 7
M_{500}–$Y_{X,500}$ Relation[a]

Sample	M_C $(10^{14}h^{-1}M_\odot)$	α
Tier 1	1.12 ± 0.16	0.605 ± 0.050
Tier 1 + clusters	1.10 ± 0.07	0.588 ± 0.012
Tier 1+2	1.12 ± 0.10	0.564 ± 0.031
Tier 1+2 + clusters	1.14 ± 0.05	0.571 ± 0.010

Notes.
[a] $E(z)^{2/5}M_{500} = M_C\,(Y_{X,500}\,/\,4\times10^{13}\ \mathrm{keV}\ M_\odot)^\alpha$. The cluster sample includes 14 $T_{500} > 3.7$ keV systems from V09. We used the BCES orthogonal regression (Akritas & Bershady 1996).

most of deviation of the group properties from the self-similar relations (e.g., entropy and luminosity). The group properties within r_{2500} have large scatter, but may all be related to variations in the level of the enclosed gas fraction within r_{2500}. Beyond r_{2500}, groups are more regular and more like clusters, making them promising tools for cosmology, as shown by the well-behaved M–T and M–Y_X relations derived in this work.

APPENDIX A

COMPONENTS OF THE *CHANDRA* BACKGROUND

The *Chandra* background has been extensively discussed before (e.g., Markevitch et al. 2003; Wargelin et al. 2004; V05; HM06; Humphrey et al. 2006). We present here a brief summary, focusing in particular on the cosmic X-ray background (CXB). There are two basic components in the quiescent *Chandra* background, particles and photons (or CXB). The dominant background component is the charged particle background (PB), which is not vignetted. The spectrum of the *Chandra* PB has been remarkably stable since 2000 (Vikhlinin et al. 2005, V05 hereafter; Hickox & Markevitch 2006, HM06 hereafter), although the absolute flux changes with time and is related to the solar cycle. The only exception so far is for BI data after the middle of 2005, which is discussed in the next section.

The cosmic hard X-ray background is considered to be composed of unresolved X-ray point sources, mostly AGN. This component can be described by an absorbed power-law with a photon index of ~ 1.5 (HM06). Its flux depends on the level of point source excision or the limiting flux for point sources. HM06 analyzed the two deepest *Chandra* fields at that time, *Chandra* deep field north (a combined clean exposure of 1.01 Ms) and south (a combined clean exposure of 0.57 Ms). The unresolved hard X-ray background flux density is $(3.4 \pm 1.7)\times10^{-12}$ ergs s^{-1} cm^{-2} deg^{-2} in the 2–8 keV band, which represents the lower limit of the hard CXB flux in shorter *Chandra* observations. The X-ray $\log N$–$\log S$ relation has been well studied allowing us to predict the average unresolved cosmic hard X-ray background below the point source limiting flux. Kim et al. (2007; K07 hereafter) presented the average

relation between point source limiting flux and expected hard CXB flux density (Figure 19 of K07). For the limiting flux for point sources in the outermost bins of groups in our sample, we expect a resolved fraction of 25%–65% in the 2–8 keV band, which corresponds to a flux density of 6.1–13.1 $\times 10^{-12}$ ergs cm^{-2} s^{-1} deg^{-2} for the unresolved hard CXB background. However, one should be aware that the K07 relation is just an average. About 30% variation can be expected over the angular scale we study (HM06).

The soft X-ray background is composed of several components, Galactic, local bubble, geocoronal and heliospheric emission (e.g., Wargelin et al. 2004; Snowden et al. 2004; Koutroumpa et al. 2007). The latter two components are primarily from the solar wind charge exchange (SWCX) emission and are time variable, with a contribution to the O VII and O VIII lines as much as the Galactic component (Koutroumpa et al. 2007). The strength of the soft X-ray background varies with the sky position (as shown in the R45, or 3/4 keV *ROSAT* all sky survey map). There has been lots of work done to quantify its spectral properties. With the *Chandra* data, Markevitch et al. (2003) and HM06 have shown that, the soft X-ray background beyond the regions with strong RASS R45 flux (e.g., the North polar spur), can be well described by a single unabsorbed thermal component with a temperature of ~ 0.2 keV. Its spectrum typically shows a broad line hump around 0.6 keV, mainly from the 0.57 keV O VII and 0.65 keV O VIII lines. The soft X-ray background has also been studied with the *Suzaku* data, which have the higher spectral resolution. Fujimoto et al. (2007) analyzed the *Suzaku* data of the North Ecliptic Pole region (R45 = 140 $\times 10^{-6}$ counts s^{-1} arcmin^{-2}) and found that the soft X-ray component at the nonflare period has a temperature of 0.18 keV with over-solar abundances. Miller et al. (2008) analyzed the *Suzaku* data of the brightest region of the North Polar Spur (NPS, R45 = 748 $\times 10^{-6}$ counts s^{-1} arcmin^{-2}) and found that the NPS thermal component has a temperature of ~ 0.28 keV with generally sub-solar abundances, besides the assumed 0.1 keV local bubble and galactic halo components with solar abundance. Snowden et al. (2008) adopted a soft CXB model composed of an unabsorbed ~ 0.1 keV component for the local hot bubble, an absorbed ~ 0.1 keV component for the cooler Galactic halo emission and an absorbed ~ 0.25 keV component for the hotter Galactic halo emission. All abundances are fixed at solar. Thus, we have enough knowledge to model the soft X-ray background.

APPENDIX B

"BLANK SKY BACKGROUND" AND STOWED BACKGROUND

Much previous *Chandra* work on clusters used the blank-sky background data,[8] which are good enough in high surface brightness regions. However, the averaged soft X-ray component in the standard blank-sky background data is very likely different from the actual soft X-ray foreground in any particular field, as pointed out previously by e.g., Markevitch et al. (2003), V05, Humphrey et al. (2006) and G07. Taking the example of the blank sky background data in period D, the ACIS-I file combines 29 pointings from 2001 January to 2004 November, at regions where R45 = 90–150. The exposures range from 27 ks to 165 ks with a median of ~ 66 ks. The ACIS-S file combines 12 pointings from 2001 November to 2003 October, at re-

gions where R45 = 90–150. The exposures range from 20 ks to 114 ks with a median of ~ 30 ks. In 5 of 12 pointings, there are no S1 data. The ACIS response has been changed significantly from 2001 to 2004 (especially because of the contamination on the optical blocking filter). Thus, it is often inadequate to only use the blank-sky background to constrain the ICM properties at low surface brightness regions. Moreover, the PB and the CXB are not separated in the blank-sky background data. When the blank-sky background is scaled to account for the flux change of the PB, the CXB in the blank-sky background data is unphysically scaled. While the PB rate did not change much between the spring of 2000 and the spring of 2004, it has been significantly increasing ever since. In 2006, the PB rate was on average 50% higher that the average value between the spring of 2000 and the spring of 2004 (Figure 6.24 from *Chandra*'s Proposers' Observatory Guide v.9[9]). Thus, any analysis for data taken after the middle of 2004 involves a large scaling of the PB, often resulting significant over-subtraction of the CXB. Therefore, a second correction besides subtracting the scaled blank-sky background is required (e.g., Vikhlinin et al. 2005). This "double subtraction" is often efficient but requires the presence of source-free regions in the *Chandra* field, which is not true for many nearby groups in our sample. In this work, we utilize the newly available ACIS stowed background data to subtract the PB component. The CXB is modeled and the uncertainties are folded into the final error budgets.

Since 2002 September, ACIS observations have been carried out twice a year in the stowed position, shielded from the sky by the science instrument module structure and away from the on-board calibration source. By the end of 2007 May, 415 ksec data had been collected. Background flares have never been observed in the stowed data. The comparison with the dark moon observations indicates that the stowed background is the same as the quiescent PB collected by the CCDs in the normal focal position (Markevitch et al. 2003; the CXC calibration website[9].). HM06 also used the stowed background (236 ks at the time of their work) to carry out absolute measurement of the unresolved CXB. They show that between 2000 January 30 and 2002 September, when the stowed background data are not available, the spectral slope of the PB is the same. Thus, we can apply the stowed background to early data. The stowed background allows us to separate the nonvignetted PB from the vignetted CXB. The main reason for our preference for the stowed background over the blank-sky background is that we have better control of the local background for nearby groups where sources fill the whole *Chandra* field. The "double subtraction" method with the blank-sky background cannot be applied for these nearby groups, as there is no region that is free of group emission. The derived local X-ray background based on stowed background also has a clear physical meaning and can be compared between *Chandra* observations with very different PB fluxes or observations with other telescopes like XMM-*Newton*. Another subtle advantage of the stowed background is related to the telemetry limit of *Chandra*, especially for the VFAINT mode data. The blank-sky background data of each specific ACIS CCD may come from different combination of observations, especially for ACIS-S (e.g., S1 versus S2+I3). Therefore, the residual or decremental background on the S1 CCD is in principle different from that on FI chips, which complicate the analysis. Similarly, even if S3 is turned on for ACIS-I observations, it cannot be used for local background

---

[8] http://cxc.harvard.edu/contrib/maxim/acisbg/

[9] http://asc.harvard.edu/proposer/POG/

study as the blank-sky background of the S3 chip (when the aim point is on ACIS-I) is only a subset of the ACIS-I blank-sky background data. On the contrary, with the stowed background, we are analyzing the absolute CXB in the interested field so data on different CCDs can be fitted jointly to make better constraints. Therefore, we used the stowed background to subtract the PB in our observations.

The spectra of the *Chandra* PB have been very stable (e.g., HM06). However, a small change of the spectral shape on the BI CCDs (S3 and S1) has been identified from around the middle of 2005, while the spectra of the PB on the FI chips still keep the same.[8] The change appears abrupt around the middle of 2005, while the spectral shape of BI data remain the same from that time to at least the middle of 2007 (private communication with Maxim Markevitch). The stowed background data have been broken into 2 periods, one with 235 ksec total exposures from five observations of 2002 September 3 to 2005 June 10 (period D), the other with 180 ksec total exposure from four observations of 2005 November 13 to 2007 May 28 (period E). We emphasize that the notation adopted here is only for the purpose of this work. We examined the spectral difference between these two periods, after matching their fluxes in the 9.5–12 keV band. The flux of the period D background is always a little lower than that of the period E background, after re-scaling. The biggest difference is seen on the S3 chip, with a 6.0% difference in the 0.35-7.0 keV band (Figure 24). The residual emission is very flat (note it is nonvignetted) and can be removed by increasing the D period background by 5.7%. The difference is smaller on the S1 chip, 2.4% in the 0.35-5.5 keV band (note that the S1 PB increases rapidly at > 5.5 keV, Figure 6.21 of *Chandra*'s Proposers' Observatory Guide v.9). The difference is consistent with zero in FI chips, ∼ 1% in the 0.5-7.0 keV band, excluding the Au line in the 2.0–2.3 keV band. Thus, we can apply the total stowed background (415 ks exposures) to the FI data. For BI data, we use the stowed background in their corresponding periods. There are only two groups in our sample with BI data taken between 2005 June 10 and 2005 November 13 (NGC 1550 and NGC 5098). Both were observed after 2005 October 22 and both have earlier FI data. We used the period E stowed background for the BI data of both groups. In this work, we also take a larger uncertainty on the normalization of period E PB for BI chips (5% compared to 3% for FI data and the period D BI data).

APPENDIX C

NOTES ON SOME GROUPS

In this section, we present notes on some groups, mainly on the comparison with previous work on the gas properties at large radii. Thus, the cited references are usually not complete for each group as the detailed dynamical and thermal structures of the group cores are beyond the scope of this work.

NGC 1550 was examined by Sun et al. (2003), with two ACIS-I observations. Now with two additional longer ACIS-S exposures in the offset positions, the gas properties in this system can be constrained much better. NGC 1550's temperature profile is among the best determined for 1 keV groups, with the good *Chandra* coverage. We can compare our results with those from G07 who analyzed two short ACIS-I observations and an XMM-*Newton* observation. The temperature profiles agree well, although we constrain the temperature to larger radii from

the ACIS-S observations. Our r_{500} and M_{500} are 10% and 50% higher than those derived by G07. Our c_{500} ($4.93^{+0.50}_{-0.46}$) is smaller than G07's (9.0 ± 0.6).

NGC 3402 has been studied by V05 and V06. Although our temperature profile is consistent with V05, the slope of the decline is smaller. The *IRAS* 100 μm map shows the presence of Galactic cirrus around the group. We indeed derived a higher absorption column, $1.1 \pm 0.1 \times 10^{21}$ cm^{-2}, than the Galactic value (4.0×10^{20} cm^{-2} from LAB). This value is smaller than that derived in V05, $1.55 \pm 0.1 \times 10^{21}$ cm^{-2}. However, the absorption difference has little effect on the derived gas temperature. As the gas temperature is mainly determined by blended line centroid, gas temperature remains almost the same, with the higher N_H in V05. Because of higher temperatures derived at large radii, our derived M_{2500} is larger than that from V06 and $f_{gas,2500}$ is smaller than in V06.

Abell 262 is a nearby luminous system in which the X-ray emission can be traced to over 800 kpc in the 7.6 ks PSPC data. A262 was included in V06 and G07 samples. We included a new deep *Chandra* exposure (110 ks) taken in 2006 in our analysis, while G07 also analyzed an XMM-*Newton* observation. Our results of r_{2500}, M_{2500}, and $f_{gas,2500}$ are consistent with those in V06 and G07. Our c_{500} ($3.48^{+0.49}_{-0.45}$) is well consistent with V06's result and is close to G07's result (4.5 ± 0.4), but smaller than the result by Piffaretti et al. (2005) (5.8 ± 1.2).

NGC 383 hosts a bright FRI radio source 3C31. There is a background cluster centered on 2MASX J01065891+3209285 at $z = 0.1116$. We derived the surface brightness profile centered on the background cluster and also analyzed a short exposure (ObsID 3555, 5.1 ks) centered on the background cluster. The cluster emission is detected to ∼ 4′ radius. In the analysis for NGC 383, we excluded the region within 6.5′ of 2MASX J01065891+3209285, which is a bit larger than its r_{500} (5.9′ for $kT = 2.3$ keV).

3C 449 is located at a Galactic latitude of −16 deg and at the outskirts of a bright *IRAS* 100 μm feature across several degrees, which should explain the enhanced absorption. It is one of the two groups with an entropy bump detected (Section 8.1).

NGC 533 was studied by Piffaretti et al. (2005; XMM-*Newton*) and G07 (*Chandra* + XMM-*Newton*). The explored radial range in spectral analysis is similar in all three work (up to 240–260 kpc). Our temperature profile agrees well with that derived by G07. Our c_{500} ($4.58^{+3.90}_{-2.34}$) is still consistent with the results by Piffaretti et al. (2005; 8.6 ± 0.7) and G07 (9.0 ± 0.7).

MKW4 is bright enough that the group emission can be traced to the very edge of the *Chandra* field. We are able to separate the group emission and the soft background emission on the S1 spectrum because of the prominent ∼ 0.6 keV hump in the soft background emission and the iron L hump in the group emission. The same *Chandra* data had been analyzed by V05 and V06. Our temperature profile agrees well with V05's, as well as properties at r_{2500} (mass and gas fraction) with V06's. However, our results at r_{500} differ from V06's. The difference should lie on the modeling of the density profile. V06 derived a very steep density profile at large radii of MKW4 ($\beta_{eff,500}$ = 0.92, Table 2 of V06), while we derived a value of ∼ 0.6, more similar to A262 and A1991 (Table 2 of V06). We notice that Vikhlinin et al. (1999) derived $\beta_{outer} = 0.67 \pm 0.06$ for MKW4, using the same PSPC data. G07 used the same
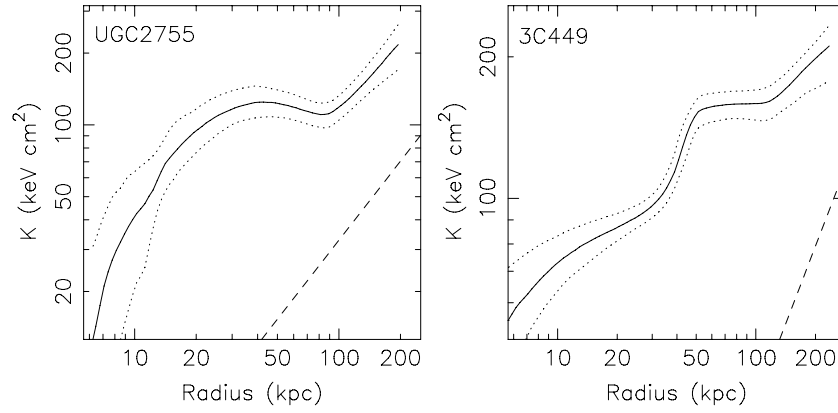
Figure 23. Two groups with a significant entropy bump: UGC 2755 and 3C 449. Both hosts an active FR I radio source (see Section 8.1). The dotted lines enclose the 1σ error region, while the dashed lines represent the baseline entropy profile (estimated from the group's mass) with a slope of 1.1.
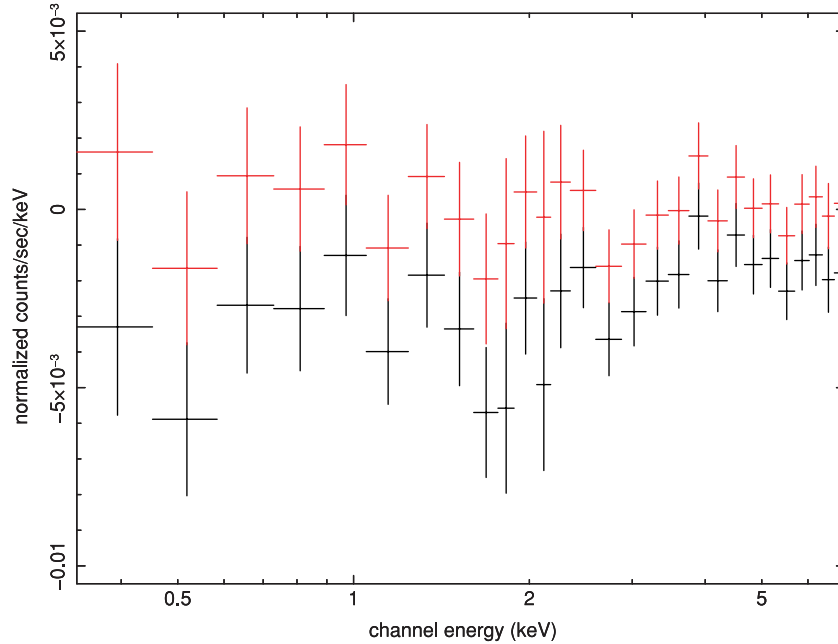

Figure 24. Spectral residual after the period D stowed background subtracted by the period E stowed background (in black). Their 9.5–12 keV fluxes are scaled to be the same. The residual is flat and is only $\sim 6\%$. The gray data points are the residual ($\sim 0\%$) if the period D stowed background is scaled up by 5.7%. Clearly after this special scaling, the 9.5–12 keV fluxes of two background are not the same, which implies a small spectral change for the BI PB from the period D to E.

(A color version of this figure is available in the online journal.)

Chandra data and also analyzed an XMM-*Newton* observation of MKW4. Our r_{500} and M_{500} are consistent with G07's values, but our c_{500} lies between the values of V06 and G07. G07 assumed an NFW profile for the dark matter halo and only derived gas properties to 322 h_{73}^{-1} kpc. The properties at r_{500} thus rely on the assumption of NFW profile and extrapolation. On the other hand, the *Chandra* data at the outermost bin only covers 10% of the area in that annulus. Better constraints on the properties of this nearby system require more coverage at large radii.

NGC 5129 is at the edge of the NPS so the local R45 value is very high. We indeed found a high local soft X-ray excess (Table 2). It is also near an extended feature on the *IRAS* 100 μm map, which should explain the enhanced absorption. G07 presented results based on an XMM-*Newton* observation. Our temperature profile is consistent with that from G07. However, our c_{500} is smaller than G07's ($3.43^{+1.72}_{-1.22}$ vs. 7.7 ± 1.3).

UGC 2755 is one of the faintest and most gas poor systems in our sample ($f_{\mathrm{gas},2500} = 0.030 \pm 0.005$). It is one of the two groups with an entropy bump detected (Section 8.1).

NGC 4325 has a luminous cooling core. NGC 4325 was studied by G07, who also analyzed an XMM-*Newton* observation. The explored radial range in spectral analysis is similar in both work (228 kpc vs. 232 kpc in our work). Our temperature profile agrees well with that derived by G07. Our c_{500}, M_{2500}, and $f_{\mathrm{gas},2500}$ are consistent with G07's within 1σ errors.

3C 442A has the most peaky temperature profile in this sample. The sharp reconstructed temperature peak at 75–150 kpc, and the steepening of the surface brightness at ~ 120 kpc, may best be explained by the second most luminous radio source in our sample (only after Abell 2462). From the NVSS image, the two radio lobes of 3C 442A extend to $\sim 5'$ (or 152 kpc) in radius. Shock heating by the radio source may explain the high temperature peak. Because of this high temperature peak, the

total mass density profile is not physically meaningful within the central ~ 160 kpc, which casts doubt on the assumption of hydrostatic equilibrium within the central 160 kpc. Therefore, c_{500} cannot be constrained reliably.

ESO 552-020 was also studied by G07. Our temperature profile is consistent with G07's. Our c_{500} is also consistent with G07's.

IC 1262 has rich substructure within its core. However, beyond the central 60 kpc radius, it appears symmetrical and relaxed. Its surface brightness profile shows a sharp break at ~ 200 kpc. Unlike 3C 442A and A2462, its radio source is faint. However, this may be caused by past AGN activity, which was also suggested to explain the rich structures in the group core by Trinchieri et al. (2007). The sharp temperature decline beyond 200 kpc also supports this scenario, as the regions between 80 and 200 kpc radius may have been recently heated (Figure 4). The adiabatic sound speed in ~ 1.9 keV gas is ~ 700 km s^{-1}. Thus, a Mach 1.5 shock will travel to the current position in ~ 200 Myr, which is consistent with the typical duty cycle of radio AGN.

ESO 306-017 has been studied before (Sun et al. 2004; G07). There is an adjacent *Chandra* pointing targeted at the $z = 0.64$ cluster RDCS J0542-4100 (ObsID 914) that we used to constrain the local soft CXB. Our temperature profile covers a wider radial range than G07's. In the overlapping region, our temperature profile is consistent with G07's. Our results on r_{500} and M_{500} are also consistent with G07's.

NGC 5098 was also studied by G07. The *IRAS* 100 μm map shows the presence of Galactic cirrus around the group and we indeed find extra absorption (Table 2). There is a second group in the field (Mahdavi et al. 2005) and the region around it is excluded in our analysis. Our temperature profile and results on r_{500}, M_{500} and c_{500} are consistent with G07's.

UGC 842 was also studied by G07. Our temperature profile and results on r_{500}, M_{500}, and c_{500} are consistent with G07's.

A2717 was studied by Pratt & Arnaud (2005), G07 and Snowden et al. (2008) with the XMM-*Newton* data. Our temperature profile is consistent with the profiles derived by G07 and Snowden et al. (2008). Our derived r_{500} and M_{500} are consistent with those derived by G07, while our c_{500} ($2.15^{+0.36}_{-0.32}$) is close to G07's value, 3.0 ± 0.2 and the result by Pratt & Arnaud (2005), 2.8 ± 0.2 (converted from their c_{200} assuming an NFW profile).

AS1101 (or Sérsic 159-03) is the most gas-rich system in our sample. Its enclosed gas fraction at $0.1 r_{500}$ (~ 0.06) is almost 3 times the average of other groups in the sample. Its gas fraction at r_{500} ($0.114^{+0.021}_{-0.020}$, extrapolated) is comparable to those of 5–7 keV clusters. The *Chandra* exposure is short but the best-fit values of our temperature profile agree well with the XMM-*Newton* results by Snowden et al. (2008). The derived c_{500} in this work ($5.05^{+2.37}_{-1.34}$) is consistent with the result by Piffaretti et al. (2005), 4.33 ± 0.51.

A1991 was also studied by V05 and V06. Our derived system properties at r_{500} and r_{2500} agree very well with those of V05 and V06. The temperature decline at large radii in this system was also found from the XMM-*Newton* data by Snowden et al. (2008) with consistent values.

A2462 hosts a small corona (with a radius of $\lesssim 4$ kpc) at the center, without a large cool core. This is common for BCGs (Sun et al. 2007; also see Section 8.2). The *Chandra* surface brightness profile shows a significant break at ~ 180 kpc, which is about the size of the central radio source from the NVSS image. The central radio source in A2462 is the most luminous one in our sample. It may have heated the group core, as shown by the high temperature and entropy beyond the central corona.

RXJ 1159+5531 has been studied by V05, V06 and G07. Our temperature profile agrees well with both V05 and G07. The derived gas fraction and total mass at r_{2500} are well consistent with those from V06. r_{500} is also consistent. Our c_{500} ($2.95^{+1.16}_{-0.90}$) lies between the results from V06 (1.70 ± 0.29) and from G07 (5.6 ± 1.5). Our r_{500} and M_{500} are consistent with G07's.

A2550 is in a large filamentary structure that connects with A2554 ($z = 0.111$, $17.5'$ on the northeast), while A2556 ($z = 0.087$) is $21'$ to the east. Based on the derived surface brightness profiles centered on each system, we exclude regions within $13.7'$ and $14.1'$ (in radius) of A2554 and A2556 respectively, which are about 1.4 times r_{500} of each system. There is also an X-ray clump south of A2550's core that is excised.

REFERENCES

Anders, E., & Grevesse, N. 1989, Geochimica et Cosmochimica Acta, 53, 197
Akritas, M. G., & Bershady, M. A. 1996, ApJ, 470, 706
Arabadjis, J. S., & Bregman, J. N. 1999, ApJ, 510, 806
Arnaud, M., Pointecouteau, E., & Pratt, G. W. 2005, A&A, 441, 893
Arnaud, M., Pointecouteau, E., & Pratt, G. W. 2007, A&A, 474, L37
Bîrzan, L., Rafferty, D. A., McNamara, B. R., Wise, M. W., & Nulsen, P. E. J. 2004, ApJ, 607, 800
Borgani, S., et al. 2004, MNRAS, 348, 1078
Borgani, S., et al. 2005, MNRAS, 361, 233
Borgani, S., & Viel, M. 2009, MNRAS, 392, L26
Bullock, J. S., et al. 2001, MNRAS, 321, 559
Buote, D. A., Lewis, A. D., Brighenti, F., & Mathews, W. G. 2003, ApJ, 595, 151
Buote, D. A., et al. 2007, ApJ, 664, 123
Croton, D. J., et al. 2006, MNRAS, 365, 11
De Grandi, S., & Molendi, S. 2002, ApJ, 567, 163
Dickey, J. M., & Lockman, F. J. 1990, ARA&A, 28, 215
Ettori, S. 2000, MNRAS, 318, 1041
Finoguenov, A., Reiprich, T. H., & Böhringer, H. 2001, A&A, 368, 749
Finoguenov, A., Jones, C., Böhringer, H., & Ponman, T. 2002, ApJ, 578, 74
Finoguenov, A., Ponman, T. J., Osmond, J. P. F., & Zimer, M. 2007, MNRAS, 374, 737
Fujimoto, R., et al. 2007, PASJ, 59, 133
Gastaldello, F., et al. 2007, ApJ, 669, 158, G07
Gilfanov, M. 2004, MNRAS, 349, 146
Gonzalez, A. H., Zaritsky, D., & Zabludoff, A. I. 2007, ApJ, 666, 147
Hickox, R. C., & Markevitch, M. 2006, ApJ, 645, 95, HM06
Humphrey, P. J., et al. 2006, ApJ, 646, 899
Jones, L. R., Ponman, T. J., Horton, A., Babul, A., Ebeling, H., & Burke, D. J. 2003, MNRAS, 343, 627
Kalberla, P. M. W., et al. 2005, A&A, 440, 775
Kay, S. T. 2004, MNRAS, 347, 13L
Kay, S. T., Thomas, P. A., Jenkins, A., & Pearce, F. R. 2004, MNRAS, 355, 1091
Khosroshahi, H. G., Ponman, T. J., & Jones, L. R. 2007, MNRAS, 377, 595
Kim, D. W., & Fabbiano, G. 2004, ApJ, 611, 846
Kim, M., et al. 2007, ApJ, 659, 29, (K07)
Komatsu, E., et al. 2009, ApJS, 180, 330
Koutroumpa, D., Acero, F., Lallement, R., Ballet, J., & Kharchenko, V. 2007, A&A, 475, 901
Kravtsov, A. V., et al. 2005, ApJ, 625, 588
Kravtsov, A., Vikhlinin, A., & Nagai, D. 2006, ApJ, 650, 128
Lapi, A., Cavaliere, A., & Menci, N. 2005, ApJ, 619, 60L
Leccardi, A., & Molendi, S. 2008, A&A, 486, 359, (LM08)
Lin, Y. T., Mohr, J. J., & Stanford, S. A. 2003, ApJ, 591, 749

Loken, C., et al. 2002, ApJ, 579, 571
Mahdavi, A., Böhringer, H., Geller, M. J., & Ramella, M. 2000, ApJ, 534, 114
Mahdavi, A., Finoguenov, A., Böhringer, H., Geller, M. J., & Henry, J. P. 2005, ApJ, 622, 187
Markevitch, M., Forman, W. R., Sarazin, C. L., & Vikhlinin, A. 1998, ApJ, 503, 77
Markevitch, M., et al. 2003, ApJ, 583, 70
Maughan, B. J. 2007, ApJ, 668, 772
McLaughlin, D. E. 1999, AJ, 117, 2398
Miller, E., et al. 2008, PASJ, 60, 95
Mohr, J. J., Mathiesen, B., & Evrard, A. E. 1999, ApJ, 517, 627
Mulchaey, J. S., & Zabludoff, A. I. 1999, ApJ, 514, 133
Mulchaey, J. S., Davis, D. S., Mushotzky, R. F., & Burstein, D. 2003, ApJS, 145, 39
Mushotzky, R., Figueroa-Feliciano, E., Loewenstein, M., & Snowden, S. L. 2003, astro-ph/0302267
Nagai, D., Vikhlinin, A., & Kravtsov, A. V. 2007a, ApJ, 655, 98
Nagai, D., Kravtsov, A. V., & Vikhlinin, A. 2007b, ApJ, 668, 1, (NKV07)
Osmond, J. P. F., & Ponman, T. J. 2004, MNRAS, 350, 1511
Ostriker, J. P., & McKee, C. F. 1988, Rev. Mod. Phys., 60, 1
Piffaretti, R., Jetzer, Ph., Kaastra, J. S., & Tamura, T. 2005, A&A, 433, 101
Pizzolato, F., Molendi, S., Ghizzardi, S., & De Grandi, S. 2003, ApJ, 592, 62
Ponman, T. J., Cannon, Damian B., & Navarro, J. F. 1999, Nature, 397, 135
Ponman, T. J., Sanderson, A. J. R., & Finoguenov, A. 2003, MNRAS, 343, 331
Pratt, G. M., & Arnaud, M. 2005, A&A, 429, 791
Pratt, G. M., Arnaud, M., & Pointecouteau, E. 2006, A&A, 429, 438
Pratt, G. W., et al. 2007, A&A, 461, 71
Puchwein, E., Sijacki, D., & Springel, V. 2008, ApJ, 687, L53
Rasia, E., Tormen, G., & Moscardini, L. 2004, MNRAS, 351, 237
Rasia, E., et al. 2008, ApJ, 674, 728
Rasmussen, J., & Ponman, T. J. 2007, MNRAS, 380, 1554

Sanderson, A. J. R., Ponman, T. J., Finoguenov, A., Lloyd-Davies, E. J., & Markevitch, M. 2003, MNRAS, 340, 989
Scannapieco, E., et al. 2005, ApJ, 635, L13
Snowden, S. L., McCammon, D., Burrows, D. N., & Mendenhall, J. A. 1994, ApJ, 424, 714
Snowden, S. L., et al. 1997, ApJ, 485, 125
Snowden, S. L., Collier, M. R., & Kuntz, K. D. 2004, ApJ, 610, 1182
Snowden, S. L., Mushotzky, R. F., Kuntz, K. D., & Davis, D. S. 2008, A&A, 478, 615
Sun, M., Forman, W., Vikhlinin, A., Hornstrup, A., Jones, C., & Murray, S. S. 2003, ApJ, 598, 250
Sun, M., Forman, W., Vikhlinin, A., Hornstrup, A., Jones, C., & Murray, S. S. 2004, ApJ, 612, 805
Sun, M., et al. 2007, ApJ, 657, 197
Trinchieri, G., Breitschwerdt, D., Pietsch, W., Sulentic, J., & Wolter, A. 2007, A&A, 463, 153
Vikhlinin, A., Forman, W., & Jones, C. 1999, ApJ, 525, 47
Vikhlinin, A., McNamara, B. R., Hornstrup, A., Quintana, H., Forman, W., Jones, C., & Way, M. 1999, ApJ, 520, L1
Vikhlinin, A., Markevitch, M., Murray, S. S., Jones, C., Forman, W., & Van Speybroeck, L. 2005, ApJ, 628, 655, (V05)
Vikhlinin, A., Kravtsov, A., Forman, W., Jones, C., Markevitch, M., Murray, S. S., & Van Speybroeck, L. 2006, ApJ, 640, 691, (V06)
Vikhlinin, A. 2006, ApJ, 640, 710
Vikhlinin, A., et al. 2009, ApJ, 692, 1033 (V09)
Voit, G. M., & Bryan, G. L. 2001, Nature, 414, 425
Voit, G. M., Balogh, M. L., Bower, R. G., Lacey, C. G., & Bryan, G. L. 2003, ApJ, 593, 272
Voit, G. M., & Ponman, T. J. 2003, ApJ, 594, L75
Voit, G. M. 2005, Rev. Mod. Phys., 77, 207
Voit, G. M., Kay, S. T., & Bryan, G. L. 2005, MNRAS, 364, 909 (VKB05)
Wargelin, B. J., Markevitch, M., Juda, M., Kharchenko, V., Edgar, R., & Dalgarno, A. 2004, ApJ, 607, 596